Rod-sphere mixture in equilibrium and under shear flow

Donald M. Guu

Rod-sphere mixture in equilibrium and under shear flow

Inaugural–Dissertation

zur Erlangung des Doktorgrades
der Mathematisch–Naturwissenschaftlichen Fakultät
der Heinrich–Heine–Universität Düsseldorf

vorgelegt von

Donald M. Guu
aus Harare Simbabwe

Düsseldorf, January 2014

aus dem Institut für komplexe Systeme, weiche Materie (ICS-3)
des Forschungszentrums Jülich

Gedruckt mit der Genehmigung der
Mathematisch–Naturwissenschaftlichen Fakultät
der Heinrich–Heine–Universität Düsseldorf

Referent :	Prof. Dr. M.P. Lettinga
Koreferent:	Prof. Dr. S. Egelhaaf

Tag der mündlichen Prüfung: 11.06.2014

This Thesis is partly based on the following publications.

[1] D. Guu, J.K.G Dhont, and M.P. Lettinga. Dispersions and mixtures of particles with complex architectures in shear flow. *The European Physical Journal Special Topics*, 222(11) : 2739 – 2755, 2013.

[2] D. Guu, J.K.G. Dhont, G.A. Vliegenthart, and M.P. Lettinga. Depletion induced clustering in mixtures of colloidal spheres and fd-virus. *Journal of Physics: Condensed Matter*, 24(46) : 464101, 2012.

Contents

1

Introduction

Colloidal dispersions offer excellent model systems for the investigation of the equilibrium phase behavior in mixtures which are ubiquitous in nature and in many practical applications. Colloids are particles in the mesoscopic length scale ranging from 1nm to 10μm which are dispersed in a fluid medium. An example of a naturally occurring system made up of a mixture of colloidal particles having different shapes and sizes is the eukaryotic cell, the unit compartment of life. The intra-cellular concentration of proteins and other macromolecules is estimated to be as high as 400 g/L [29]. Within such a complex and gel-like environment it is very challenging to model the bio-physical processes that occur within the cell. In industrial applications, mixtures of mesoscopic particles are encountered in many systems. Examples include commercial paints for coating surfaces which are made up of metal oxide nanoparticles that are dispersed in solutions of polymers. In the food processing industry mixtures appear in the form of dispersions containing fibers and globular macromolecules. Knowledge of the stability of such products is very important for the production process and also for the practical use of the system. The bulk phase behavior of such complex systems is very difficult to theoretically model just as in the example of the densely-packed cell cytoplasm.

The basis of a theoretical framework which can be applied to describe such multi-component systems can be tested on model colloidal systems. The versatility of colloidal dispersions as model systems is attributed to two main features. The first feature is that particles of different sizes and shapes can be synthesized in the laboratory in a controlled way. The second feature is that the interparticle forces can easily be tuned for example by changing the ionic strength of the suspending fluid solvent. The properties of model colloidal dispersions can then be used to systematically investigate the equilibrium bulk phase behavior and structure of mixtures with a higher degree of complexity. Another question that can be addressed is the influence of external fields on the phase behavior of the mixtures. This is relevant since both in natural systems and in practical applications the colloidal dispersions are usually exposed to external force fields such as shear flow.

The central theme of this thesis is the study of the stability of a model colloidal rod/sphere mixture under equilibrium conditions and the role that an external flow field plays on the phase behavior of the mixture. The following introductory chapter is divided into two main sections. The first section is a review on the equilibrium phase behavior of mixtures of colloidal particles. In the second section we introduce the phase behavior of mixtures of colloids in shear flow.

1.1 Equilibrium phase behavior of binary mixtures

Spherical particles have the simplest geometry and thereby offer the simplest system to use for developing theoretical models. We will start by discussing the equilibrium phase behavior of a binary mixture of simple hard spheres. The resulting phase behavior depends strongly on the size ratio R_{small}/R_{big} where R_{small} and R_{big} represent the radii of the small and big spheres respectively. Super-lattice structures have been observed under equilibrium conditions in the case of a binary mixture of hard spheres [11]. Such structures form when the size ratio R_{small}/R_{big} lies in the range $0.58-0.62$. The larger spheres start to experience an attractive force mediated by the smaller spheres when $R_{small}/R_{big} < 0.2$ [14]. This phenomena is known as a depletion attraction [7]. The attractive force is the result of an anisotropic osmotic pressure which the smaller spheres exert on the larger particles. The anisotropy in pressure occurs whenever the distance separating the surfaces of the larger spheres is so small such that the probability of finding the smaller particles in between two big particles is greatly reduced. The region in between the larger spheres is then said to be depleted of the smaller spheres. Smaller particles are called the depletants and the inter-particle interaction is called the depletion interaction. At high enough concentrations of the depletant, the attractive force which is induced by the smaller colloids can lead to a bulk phase separation. A rich phase behavior can be observed analogous to that of an atomic/molecular system. The different phases respond differently to simple shear flow, allowing the use of rheology as a means to probe the structure of the microphases formed in phase separating mixtures. Flexible polymer chains are commonly used as depletants. These can be modeled as penetrable hard spheres with a radius defined by the polymer's radius of gyration R_g. Such colloid/polymer mixtures have been extensively studied both experimentally and by means of numerical simulations and the result is a robust statistical mechanics based framework [64, 84].

The complexity of the system can be increased by considering mixtures of anisometric particles. Examples of anisometric particles include rod-like shaped colloids and platelets. Depending on the particle concentration, dispersions made up of one component of such particles display a manifold of liquid crystalline phases [34, 109, 116]. In mixtures of anisometric particles, complex phases are to be expected. We will consider here the colloidal rod/sphere mixture. Rods are much more efficient at inducing depletion forces compared to polymer chains [7]. This can be explained by the fact that a rod which is allowed to probe all possible orientational configurations, excludes a much larger volume compared to spherical depletants. Colloidal rods of high aspect ratio also offer the possibility to induce a relatively longer ranged depletion force than that achieved by polymer coils. For example in systems where the attraction is induced by linear polymer chains, the range of the attraction is set by R_g which is of the order $\sim 10 - 100$ nm. In rod-induced depletion, the range is set by the rod length which means the range of attraction can be increased to the order of a several μm. At this point we define a dimensionless size ratio $\xi = L/R_c$, where L is the length of the rod and R_c is the radius of spherical colloids.

We begin by considering the case of mixtures made up of spherical colloids and small rods i.e. $\xi \ll 1$. To our knowledge, in this size regime, no experimental investigations have been reported. A major reason for the lack of studies in this size regime could be the lack of model colloidal rods. The attractive interaction mediated by rods between two spherical particles can be calculated using the Derjaguin approximation. The approximation relates the force that acts between two curved surfaces to the force that would act between two flat surfaces. This is done by progressively using flat discs to approximate the curved surface [20]. The bulk phase behavior of the mixtures in this size ratio regime has likewise not received much attention. We now discuss the case where the spheres have a diameter much smaller compared to the length of the rod, so $\xi \gg 1$. In this regime the spheres play the role of the depletant. The phase topology in this case is set not only by ξ, but also by the ratio of the diameter of the sphere to that of the rod which we define as $\chi = 2R_c/D_{rod}$. Buitenhuis et al varied χ in a polymer/boehmite rod mixture and showed indeed how χ has a greater influence on the topology than ξ does [17]. Dogic et al observed the widening of the region where the isotropic and the nematic phases coexist for mixtures of filamentous monodisperse viruses and flexible polymer chains which are modelled as small spheres. In a similar system, but at much higher polymer concentrations, Barry et al observed the formation of disk-shaped 2D membrane-like structures [10]. A manifold of highly ordered structures which are rich in rods are observed when the range of ξ runs from $6-20$. In these mixtures the rods are highly monodisperse and have an aspect ratio $L_{rod}/D_{rod} > 100$ [6].

We now discuss the intermediate regime $\xi \approx 1$ where the length of the rod is of the order of the radius of the sphere. We start by considering infinitely dilute suspensions of hard spheres in the presence of ideal rods. After that we will discuss the bulk phase behavior at higher colloid concentrations. In this regime, the Derjaguin approximation over-estimates the depletion force acting between two spherical particles. Yaman et al showed how the depth of the potential decreases as $\xi \to 1$ using a numerical integration based method [120]. Direct measurements of rod-induced attractive force between colloidal spheres have been performed using optical traps [67]. July et al have shown that first order analytical calculations describe very well the experimentally measured potentials that a colloidal sphere experiences in the vicinity of a wall for rod concentrations as high as three times the overlap concentration [55]. The minimum of the depletion potential that is measured is typically in the order of several k_BT which is greater than the particle motion due to thermal energy. Such an effective attraction at the inter-particle level can induce a macroscopic phase separation at high enough colloid concentrations. Indeed at higher colloid concentrations, Monte Carlo Simulations (MCS) predict a fluid/fluid phase coexistence for mixtures with $\xi > 0.6$ and a gas/solid region for the case $\xi < 0.6$ [15]. This result is very similar to what is predicted for the bulk phase behavior of colloid/polymer mixtures. The drawback of phase boundaries that are predicted using MCS is that in the computation the rods are assumed to be infinitely thin, whereas in experiments the rods actually have a finite diameter D_{rod}. The MCS results are recaptured at a qualitative level when using the Free Volume Theory (FVT). The finite rod thickness is incorporated within the FVT calculation scheme. Interestingly, the FVT predicts a triple coexistence region of gas,liquid,and crystal phases as $\xi \approx 1$ [112]. Semi-quantitative agreement between experiments and the FVT has been shown by Koenderink et al using mixtures of silica spheres and boehmite rods at $\xi = 0.6$ [60]. The disadvantage of using this model system is that boehmite rods are rather poly-disperse which means a poorly defined ξ. The rods also show a gelling behavior at longer waiting times and it is challenging to find solvents in which the rods are neutrally buoyant.

Surprisingly, there is a dearth of systematic investigations on the equilibrium phase behavior of rod/sphere mixtures in the regime $\xi \approx 1$. The central subject of this thesis is the characterization of the stability of such a mixture under quiescent conditions. In this thesis, we use mixtures of *fd* and neutrally buoyant polystyrene spheres with size ratios ξ in the range 1.8 to 3.5. The micron-sized semi-flexible filamentous virus *fd*, is a well established model system for colloidal rods. It offers a superior colloidal rod model compared to commonly used rod systems such as xanthan or silica coated boehmite rods. It is highly monodisperse and stable in solution due to charged protein residues at its surface at $pH > 4.2$ [125]. In chapter 2 we introduce the theoretical concepts which will be used to interpret and to discuss the experimentally observed phenomena. In chapter 3 we experimentally determine the the gas/liquid binodal at various ξ using a combination of light scattering and optical microscopy techniques. In chapter 4 the phase topology of the rod/sphere mixture is fully characterized and the interfacial tension between the gas/liquid interface in mixtures that phase separate is obtained using capillary wave analysis. Chapter 4 concludes the first main section on the equilibrium phase behavior of the rod/sphere system. The non-equlibrium phase behavior is studied in chapter 5. A review of the effect of shear flow on the stability of colloidal mixtures of anisotropic particles will be presented in the following section.

1.2 Phase behavior of colloidal binary mixtures in shear flow

The discussion thus far has been dedicated to the phase behavior of binary mixtures in the absence of an external field. In this section, we review the influence of shear flow on the stability of the mixtures. The relevant length and time scales must be taken into account in order to be able to understand shear-induced phenomena. At short time/length scales, shear flow strongly influences the interactions at the particle level. The influence of shear flow increases with the shape anisotropy of the colloidal particles. Upon increasing the time/length scale, shear flow perturbs the formed microphases at a macroscopic level. The coupling of the microphases to the shear flow field and the corresponding deformation depends on several factors. Some of these factors include the interfacial tension of the coexisting phases and the difference in viscosity of the respective phases. Shear flow due to convection of material to and erosion from formed microphases

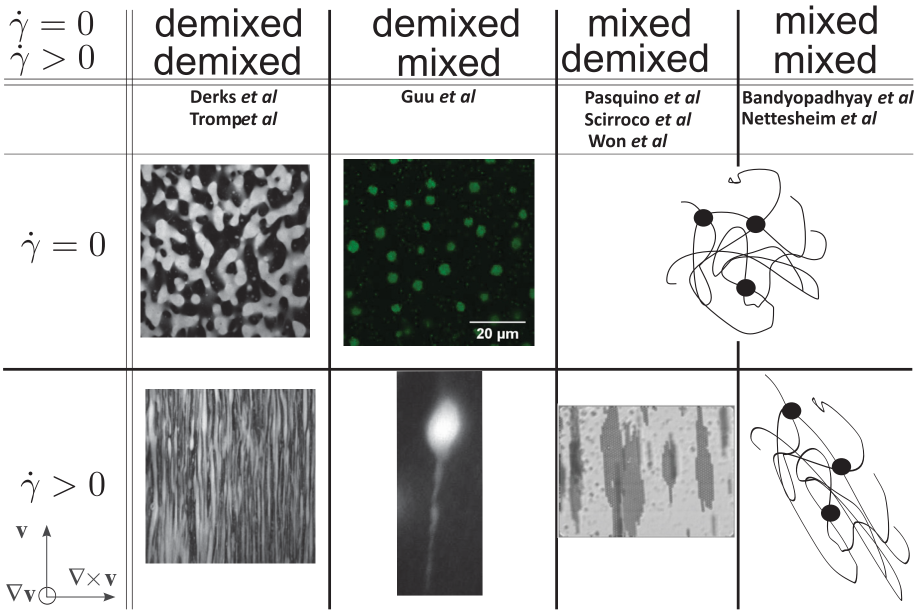

Figure 1.1: *Four different effects that shear flow can have on mixtures: mixed stays mixed; mixed becomes unstable; demixed stays demixed; demixed becomes mixed. The demixed-to-demixed example shows a phase separating colloidal sphere-polymer mixture (image taken from Ref. [22]); demixed-to-mixed shows images of sphere-rod mixture in equilibrium and in a transition state, shortly before it is completely molten by shear flow; the mixed-to-demixed and mixed-to-mixed examples both concern spheres in a visco-elastic background of WLMs, where particles can enhance structure (mixed-to-mixed) or form local structures (mixed-to-demixed, image taken from Ref. [81]). The complete figure is taken from Ref. [45] with kind permission of The European Physical Journal (EPJ).*

also contributes to the non-equilibrium phase behavior. Another important factor are the hydrodynamic instabilities that can occur within the geometry gap which in turn disturb the laminar flow profile imposed in the rheometer. To facilitate the further discussion on dispersion stability in the presence of an external flow field we will define four possible scenarios. The first one is a mixture that is stable under quiescent conditions which remains mixed in the presence of shear. The second case would be a mixture that is stable under quiescent conditions but demixes upon shearing. The third case covers dispersions that are demixed initially and upon shearing remain demixed. The fourth case would be dispersions that are demixed initially, but on shearing complete mixing is achieved. This classification scheme is summarized in figure 1.1.

The first example is a dispersion of Worm Like Micelles (WLMs) together with sub-micron sized particles which are added at a low volume fraction [9,74]. The small particles are evenly dispersed in the solution of WLMs. According to the system classification summarized in fig 1.1, the mixture falls in the *mixed* regime when no shear is applied. However a significant modification of the sample flow properties is observed when the mixture is sheared. This modification is explained using a phenomena termed double network, i.e. the formation of micelle-nanoparticle junctions which result in the observed viscoelastic behavior. The source of the viscoelastic response is the entanglement of the micelles and the formation of junctions similar to cross-linking [49, 74] (as illustrated in Fig. 1.1). The adsorption of micelles onto the surfaces of the nanoparticles complicates the characterization of the effect of flow on the interparticle forces. Systems interacting via excluded volume interactions are required in order to facilitate the development of a statistical mechanics based description of the non-equilibrium phase behavior of such systems.

An interesting phenomena is observed in similar dispersions of WLMs but with the suspended nanoparticles now replaced by micron-sized particles [81,93,118]. Necklace-like structures are formed oriented parallel to the flow direction. The formation of these ordered structures is linked to the normal stresses induced by shearing the WLMs that make up the host medium. The Weissenberg number strongly influences the magnitude of the normal stresses [39]. Scirrocco et al related shear induced ordering of suspended particles to the migration of particles towards the vicinity of the geometry walls [93]. Pasquino et al showed the formation of 2D crystalline sheets [81], as is depicted in the middle right panel in Fig. 1.1. This experimental evidence leads to the conclusion that the competition between hydrodynamic and colloidal forces plays an important role for the shear-induced ordering. The first step to gain a deeper microscopic understanding of the competition between the two aforementioned forces is to investigate the rheological response of the host medium.

The second example of a two component system is the colloid/polymer mixture. The interactions between the particles under quiescent conditions have been intensively studied in the recent past [84]. The Smoluchowski theory can be used to describe the phase behavior of attractive colloids that are subjected to shear flow. For example, Lettinga et al showed that shearing a colloid/polymer mixture moves the location of the critical point in the state diagram to higher volume fractions [66]. Dhont et al used the Smoluchowski theory to predict the deformation caused by shear flow in a similar mixture at the onset of spinodal decomposition [24]. Tromp et al reported the formation of shear bands which extend into stable doughnut-like shapes [107]. Derks et al observed that shear induced deformation increases as the structures that are formed after a spinodal decomposition continue to coarsen [22]. The phase separating mixture was sheared in a cone/plate rheometer which allows observation in real space/time (see the left panel of figure 1.1). Interestingly, many phenomenological features of the shear response of colloid/polymer mixtures that undergo spinodal decomposition can also be observed in polymer blend systems.

In this thesis we increase the anisometry of the depletant from polymer coils to a rigid rod of high aspect ratio (~ 130). We use filamentous *fd* virus to induce an attraction between the spherical colloids. The versatility of the rod/sphere mixture was already discussed in the introductory section on the equilibrium phase behavior (section 1.1). One main advantage of our system is that unlike in the WLMs/sphere dispersions, in our system we do not have the problem of adsorption and complicated particle interactions since the particles interact mainly via excluded volume interactions. Another advantage of our system is that the particles are all at the micron length scale which allows us to observe the sample's response to shear flow in real space/time on a single particle level. We are then able to probe the internal structure of the resulting micro-phases in mixtures that phase separate and to compare the subsequent deformation pathways with semi-quantitative models. The central theme of chapter 5 is the study of the internal structure of the resulting microphases in demixed samples using a counter-rotating cone/plate shear cell which is mounted onto a confocal microscope. The results are interpreted based on the knowledge gained from the characterization of the equilibrium phase behavior in chapters 3 and 4. Chapter 5 is followed by the summary and outlook.

2

Theoretical Background

This chapter introduces the theoretical background needed to interpret and discuss the measured phenomena. First the concept of the depletion interaction in colloidal mixtures is presented. Then Free Volume Theory which is a statistical mechanics based theory for calculating the phase boundaries in mixtures of colloidal particles is discussed. Capillary wave analysis is then introduced for the characterization of the interfacial properties of the resulting coexisting phases formed after depletion-induced phase separation occurs in the mixture. Finally we discuss the concepts which are essential to understand the results which are obtained from the shear experiments.

2.1 Depletion Interaction

The goal in this section is to describe the depletion interaction in a rod/sphere mixture. We will first consider the depletion interaction in a simple model system of isotropic particles namely a binary mixture of hard spheres. In the next step we will replace the spheres with rods and discuss the depletion force induced by the rods in an infinitely dilute dispersion of spheres.

2.1.1 Depletion Interaction in Binary Sphere Mixture

Binary mixtures of spherical particles exhibit a rich equilibrium phase behavior. The phase diagram of such mixtures depends strongly on the size ratio r_s/R_b,

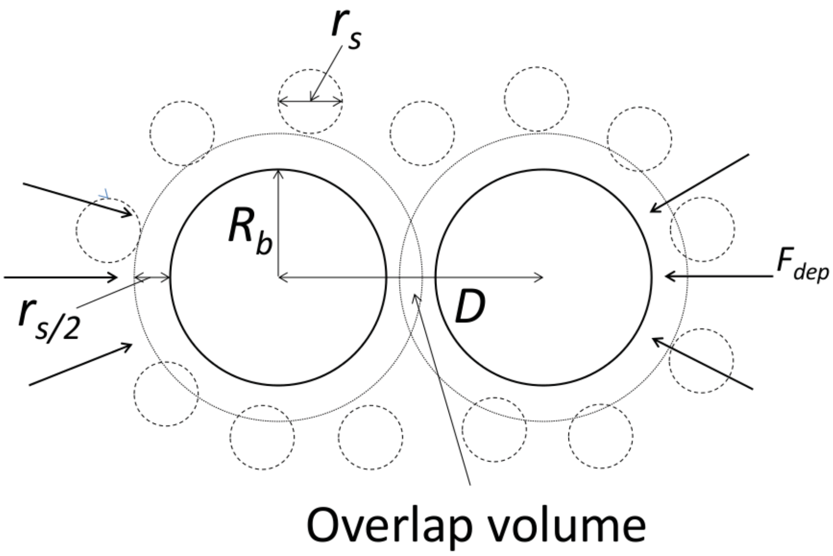

Figure 2.1: *Binary mixture of colloidal hard spheres. The larger spheres of radius R_b experience a net attractive force mediated by the smaller spheres of radius r_s. Around each sphere of radius R_b is a region depleted of the smaller spheres which has a thickness $\sim r_s/2$ defined as the depletion layer. At large inter-particle distances D the osmotic pressure exerted onto the larger colloids due to the small spheres is isotropic resulting in a zero net force. As inter-particle distance D decreases, the depletion layers start to overlap leading to an imbalance in the osmotic pressure acting on the larger spheres as indicated by the arrows in the figure. This anisotropy in the osmotic pressure then results in a net attractive inter-particle force.*

where r_s is the radius of the smaller spheres and R_b is that of the larger spheres. For example colloidal crystals with super-lattice structures are formed for a size range $(0.58 \leq r_s/R_b \leq 0.62)$ [11]. In the case that $r_s/R_b < 0.2$, the smaller particles induce an apparent attractive force between the larger spheres [14] leading to a macroscopic phase separation. In the rest of this section we will explain the origin of this depletion attraction in a system where particles interact primarily by means of repulsion.

Let us assume that we have a dispersion of larger colloidal hard spheres of radius R_b suspended in some solvent that we treat as a continuum background. The treatment of the background as a continuum is justified by the fact that the solvent molecules are orders of magnitude smaller than the spherical colloids. We now add to the dispersion smaller hard spheres of radius r_s. An isolated sphere of radius R_b, experiences an isotropic pressure acting on it due to the momentum transfer from the smaller spheres undergoing Brownian motion. For two large spheres approaching each other the osmotic pressure acting on the spheres ceases to be isotropic. We will now quantitatively determine the magnitude of this osmotic pressure imbalance.

We define a depletion layer around each large spherical particle of thickness $r_s/2$. The probability of finding a smaller sphere in this layer is reduced due to the loss in translational entropy for configurational states in which a small sphere is found very close to the surface of the larger colloid. In the case that two larger spheres approach each other and and their depletion layers begin to overlap, the colloids start to experience an imbalance in osmotic pressure and are subject to an apparent attractive force. We define an effective radius R_d

$$R_d = R_b + r_s/2 \tag{2.1}$$

As the center to center inter-particle separation distance (D) becomes less than $2R_d$, the larger particles start to experience a net attractive force as depicted in the Fig 2.1. The probability of finding smaller spheres of radius r_s in the overlap region reduces drastically and is thus depleted of the smaller spheres. The smaller particles as a result are commonly termed as the *depletants* and will be referred to as such in the subsequent discussion. From symmetry arguments, the components of the force that contribute to the inter-particle attraction are those directed on the line joining the two large spheres [64]. It can be shown that the net force F_{dep} acting on the colloidal spheres is given by

$$\begin{aligned} F_{dep} &= -\pi R_d^2 \left[1-(D/2R_d)^2\right] \qquad 2R_b \leq D \leq 2R_d & (2.2) \\ &= 0 \qquad D \geq 2R_d & (2.3) \end{aligned}$$

where the minus sign shows this is an attractive force [8,64]. By integrating the force using D as the variable over which the integration is performed we arrive at the depletion potential which can be written as

$$\begin{aligned} W_{dep} &= -n_b kT V_{ov}(D) \qquad 2R_b \leq D \leq 2R_d & (2.4) \\ &= 0 \qquad D \geq 2R_d & (2.5) \end{aligned}$$

where $V_{ov}(D)$ is the overlap volume and where n_b is the bulk number density of the depletant [114]. The derivation thus far has been for the interaction energy between two spheres mediated by a sea of smaller spheres. In the case of the W_{dep} acting between a wall and a sphere, the potential is shown to be twice as deep. For a didactic derivation using the extended Gibbs equation please refer to book by Lekkerkerker et al [64]. A closer look at equation (2.4) shows that the Depletion potential is just the osmotic pressure $n_b kT$ times V_{ov}. A result that shows that it is easy to tune the depletion force either by increasing the concentration of depletants or just by changing its size.

2.1.2 Depletion induced by Colloidal rods

2.1.2.1 Rod-induced depletion using the Derjaguin Approximation

Anisotropic colloidal particles act as very efficient depletion agents [8]. This can be explained by considering the fact that rods have a much larger excluded volume compared to their actual volume. In order to obtain an expression for the rod-induced depletion potential acting between two large spheres, we replace the small spheres of radius r_s in figure 2.1 with rods of length $L \ll R_b$. Instead of using the force method as in the case of the binary sphere mixture (section 2.1.1), we will now make use of the Derjaguin approximation which holds in the limit where the range of interaction and the inter-particle separation distance is much smaller than the radius of particles. The method is based on solving the integral given by equation 2.6

$$W_s(h) = \pi R_b \int_h^\infty W(H)dH \tag{2.6}$$

where h is the distance from sphere surface to sphere surface measured along the line joining the centers of the larger colloids while H is the distance separating sphere surfaces along a line that is parallel to the line which connects the centers of the spheres at a height z [20]. The equation 2.6 relates the potential acting between curved surfaces to the potential acting between flat discs which is much easier to compute. The first step in solving the integral is to obtain an expression for the interaction potential per unit area $W(H)$ which acts between two parallel flat plates that are used for the approximation of the curved sphere surfaces. For the case of an inter-particle interaction induced by rods $W(H)$ is given by

$$\begin{aligned} W(h^{'}) &= -\frac{1}{2}n_b kT\frac{(L-h^{'})^2}{L} \qquad 0 \le h^{'} \le L & (2.7)\\ &= 0 \qquad\qquad\qquad\qquad\quad h^{'} > L & (2.8)\end{aligned}$$

where now $h^{'}$ is the distance which separates the parallel plates, L is the length of

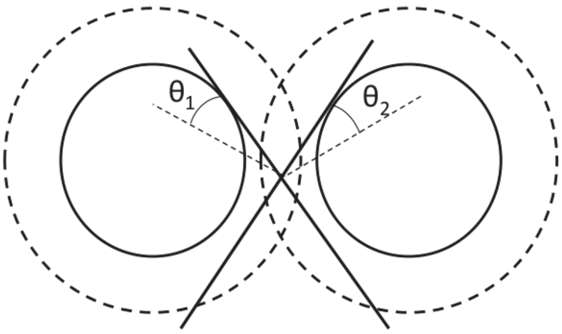

Figure 2.2: *Illustration of the parameterization used in the numerical integration method for the determination of the depletion force between spheres which is mediated by rods. The orientation of the rods is accounted for by the center of mass of sphere and two angles* θ_1, θ_2*. The parameterization sets the phase space over which integrals of the excluded volume are computed.*

the rods and n_b is the bulk number density of the rods. By inserting the expression given by equation 2.7 into the integral (equation 2.6) and then integrating over the variable H we obtain the expression for the rod-induced interaction potential acting between spherical particles as shown in equation 2.9

$$W_s(h) = -\frac{2}{3} kT\phi \frac{RL}{D_{rod}^2}\left(1-\frac{h}{L}\right)^3 \tag{2.9}$$

where h is again the distance from sphere surface to sphere surface measured along the line joining the centers of the spherical particles, D_{rod} is the diameter of rods and ϕ is the rod volume fraction. The rod-induced depletion potential as calculated by means of equation 2.9 overestimates the actual depth of the potential as the length of rod L_{rod} in the mixture approaches the colloidal sphere radius R_b. In this thesis we investigated the phase behavior of rod/sphere mixtures that fall within the regime where the deviation from the Derjaguin approximation are expected. Yaman et al have developed a more exact numerical method to calculate the depletion potential between two colloidal spheres mediated by a sea of ideal rods [61, 120, 122] which is going to be presented in the following subsection.

2.1.2.2 Rod-induced depletion using an exact numerical integration

In the preceding section we discussed the methods that can be used to determine the rod-induced depletion interaction acting between spherical particles. The calculation method using the Derjaguin approximation which was discussed in section 2.1.2.1 is only valid in the limit that the length of rod L_{rod} is much smaller than the sphere radius ($L \ll R_b$). Since in this thesis the aim is to study mixtures in which $L_{rod} \sim R_b$, we need a way to determine the depletion potential which is not restricted to relatively small size ratios. In this section we will now discuss a numerical based method for calculating the rod induced depletion which holds for any size ratio $\xi = L_{rod}/R_b$. The analysis is based on the assumption that the dispersion of rods behaves as an ideal gas in which rod-rod interactions are negligible just as it is also assumed to be the case when the Derjaguin approximation is used for the calculation. We start by considering a dispersion of thin rods i.e $L_{rod}/D_{rod} \gg 1$, where D_{rod} is the rod thickness and at low rod bulk density n_b. To determine the depletion force between two spheres suspended in the rod solution we assume that the particles only interact via excluded volume interactions. We then calculate the change in free energy ΔF in bringing the two spheres from infinite distance to the final finite separation D using equation (2.10)

$$\Delta F = \rho_{rod} kT \left[V_{ex}(D) - V_{ex}(D = \infty) \right] \tag{2.10}$$

where $V_{ex}(D)$ is the volume inaccessible for the rods when the two spheres are at a distance D from each other and $V_{ex}(D) = \infty$ is when the separation distance is set to infinity. The excluded volumes, V_{ex} in the Free energy expression are integrals over the phase space of possible rod configurations. To perform the numerical integration, the rod configurations are parameterized by the center of mass of rod and by two angles that give rod orientation as shown in Figure 2.2. The functional form used in the solving of the integral is selected after considering rod position and orientation. For an explicit description of how the numerical integration is carried out see reference [120].

We can concisely write the expression that gives the rod-induced depletion potential between the spheres $W_s(D)$ as

$$W_s(D) = \rho kTL^2RK_1(D) \tag{2.11}$$

where $K_1(D)$ describes the distance dependence of the depletion interaction and $K_1(D=0)$ is the potential when the spheres come into contact. For the rod/sphere systems that lie within the Derjaguin approximation, $K_1(D) = -\pi(1-\frac{D}{L})^3/6$. Outside of this regime there are no explicit expressions for it. We used the numerical integration method published by Lang et al to calculate $K_1(D)$ [61]. Figure 2.3 shows the plot of $K_1(D)$ for the four size ratios ξ used for the mixtures we studied. The solid line is the result one would expect for a ξ value that satisfies the Derjaguin approximation i.e when $L \ll R_b$. The plot in figure 2.3 clearly shows that in the range of size ratio $\xi \approx 1$, the depth of the depletion potential obtained from the numerical computation is much shallower than that from the one calculated for ξ values for which the Derjaguin approximation is valid. The depth of the depletion potential we obtain from the numerical integration at size ratios ≈ 1 is a several k_bT in magnitude which means we still have an appreciable attractive force induced by the rods in the mixtures that we investigated. Note that there is a small upturn at small distances in the numerically obtained $K_1(D)$ data. It can be explained by considering the interplay between the counterbalancing effect of positional and orientational degrees of freedom of the rods as the spheres approach each other. Lang et al discusses in detail this effect and show that it is not an artifact inherent in the numerical integration [61]. From figure 2.3 we also see that the range of the attraction is set by the length of the rod which in our case is $\approx 1\mu$m. Typically depletion is induced by flexible polymer chains whose radius of gyration $R_g \leq 100$ nm which means with the filamentous virus *fd* we can investigate the effect of an attraction which is by a factor 10 longer on the phase behavior of charged spheres. The efficiency of rods as depletants also means we can induce significant attraction at relatively low rod volume fractions.

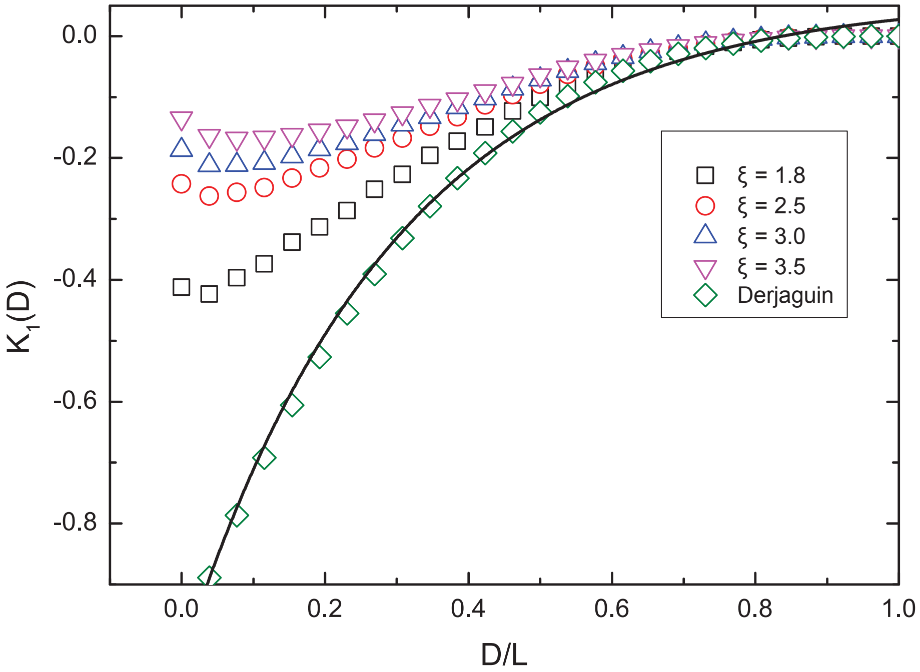

Figure 2.3: *Plot showing $K_1(D)$ for a rod/sphere mixture calculated using an exact numerical method [61]. The corresponding ξ values are shown in the legend on the right and the solid line is a representative result for a size ratio where the Derjaguin approximation is valid. As ξ increases, a systematic deviation from the Derjaguin is clearly observed.*

With this model system, we can now systematically study how ξ influences the topology of the rod/sphere phase diagram.

2.2 Free Volume Theory

The Free Volume Theory (FVT) is a versatile tool used for the prediction of the phase behavior of colloidal systems interacting via depletion forces [63,64]. The model is based is on a reservoir made up of two compartments with one containing only the depletant and the other compartment having a mixture of colloids and depletant. The two compartments are separated by a membrane permeable only to the depletant and solvent but not for the spherical particles (see Fig 2.4). The two compartments are in osmotic equilibrium and the resulting phase behavior is obtained by setting up the semi-grand potential that describes the given system. We will now outline the steps involved in applying this theory. In the

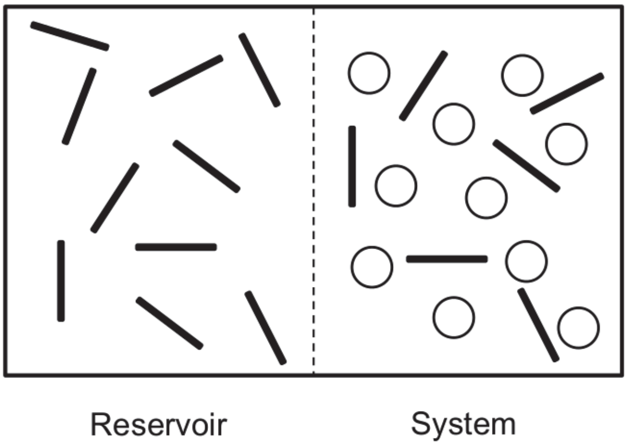

Figure 2.4: *The hypothetical scheme used in the Free Volume Theory to determine the phase behavior of a rod/sphere system. In the right compartment are the rods in the reservoir at a chemical potential* μ_2*. On the left are* N_1 *spheres with rods in the system at a temperature* T *and volume* V *which is in chemical equilibrium with the reservoir. The two compartments are separated by a membrane permeable only to the solvent and rods.*

following discussion component 1 will be the colloidal spheres while component 2 will be the rods.

We define the compartment on the left side of the figure as the reservoir in which we have rods that are at a chemical potential of μ_2. In the right compartment we have N_1 spheres together with rods at a number density which we do not know *apriori* in a volume V and at a temperature T. The semi-grand potential of such a system can be written as

$$\Omega(N_1,V,T,\mu_2) = F(N_1,V,T) + \int_{-\infty}^{\mu_2} \left(\frac{\partial \Omega}{\partial \mu_2}\right)_{N_1,V,T} d\mu_2 \tag{2.12}$$

$$= F(N_1,V,T) - \int_{-\infty}^{\mu_2} N_2 d\mu_2 \tag{2.13}$$

where $F(N_1,V,T)$ is the Helmholtz free energy of a colloidal hard sphere system in the absence of rods and the second term on the right-hand side of the equation N_2 is the number of rods that are in the system compartment together with the spheres. In order to obtain an explicit expression for N_2, we will make use of the fact that the chemical potential μ_2 is the same in both the reservoir and in the colloid/rod system since both compartments are in osmotic equilibrium. Assuming low rod number density in the reservoir, we can write the chemical potential as

$$\mu_2 = A + k_B T ln(\rho_2^r) \tag{2.14}$$

where A is a constant and ρ_2^r is the number density of rods in the reservoir. To obtain an expression for the chemical potential for the colloid/rod system compartment we use the Widom insertion principle [115] which results in the chemical potential which is given by equation 2.15

$$\mu_2 = A + k_B T ln \left(\frac{\rho_2^s V}{\left\langle V_{free} \right\rangle_0} \right) \tag{2.15}$$

where $\left\langle V_{free} \right\rangle_0$ is the free volume available for the rods if the system compartment would only be occupied by spheres and ρ_2^s is the number density of rods in the system compartment. Since both the system and resrvoir are in chemical equilibrium we can equate equations (2.14) and (2.15) and from that obtain an expression for the actual number of rods in the colloid/rod compartment which is given by equation (2.16)

$$N_2 = \rho_2^r \left\langle V_{free} \right\rangle_0 = \rho_2^r \alpha V \tag{2.16}$$

where V is the system volume and α is the free volume fraction. By means of plugging in equation (2.16) into equation (2.12) and then applying the Gibbs-Duheim relation, the semi-grand potential can now be written simply as

$$\Omega = F - \Pi \alpha V \tag{2.17}$$

where Π is the osmotic pressure of the rods in the reservoir. The next step is to obtain explicit mathematical expressions for Π and α in equation 2.17. We use the Scaled Particle Theory (SPT) [88] to obtain the required respective equations. We begin by searching for an expression for Π. We approximate the rods as sphero-cylinders of a length L and diameter D capped at the ends by a hemisphere. Equation 2.18 is the result obtained for Π for a system of sphero-cylinders.

$$\frac{\Pi v_2}{k_B T} = \frac{\phi_2^r}{1-\phi_2^r} + C_2\left(\frac{\phi_2^r}{1-\phi_2^r}\right)^2 + C_3\left(\frac{\phi_2^r}{1-\phi_2^r}\right)^3 \tag{2.18}$$

where v_2 is the volume of a sphero-cylinder and C_2 and C_3 are constants that depend on the ratio of L/D [64, 112]. For the expression which we will use for the free volume fraction α we start by simplifying the relation given in the relation 2.16 which yields equation 2.19

$$\alpha = \frac{\langle V_{free}\rangle_0}{V} = e^{-W/k_B T} \tag{2.19}$$

where W represents the reversible work that it would cost to insert a sphero-cylinder into a dispersion of hard spheres. The next step in calculating the reversible work W is by allowing the volume of the sphero-cylinder which is inserted into a system of hard spheres to shrink in size approaching zero and then to progressively expand the volume until it attains its final size. As the scaled particle size approaches that of the actual size of the sphero-cylinder, W becomes the same as the work that would be required to create a volume of a similar magnitude while acting against a pressure P^s in a hard sphere fluid which is easily calculated by using the SPT. The just mentioned relation of W and P^s helps us to obtain an expression for W given by equation 2.20

$$\frac{W}{k_B T} = -ln(1-\phi_1) + a\chi + b\chi^2 + c\chi^3 \tag{2.20}$$

here $\chi = \phi_1/(1-\phi_1)$ where ϕ_1 is the volume fraction of the hard spheres in the fluid. The constants a, b and c are polynomials which are determined by size ratios of the sphero-cylinder diameter (D) to that of the sphere diameter σ which we define as $q = D/\sigma$ and the ratio of the length of the cylinder L to that of σ which we define as $t = L/\sigma$ [64]. Inserting equation 2.20 into the equation 2.19 for the free volume fraction α we obtain equation 2.21

$$\alpha = (1-\alpha_1)exp\left[-\left\{a\chi + b\chi^2 + c\chi^3\right\}\right] \tag{2.21}$$

At this point we have all the expressions that we require to make use of equation 2.17 which yields the expressions for the chemical potential and pressure in the rod/sphere system shown in equation (2.22) and (2.23) respectively

$$\mu_1 = \left(\frac{\partial\Omega}{\partial N_1}\right)_{\mu_2,V,T} = \mu_1^0 - \Pi\frac{d\alpha}{d\phi_1}V \tag{2.22}$$

$$P = -\left(\frac{\partial\Omega}{\partial V}\right)_{\mu_2,N_1,T} = P^0 + \Pi\left(\alpha - V\frac{d\alpha}{dV}\right) \tag{2.23}$$

where now μ_1^0 represents the chemical potential of a hard-sphere system while P^0 is the pressure of a hard-sphere system. To obtain the equilibrium phase diagram of the mixture then involves first finding for each coexisting phase the explicit expressions for μ_1 and P given by equations (2.22) and (2.23) respectively then solving the equations under the conditions that satisfy coexistence of the phases shown in equation 2.24, here the superscripts I and II stand for the coexisting phases.

$$\mu_1^I = \mu_1^{II} \tag{2.24}$$

$$P^I = P^{II} \tag{2.25}$$

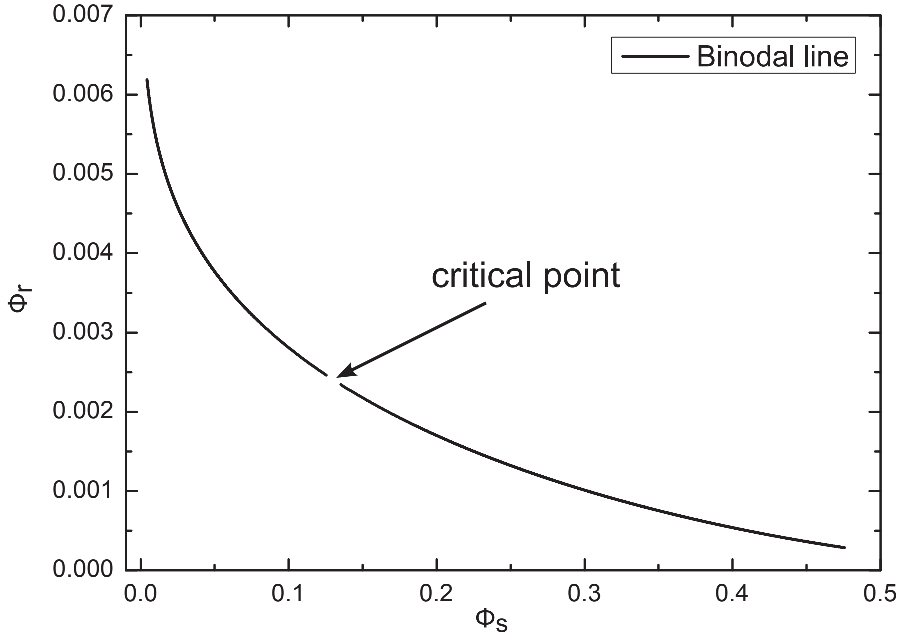

***Figure 2.5:** Plot of the gas/liquid binodal calculated using the Free Volume Theory for a rod/sphere mixture at a size ratio $L_{rod}/R_{sphere} = 3.5$. On the horizontal axis is the sphere volume fraction ϕ_s and on the vertical axis is the rod volume fraction ϕ_r.*

An example of a gas/liquid binodal line for a mixture at a size ratio $\xi = L_{rod}/R_{sphere} = 3.5$ is shown in figure 2.5. In Chapter 3 we will determine the location of binodals experimentally and then compare the results with the prediction from FVT calculations.

2.3 Capillary wave analysis of macroscopic interfaces

Until this point we have discussed methods used for determining the depletion interaction that is induced by rod-like colloids using the Derjaguin approximation [20] and with a more exact numerical integration method [62, 121]. Following that we discussed the Free Volume Theory which is used for calculating the bulk equilibrium phase diagrams in mixtures of colloidal particles [63, 64]. In this section we will discuss the characterization of interfacial properties of free interfaces that separate coexisting fluid-fluid phases which are formed as a result of the depletion induced attraction acting between the spherical particles. We

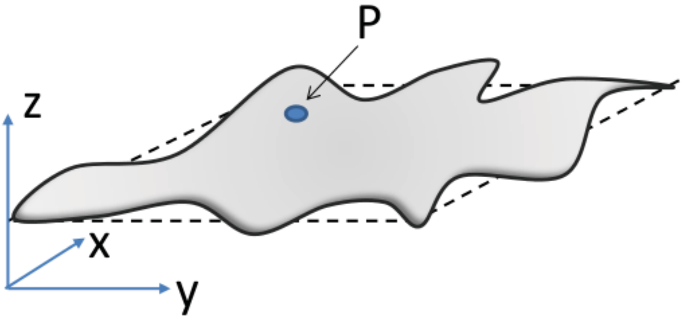

Figure 2.6: *Schematic representation of thermally-induced undulations of a flat interface of length* $L \times L$*. In the Monge representation, a local height position for a point P is given by z=h(x,y). The undistorted interface has a fixed height* $h = h_0$*.*

will focus on the capillary waves which are observed at a fluid/fluid macroscopic interface.

The starting point in analyzing thermally induced fluctuations of flat interfaces is by considering the free energy of the interfacial undulations. Given some distorted surface of size $L \times L$ as shown in Fig 2.6, we can use the Monge representation to describe points on this surface [91]. By defining a mean interface height $h = h_0$, we can then define a local height at some point P as $z = h(x, y)$ relative to h_0. From the seminal work of Mandelstam [72], we can then consider the work done, in other words the free energy increase in bringing an un-distorted interface into a distorted one. This work is given by equation (2.26)

$$\Delta F = \Delta F_1 + \Delta F_2 \tag{2.26}$$

where ΔF_1 is the work that is done against gravity to displace material during the formation of corrugations of the interface and ΔF_2 is due to the work done against capillary forces such as electrostatic attraction/repulsion in the creation of a new interface [113]. Unlike in the case of molecular fluids, where these undulations are of the order of a few nm, in colloid/polymer mixtures they are of a size that is easily accessible to real space measurement techniques such as confocal microscopy [3].

The two terms on the right hand-side of equation (2.26) can be written explicitly as follows [1]:

$$\Delta F_1 = \frac{1}{2} g \Delta\rho \int\int dxdy\, h^2 \tag{2.27}$$

where g is the acceleration due to gravity and the mass density difference is given by $\Delta\rho$.

$$\Delta F_2 = \frac{1}{2}\gamma \int\int dxdy\, (h_x^2 + h_y^2) \tag{2.28}$$

where γ is the interfacial tension. In order to transform the equations into reciprocal space, the height is transformed into the Fourier space. By replacing the Fourier series expansion of the height h into equations (2.27) and (2.28) we can write the equation for the total work done ΔF as given by equation (2.29) where k represents the modes and $h_{\mathbf{k}}$ are the Fourier coefficients in the expansion of the height. Using the equipartition theorem we assume that the work required to create each mode of the fluctuations is equal to $k_BT/2$ which leads to the mean square amplitude of each mode being expressed as shown in equation (2.30)

$$\Delta F = \frac{1}{2} L^2 \sum |h_{\mathbf{k}}|^2 (g\Delta\rho + \gamma k^2) \tag{2.29}$$

$$\langle |h_{\mathbf{k}}|^2 \rangle = \frac{k_BT}{\gamma L^2} \frac{1}{k^2 + L_c^{-2}} \tag{2.30}$$

where γ as in equation 2.29 is the interfacial tension, L is the system size and L_c is the capillary length which gives the length over which a disturbance reaches.

Thus far we have carried out the derivation considering fluctuations of single points on the interface. Experimentally it is easier to obtain the height-height correlation function. If we Fourier transform equation (2.30), what we obtain is the corresponding static correlation function $g_h(x)$ shown in equation (2.31).

The latter expression can be further simplified by transformation of the $\mathbf{s} = (x, y)$ Cartesian coordinates into cylindrical ones leading to equation (2.32). A more comprehensive treatment of the theory can be found in reference [1]

$$g_h(x) = \sum_{\mathbf{k}} \frac{k_B T}{\gamma L^2} \frac{1}{k^2 + {L_c}^{-2}} e^{i\mathbf{k}\cdot\mathbf{s}} = \frac{k_B T}{\gamma L^2} \frac{L^2}{(2\pi)^2} \int d\mathbf{k} \frac{1}{k^2 + {L_c}^{-2}} e^{i\mathbf{k}\cdot\mathbf{s}} \tag{2.31}$$

$$g_h(x) = \frac{k_B T}{\gamma L^2} \frac{1}{(2\pi)^2} \int dk \frac{k}{k^2 + L_c^{-2}} \int_0^{2\pi} d\phi \; e^{ikx\, cos\phi} \tag{2.32}$$

$$= \frac{k_B T}{\gamma L^2} \frac{2\pi}{(2\pi)^2} \int_{k_{min}}^{k_{max}} dk \frac{k}{k^2 + L_c^{-2}} J_0(kx) \tag{2.33}$$

The upper and lower limits of the integral (2.32), k_{max} and k_{min} are respectively set by the physical system size L and the microscopic length l_m. In our system, $k_{min} = 2\pi/L \simeq 0$ since L is very large. The upper limit k_{max} is set by the colloid diameter ϕ_c. In our experiments where ϕ_c = 0.5μm, this gives a $k_{max} \simeq 13$. If one plots theoretically calculated correlation functions obtained by using finite integral limits in one case and in the other setting k_{max} to infinity, a considerable difference is observed at very small distances x along the interface. For distances greater than ϕ_c, there is no significant mismatch anymore and we can thus set k_{max} to infinity instead of using a finite cut-off allowing us to analytically solve the integral 2.32. Note that in the integral, we have a Bessel function of the first kind represented by J_0. On solving the integral, we then obtain

$$g_h(x) = \frac{k_B T}{2\pi\gamma} K_0\left(\frac{x}{L_c}\right) \tag{2.34}$$

where we now have a modified Bessel function, K_0 which is written as a function of x/L_c. We use the expression in equation 2.34 to fit the experimental data with L_c and γ as the fitting parameters.

It is also possible to define a dynamic correlation function by staying at a fixed position x along the length of the interface and following the corresponding height of the interface as a function of time. This can be written as $g_h(t) = g_h(x=0,t)$. It has been shown that colloid/polymer mixtures fall into the the over-damped capillary wave regime [3, 54]. Based on this fact, theory predicts that a mode with a wave-vector $\mathbf{k}$ relaxes as $\exp(-t(\gamma k + g\Delta\rho/k)2\eta)$. Using a similar ansatz as in the derivation for the expressions used for analyzing the static correlation function, we obtain the expression for the dynamic correlation function

$$g_h(t) = \frac{k_BT}{2\pi\gamma}\int_0^{\bar{k}_{max}} d\bar{k}\frac{\bar{k}}{1+\bar{k}^2}exp(-(\bar{k}+\bar{k}^{-1})t/2\tau) \tag{2.35}$$

where $\bar{k} = L_c k$ and the relaxation time τ is given by $\tau = L_c\eta/\gamma$ [1]. The viscosity η is in actual fact a sum of the viscosities of the respective coexisting colloidal fluid phases.

2.4 Capillary wave analysis of spherical shaped droplets

It is also possible to determine the interfacial properties of spherically shaped fluid-like objects suspended in a second fluid. Typical systems where it is applied are in the study of the fluctuations of giant unilamellar vesicles (GUVs) [31,33,82,97], lipid bilayer vesicles [28] red blood cells using methods like video flicker spectroscopy [13, 32, 37, 100] and spherical microemulsions [73, 89]. The bending rigidity κ of the droplets and their interfacial tension γ can then be obtained from such an analysis. Milner et al. calculated the fluctuation spectra for nearly spherical droplets [73]. The analysis is based on the Helfrich theory of curvature elasticity [48]. A Helfrich energy expression is derived assuming that the droplets have a constant area and volume. This expression is effectively the elastic energy per unit area of droplet's surface and it characterizes its fluctuations.

Typically in experiments where the fluctuations are observed by video microscopy, the most accessible fluctuations are those in the plane of the droplet's

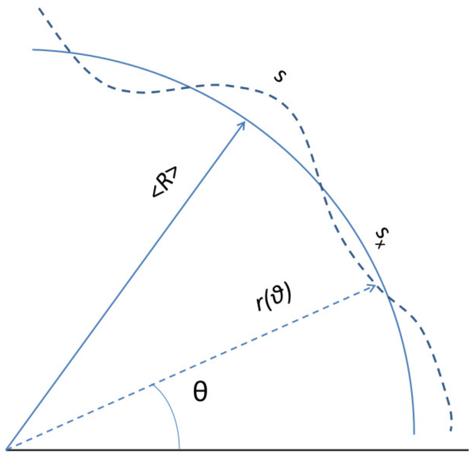

Figure 2.7: *Parameterization of Cartesian coordinates* $(s_x, u(s_x))$ *into polar coordinates. Part of a contour of a cluster is shown as dashed line and superimposed is an arc representing the mean position of the contour.The local displacement of the contour is given by* $u(s_x) = R(\theta) - <R>$*. (Adapted from Pecraux et al.).*

equator. The problem becomes two-dimensional and the spectrum can be calculated using the Helfrich equation for planar membranes equation (3.1)

$$\langle |u(q_\perp)|^2 \rangle = \frac{k_B T}{\gamma q_\perp^2 + \kappa q_\perp^4} \tag{2.36}$$

where $u(r_\perp)$ denotes the local perpendicular displacement of the interface relative to its average position and $q_\perp$ is the wave vector associated with $u(r_\perp)$ [82]. κ gives the bending rigidity and γ is the interfacial tension.

To determine the amplitude of the fluctuations, the contour of the droplet is expressed in polar coordinates (r, θ). An average position of the interface $<R>$ is calculated and the displacements about this average is given by equation $u(s_x) = R(\theta) - <R>$ (see figure2.7). The contours at the droplet's equator are decomposed into a Fourier series:

$$r(\theta) = R(1 + \sum_{n=1}^{\infty} a_n cos(n\theta) + b_n sin(n\theta)) \tag{2.37}$$

where the radius R of the contour is given by:

$$R = \frac{1}{4\pi} \sum_{n=1}^{N} (r_i + r_{i+1}) \times (\theta_{i+1} - \theta_i)) \tag{2.38}$$

The coefficients of cos and sin, a_n and b_n respectively in equation 2.37 can be used to compute the amplitude of the fluctuations relative to the mean position of the interface. To relate the spectral coefficients $\langle |u(q_\perp)|^2 \rangle$ to the interfacial tension σ, we use equation 2.39 [82].

$$\langle |u(q_\perp)|^2 \rangle = \frac{k_B T}{2\gamma} \left[\frac{1}{q_x} - \frac{1}{\sqrt{\frac{\gamma}{\kappa} - q_x^2}} \right] \tag{2.39}$$

The first few modes are discarded when fitting the Power Spectral Density (PSD). This is done to account for the significant difference in the first 5 modes between theoretically calculated fluctuation spectra of a spherical and that of a planar geometry. Above the first five modes the two spectra become indistinguishable within experimental error. At high-q, the cut-off is set by the optical resolution of the imaging setup and the pixel size of the camera which for a standard optical microscopy imaging system is of the order of q $\sim 10^{-7}\text{m}^{-1}$.

The method presented in this section can be applied in determining the interfacial tension of neutrally buoyant liquid-like clusters dispersed in a continuous medium. In comparison the method for analyzing the capillary waves at macroscopic interfaces that was discussed in section 2.4 requires that the droplets first coalesce and then sediment due to gravity to the bottom of the sample holder so as to form one continuous liquid phase. Since the latter method can only be applied for systems which are not density matched, the sedimentation-diffusion dynamics have to be taken into account in the determination of the interfacial tension [53] which is not necessary for the method in which the clusters are density-matched. Despite the differences both methods when applied to study

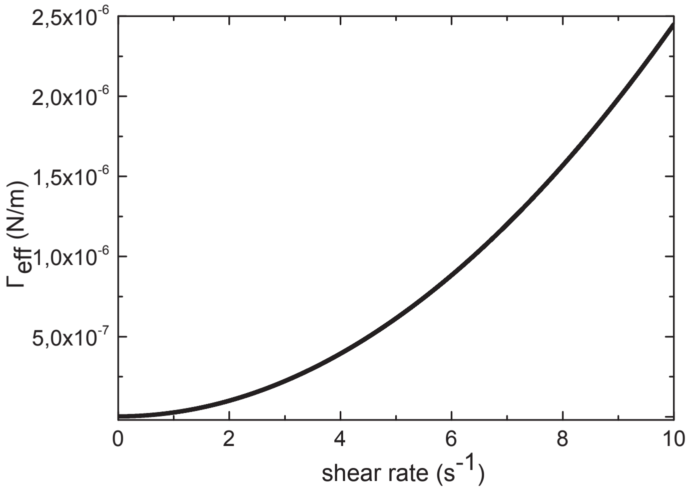

Figure 2.8: *The calculated dynamic effective interfacial tension Γ_{eff} at a gas/liquid macroscopic interface for a mixture of poly(methyl methacrylate) PMMA spheres and polystyrene polymer chains obtained from reference [21].*

free fluid-fluid interfaces of colloid/polymer mixtures they yield ultra-low interfacial as determined by other methods such as spinning drop method [18].

2.5 Shear induced suppression of Capillary Waves

In section 2.3 and 2.4 we discussed the theoretical background required to explain the capillary waves that are observed under quiescent conditions at a gas/liquid interface in colloid/polymer mixtures. In mixtures that are subjected to shear flow the amplitude of the thermally induced capillary waves decreases with increase in shear rate. This observation can be explained by the concept of an effective interfacial tension Γ_{eff} which depends on the applied shear rate [21]. For a macroscopic horizontal gas/liquid interface which lies parallel to the direction of shear flow the mathematical expression for Γ_{eff} is given by equation 2.40

$$\Gamma_{eff}(\dot{\gamma}) = \Gamma_0 + \frac{3k_BT}{4\pi}\frac{\dot{\gamma}\tau_{cap}}{L_{cap}^2}\sqrt{(\dot{\gamma}\tau_{cap})^2 - 1} \tag{2.40}$$

here Γ_0 is the interfacial tension at zero shear, τ_{cap} and L_{cap} are a characteristic time and length respectively [3] which were introduced in section 2.3. All the quantities required to apply equation 2.40 are obtained by fitting the experimentally determined dynamic height-height correlation function at the interface using equation 2.34. At low shear rates the second term on the right hand side of equation 2.40 is relatively small and the effective interfacial tension is almost equal to Γ_0. The second term increases at higher shear rates. Figure 2.8 shows the Γ_{eff} versus shear rate calculated using experimentally determined quantities for a mixture of poly(methyl methacrylate) PMMA spheres and polystyrene polymer chains obtained from reference [21]. The plot serves to illustrate how the dynamic interfacial tension depends on shear rate.

2.6 Droplet deformation under shear

Thus far we have focused on the theoretical background needed to discuss the equilibrium phase behavior of colloidal/rod sphere mixtures. In this section we discuss fundamentals essential to understand the flow behavior of the mixtures.

We start by defining the capillary number (Ca) which is a dimensionless measure for characterizing the deformation of liquid droplets of viscosity η_d (where the subscript d denotes the dispersed phase) that are suspended in a continuous host liquid phase of viscosity η_h (where the subscript h denotes the continuous host phase). The capillary number is defined as

$$Ca = \frac{\eta_h \dot{\gamma} R}{\Gamma} \tag{2.41}$$

where $\dot{\gamma}$ is the applied shear rate, R is the radius of the spherical droplet and Γ is the interfacial tension. Ca is actually the ratio of elongational/viscous forces to the capillary/surface tension forces. The breakup of droplets which are subjected to shear flow occurs above a critical capillary Ca_{crit} number which is reached when the shear stress $\eta_m \dot{\gamma}$ is of the same order of magnitude as the interfacial stress Γ. When $Ca > Ca_{crit}$ the elongational stresses are the dominating forces leading to the droplets undergoing affine deformation. In the case that $Ca <$

Ca_{crit}, the interfacial tension dominates thereby leading to droplets which are spherically shaped.

Droplet deformation mechanisms and eventually their break-up into smaller droplets when subjected to flow depends on the type of the flow field (shear or elongational), the viscosity ratio $p = \eta_d/\eta_h$ and the capillary number as defined by equation 2.41. A theoretical framework has been well established to explain the response of single droplets to a well defined flow field for the case of Newtonian liquids [108]. The stability of droplets and how they break-up has been characterized for a wide range of the viscosity ratio p running from 10^{-6} to 10^{3} and capillary numbers Ca spanning 3 orders of magnitude by Grace [40]. Figure 2.9 shows the empirical fit to the experimental data measured by Grace which separates the region where droplets acquire a steady shape,orientation and are deformed affinely in the presence of shear flow and the region where they begin to breakup [19, 108].

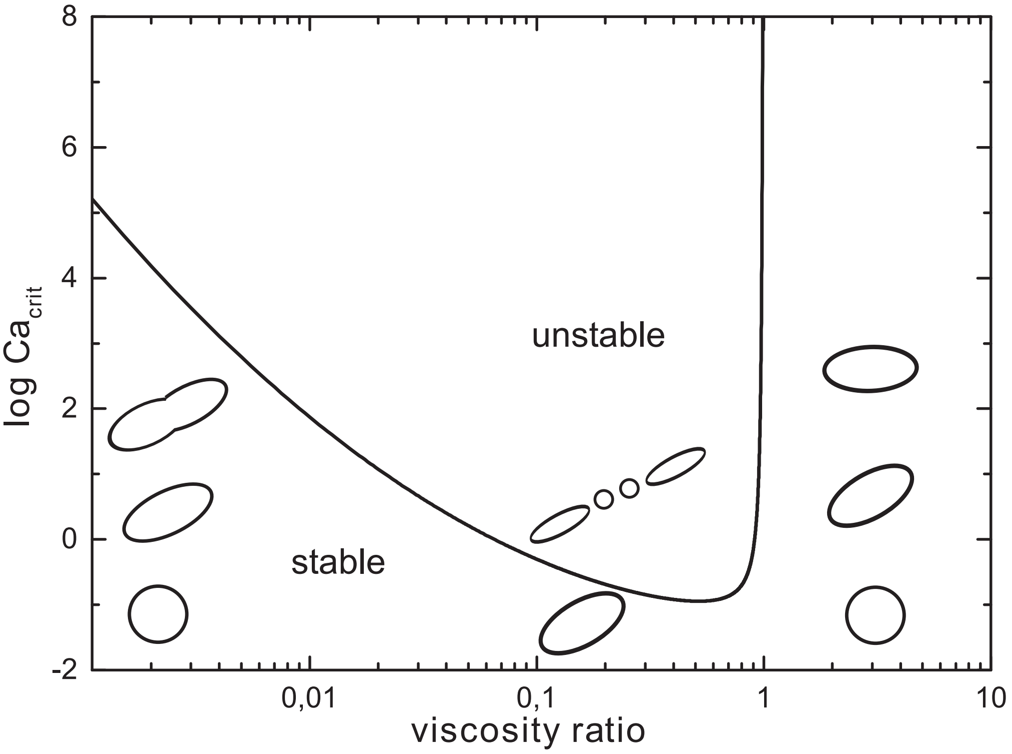

Figure 2.9: *A plot showing the dependence of droplet deformation on the critical capillary number (Ca_{crit}) and the viscosity ratio $p = \eta_d/\eta_m$ in a simple shear flow. The solid line which separates the region where stable droplets are found and the onset of droplet break-up is an empirical fit of the experimental data produced by Grace for two immiscible Newtonian liquids [40]. The mechanism of droplet breakup can be separated into three main regimes: (a) for $p \ll 1$ the droplet deforms into a sigmoidal shape and above the Ca_{crit} small droplets are released at the tips, (b) $p \sim 1$ the droplet breaks up in the middle region into daughter droplets and at $p \gg 1$ no droplet breakup is possible but rather the orientation of the steady shape changes into the direction of the flow is observed. (Figure adapted from Tucker et al [108]).*

3

Determining Binodals

We determined the gas-liquid binodal in a colloidal rod/sphere mixture using a combination of Diffusing Wave Spectroscopy and fluorescence confocal microscopy. The colloidal rods induce an attractive force between the colloidal spheres which at high enough rod concentrations leads to phase separation. We studied how the location of the binodal line in the rod/sphere mixtures is influenced by the buffer ionic strength and the size ratio L/R, where L is the length of the rod and R is the radius of the colloidal spheres. The experimentally determined binodals were compared to phase boundaries obtained using the Free Volume Theory, a well established method for calculating the phase behavior of mixtures of colloidal particles.

3.1 Introduction

In the soft matter community, entropy driven ordering at the colloidal length scale has been well established both by theoretical [36, 78] and experimental studies [6, 34]. Colloidal particles with strictly hard body interactions offer relatively simple model systems which can be used for developing a statistical mechanical description of the phase behavior of collodal dispersions. The description of colloidal dispersions with an increasing degree of complexity can then be based upon the knowledge that is acquired from the investigation of ideal model systems.

The Helmholtz free energy of a dispersion of colloidal particles interacting only via steric repulsion can be written as $F = U - TS$, where U is the interaction energy which in the case of strictly hard body interactions is zero, T is the temperature and S is the entropy. At constant temperature, the system can only minimize its free energy through maximizing its entropy S. A good example in which entropy driven ordering is observed is in colloidal hard sphere dispersions. Highly monodisperse sterically stabilized hard spheres can be synthesized in the lab by following well established protocols [98, 110]. The phase behavior of such systems has been intensively studied and transitions from liquid to crystalline and to jammed glassy states upon increasing sphere concentration have been observed [86]. The observed phase behavior can be explained by considering that at low sphere volume fractions maximum entropy is achieved in states having disordered particle configurations. As the sphere concentration increases the crystalline packing configurations offer more possible particle arrangements than the disordered states and this in turn maximizes the entropy of the system. We thus have an ordering of a colloidal system that is driven purely by entropy.

Entropic driven phase transitions also occur in mixtures of particles. The free volume available to each particle species in a multi-component mixture increases when the system phase separates. An increase in free volume corresponds to an increase in the translational entropy of the particles. Actually the entropy of mixing is lowered in the process but at high enough particle concentrations the total entropy is maximized by means of the increase in the translational entropy. A well studied mixture in which this phase separation is observed is the colloid/polymer system [84]. It is typically a suspension of hard spheres and non-adsorbing polymer chains which induce an effective attraction.

A well studied colloid/polymer mixture is the dispersion of polymethyacrylate (PMMA) particles which are sterically stabilized using poly-12-hydroxy stearic acid in cis-decalin solution mixed together with non-adsorbing polystyrene random-coils. The sterical stabilization yields nearly-hard sphere particles and the short polymer chains induce a relatively short-ranged attraction. This effective attraction is called the depletion effect and was first proposed by Asakura and

Oosawa [7] and then further developed by Vrij [114] and is discussed in detail in section 2.1. The induced attractive inter-particle force leads to a rich equilibrium phase behavior which is analogous to what is observed in molecular systems. The appearance of the phase diagram is determined by the range of the attraction which can be quantified by defining a size ratio $\xi = r_g/R$ where r_g is the polymer radius of gyration and R is the radius of the spherical colloids [38, 52]. In systems where the attraction is induced by random coils the range of the attraction is $\approx r_g$ which is of the order $\sim 10-100$ nm.

Anisometric particles (e.g. rod-shaped colloids) can also be used to induce depletion forces. Depletants having shape anisotropy are highly efficient at mediating an attractive potential between the colloidal particles. This efficiency can be explained by considering the fact that the effective volume occupied by the depletants is much larger that the actual particle volume. The topology of the equilibrium state diagram, strongly depends on the size ratio of the relevant length scale of the depletant to that of colloid of interest. In the case of rod-induced depletion between spherical colloids, this size ratio is given by $\xi = L_{rod}/R$, where L_{rod} is the rod length. Bolhuis et al using Monte Carlo based Simulations (MCS) predict a gas/solid phase coexistence for mixtures with $\xi < 0.6$ [15]. In their investigations the assumption is that the rods are infinitely thin although in experiments rods have a finite diameter. A theory that takes into account the finite thickness of rods is the Free Volume Theory [63]. Phase diagrams determined using FVT also show the strong influence of ξ on the topology of the rod/sphere state diagram [112]. Experiments have been performed in mixtures of silica spheres and boehmite rods. The rods have an aspect ratio $L_{rod}/D_{rod} < 25$ and the size ratio of the experimental system $\xi = 0.6$. They observed that the spherical particles phase separate into a sphere-rich phase made up of crystallites, a result which agrees well with the FVT predictions [60, 80]. One disadvantage of the silica sphere/boehmite rod system is that the colloids are not density matched and each particle species sediments rather quickly. This means the influence of gravity cannot be neglected when interpreting experimentally observed phenomena within these mixtures. Yasarawan et al [123] studied the phase behavior of a mixture consisting of sepiolite rods and silica spheres but in their experiments they used very high rod volume fractions ϕ_r which are well above the Isotropic/Nematic coexistence concentration making it difficult to compare the experimental results to theoretical predictions which are derived under the assumption that ϕ_r is below the overlap concentration.

Semi-flexible filamentous bacteriophages offer versatile colloidal rod-like model systems [26, 35]. *fd* viruses are a good example of such a well characterized system [90]. The viruses have an aspect ratio ≈ 130 and are charge stabilized due to the negative surface charge of the coat proteins at values of $pH > 4.2$ [125]. Adams et al have studied the equilibrium phase behavior of mixtures of *fd* and polystyrene spheres for a range of size ratios ξ running from $6 - 80$ [6]. For the ξ values that they investigated the spheres act as the depletion agents and not the rods. Concentrations of rods used in the experiments by Adams et al [6] also either lie close to the I/N coexistence regime or are already at high rod volume fractions where the rods self assemble into highly ordered phases in the absence of any depletants. In several studies *fd* virus has been used to mediate an attraction between single spherical particles and a fixed wall and to determine the corresponding depletion potential [50, 55]. To our knowledge there is a dearth of studies in the literature on the bulk phase behavior in mixtures of *fd* and colloidal spheres. This might be due to the already mentioned reason that there are few rod models that can be density matched and at the same time have a narrow size distribution having a high aspect ratio.

In this chapter we will present the experimentally determined binodal lines of colloidal rod/sphere mixtures consisting of *fd*-virus, an established model system for mono-disperse colloidal rods and density matched polystyrene spheres. We determined binodals for a range of size ratios $\xi = L/R$, where L is the length of the rod and R is the radius of the spheres. We studied the influence of electrostatic repulsion in the mixtures by performing the experiments in buffers at relatively low and at high effective ionic strength. We also used sterically stabilized rods as depletants by covalently attaching small polyethylene glycol short polymer chains onto the surface of *fd*-virus. The theoretical background needed to understand and interpret the results in this chapter is discussed in chapter 2. We present the description of the rod/sphere system and the experimental techniques used to determine the location of the binodals in section 3.2. Experimentally determined phase boundaries are presented in section 3.3 and we compare these boundaries to the boundaries determined theoretically using the Free Volume Theory. The chapter closes by a discussion of the discrepancy of theory versus experimental data and how to introduce fitting parameters to bring the two into quantitative agreement.

3.2 System description and Experimental Techniques

3.2.1 Mixtures: Polystrene spheres and *fd* viruses

Polystyrene spheres purchased from Thermo Scientific were used for preparing the rod/sphere mixtures. For a detailed description of the particle properties see Table 3.1. The spheres were concentrated by centrifugation and re-dispersed in TRIS-HCl buffer at a pH = 8.3. Ionic strengths of the buffers used were set by adding NaCl. The buffer was prepared in a D_2O/H_2O mixture to make the spheres neutrally buoyant. The spheres remain stable in solution and sealed samples of the micro-sphere stock solution do not show any sedimentation over a period of several months. The polystyrene spheres carry a negative surface charge due to ionizable sulphate groups. The buffers used in our experiments have monovalent salt ion concentrations of 25 mM and 100 mM which gives a Debye length (κ^{-1}) $\approx$ 2 nm and 1 nm respectively. We determined the concentration of the polystyrene spheres by drying the spheres in a vacuum oven and then measuring the dry weight of particles. Rod/sphere mixtures were then prepared by taking the desired concentration of each component from the respective stock solution.

The *fd* virus was obtained following the protocol outlined in [90]. The yield

Table 3.1: *Polystyrene particle physical properties*

Catalogue no.	3495A	3600A	3700A	4009A
mean diameter	496 ± 8 nm	600 ± 9nm	707 ± 9nm	994 ± 0.01 nm
standard deviation	8.6 nm	10.0 nm	8.3 nm	0.010 nm
coefficient of variation	1.7%	1.7%	1.2%	1.0%
density	1.05 g/cm^3	1.05 g/cm^3	1.05 g/cm^3	1.05 g/cm^3
Index of refraction at 589 nm	1.58	1.58	1.58	1.58

of viruses is highly mono-disperse due to the fact that *fd* essentially clones itself using the biological machinery of the host bacterial cells. *fd* was then dispersed in a 10 mM TRIS-HCl buffer at pH = 8.3 set at ionic strengths of 20 mM and 50 mM. *fd* virus is a rod-like colloid made up of single stranded DNA (ssDNA) which is covered by repeat units of a coat protein [90]. It has contour length of 0.88 μm and diameter of 6.6 nm. This gives a slender rod with an aspect ratio of 130. The persistence length $l_p \approx 3.0$ μm making *fd* a semi-flexible rod. Virus concentration is measured by UV-VIS absorbance measurements using an empirically determined extinction coefficient of 3.84 mg cm^{-2} at 269 nm [12]. At a pH>7 and the ionic strength at which the fd was suspended, the rods carry an estimated linear charge density of 10-20 e/nm [101]. The effect of the surface charge is that the rods exhibit a long range soft repulsion superimposed on top of the hard body interactions. The electrostatic repulsion between the rods is given by equation 3.1

$$\frac{U_{el(x)}}{kT} = \frac{\Gamma e^{-\kappa(x-D)}}{sin(\gamma)} \tag{3.1}$$

Where x is separation distance between two rods, Γ is a constant resulting from the solution of the Poisson-Boltzmann equation, γ is the orientation of one rod with respect to another and κ^{-1} represents the Debye length [25]. In theoretical descriptions of the phase behavior, *fd* can be described as a rod with a larger effective diameter d_{eff} than the bare *fd* diameter of 6.6 nm. The d_{eff} can be determined empirically from the plot of the isotropic/nematic coexistence concentrations versus the ionic strength. At a buffer ionic strength of 25 mM and 100

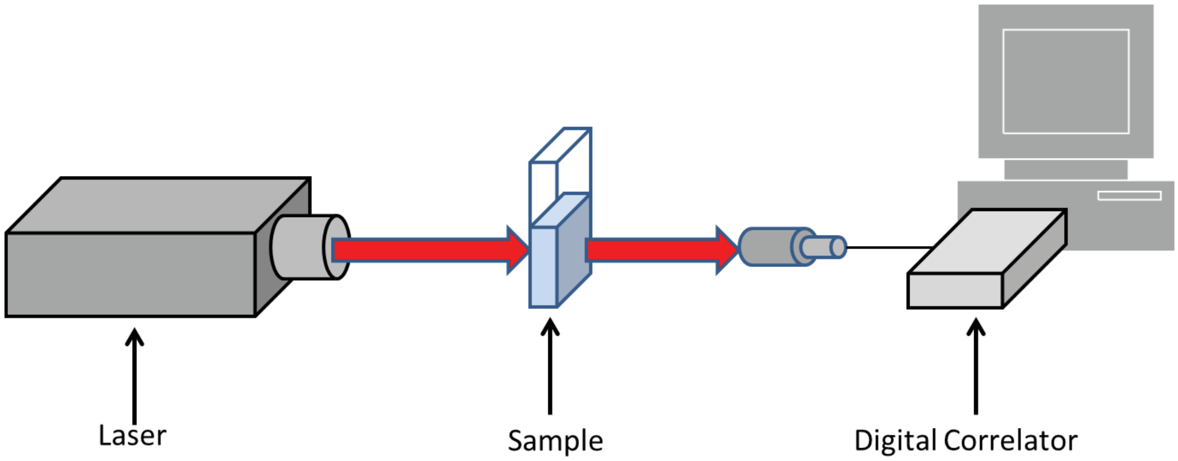

Figure 3.1: *DWS in transmission geometry. Sample is illuminated by a He-Ne 514.5 nm laser beam and the light undergoes multiple scattering in the turbid sample. Scattered light in the forward direction is detected by an avalanche photo diode and the intensity correlation function is obtained using a commercial correlator.*

mM, $d_{eff} \approx 14$ nm and 10.6 nm respectively [101]. The long ranged repulsion of the *fd* virus can be switched off by modifying the surface properties of the rods. This was done by covalently attaching onto the coat proteins of the virus, short Polyethylene Glycol (PEG) polymer chains [42]. In the protocol, end functionalized PEG is attached onto the N-terminal end of virus coat proteins. Since the PEG used is electrically neutral the polymer coated rods interact predominantly via steric repulsion depending on the surface density coverage by the linear polymer chains and on the ionic strength of buffer. At an ionic strength of 25mM, the surface charges lie completely within the PEG chains and are thus shielded. d_{eff} is now determined by the radius of gyration R_g of the polymer coils attached on the surface of the rod. As in the uncoated *fd* case discussed above, the d_{eff} can be obtained from the plot of isotropic/nematic coexistence concentrations as a function of ionic strength. For a buffer at 25 mM ionic strength as used in our experiments, this gives a $d_{eff} \approx 19$nm.

3.2.2 Experimental technique

Characterization of the *fd*/sphere dispersions was done using a combination of several techniques. In the first step bright field transmission microscopy and confocal laser scanning microscopy (CLSM) were used to estimate the location of the phase boundaries. Optical microscopy is not suitable for investigating mixtures with compositions that are close to a phase transion boundary because they scatter light strongly. For such samples we used Diffusive Wave Spectroscopy (DWS) to determine the location of binodals more precisely since it is a method developed for application in dispersions where multiple scattering occurs. DWS also has the advantage that it is highly sensitive to smaller changes in the turbidity of the colloidal dispersion. We will start by describing the optical microscopy methods we used for the determination of the equilibrium phase behavior of our rod/sphere mixture then a description of the DWS experimental setup.

Bright field microscopy was carried out on a Zeiss Axioplan 2 microscope with a 40x oil immersion objective lens. The fluorescence confocal microscopy was performed with a 60x water objective on an IX71 inverted Olympus microscope equipped with a Olympus Fluoview 300 single pinhole scanning unit. For the confocal fluorescence microscopy images, similar polystyrene spheres as in the DWS experiments were used but now with a fluorescent core. On preparing a sphere/*fd* mixture, samples were loaded into a 0.5 x 0.5 mm capillary from Vitrotube and mounted onto a glass slide to facilitate the imaging.

Diffusive wave spectroscopy was performed in transmission geometry Fig. 3.1. The sample was illuminated by a Spectra physics Beamlock 2060-06S Argon ion laser at a wavelength of 514.5 nm. The sample was placed in a 0.1 mm path length quartz suprasil cuvette and the transmitted light through the sample was captured by an optical fiber and detected by an ALV single photon avalanche diode. An ALV-6010/160 multi-tau correlator was used to compute intensity correlation functions.

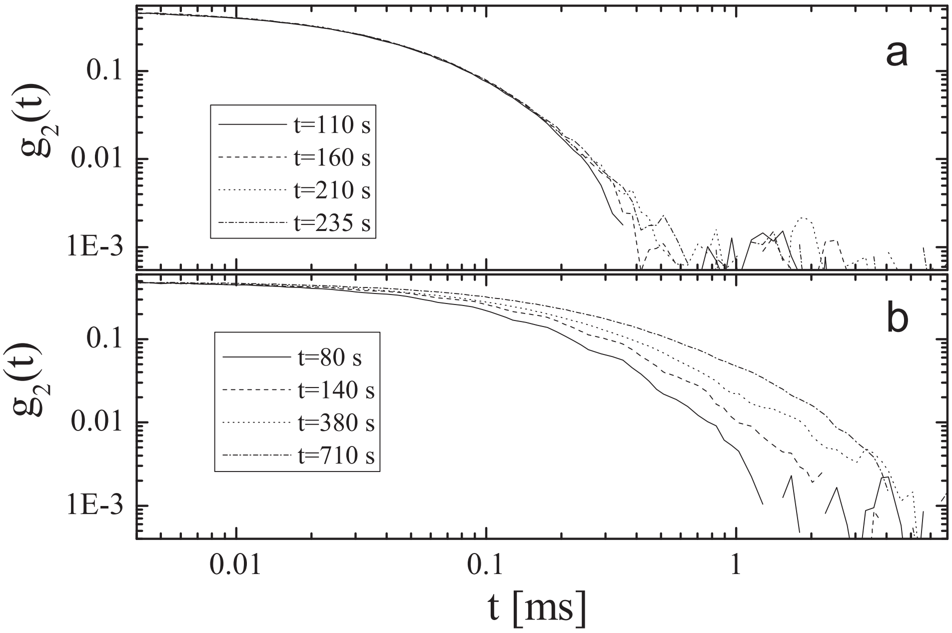

Figure 3.2: *Time series of the correlation function in a DWS experiment after mixing colloidal spheres at a fixed volume fraction of* $\phi_{spheres} = 0.02$ *and rod mass concentration of [fd] = 0 mg/ml (a) and 2 mg/ml (b). No changes in the measured correlation functions are observed in the dispersion containing only spheres, while in the mixture in which 2 mg/ml fd was added the correlation function is stretched towards longer relaxation times. (Figure taken from reference [46]).*

3.3 Results

3.3.1 Determination of phase boundaries

We prepared statepoints in the phase diagram by mixing the desired rod/sphere concentrations diluted from the respective stock solutions. Both *fd*-virus and polystyrene spheres were dispersed in an aqueous based buffer as described in section 3.2. The rod/sphere dispersions are highly turbid upon mixing due to a mismatch of the buffer refractive index ($n_{buffer} \approx 1$) compared to that of the polystyrene spheres ($n_{spheres} \approx 1.6$). In mixtures which phase separate, the turbidity of the sample decreases significantly allowing for characterization by means of optical microscopy. For statepoints that lie close to the binodal line, the mixtures scatter quite strongly. DWS was then used to investigate the precise location of the gas/liquid binodals. The samples were loaded into a quartz cuvette of 1mm optical path length after homogenizing the mixture by vortexing. The cuvette was then mounted onto a home-built DWS experimental setup (see section 3.2). Correlation functions were measured every 30 seconds until the system reached steady state. In stable mixtures, i.e mixtures in which no phase separation occurred, the measured correlation functions did not change in time. In the case of phase separating mixtures, the characteristic relaxation time of the measured correlation functions increased as the mixture phase separated.

Representative time evolution plots of correlation functions measured during an experiment are shown in Figure 3.2. Figure 3.2(a) shows what is measured in the case of a stable mixture and in the case of a demixing rod/sphere dispersion Figure 3.2(b). The measured correlation functions can be described by a stretched exponential function which has a single relaxation time τ. In Figure 3.3, representative results of the measured τ for several mixtures are plotted as a function of time. In classical Diffusing-wave spectroscopy, one defines a photon transport mean free path l^* [83]. This l^* is used as a fitting parameter of the measured auto-correlation functions. In our case this characteristic length is ill-defined since in phase separating mixtures there is a large distribution of clus-

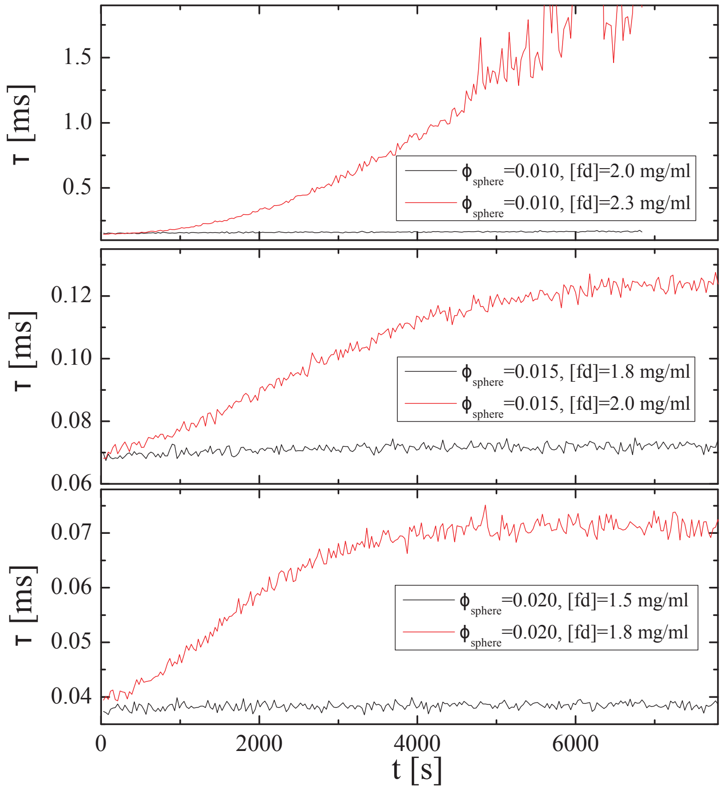

Figure 3.3: *The mean relaxation time τ plotted as a function of time after quenching at three sphere volume fractions $\phi_{spheres} = 0.01$ (a), 0.015 (b) and 0.02 (c). At a fixed $\phi_{spheres}$, the typical time evolution of τ for a stable mixture and a phase separating mixture is shown. (Figure taken from reference [46]).*

ter sizes and the turbidity changes as a function of time. With respect to phase separation kinetics, our temporal resolution is not able to resolve the onset of the demixing. We thus could not observe the nucleation time and are not able to exactly say whether we have a nucleation and growth phase separation or a spinodal decomposition taking place in our rod/sphere mixtures.

3.3.2 Binodals as a function of ξ and buffer ionic strength

We prepared mixtures of *fd* which has a contour length of 0.88 μm and monodisperse polystyrene spheres of various radii as described in section 3.2. The range of ξ covered runs from 1.8 to 3.5. By varying ξ, we effectively changed the form of the rod-induced depletion potential which acts between the spheres in the mixtures without changing the range of the attractive potential (see section 2.1). We determined the gas/liquid binodals for relatively low spherical colloid volume fractions $\phi_s < 0.03$ in a density-matched buffer at an effective ionic strength of 25mM and at 100mM. Figure 3.4(a) shows the boundaries between stable and phase separating mixture compositions for the range of ξ values studied. The open symbols represent the highest volume fraction of rods, ϕ_r added to the mixture, at a given ϕ_s, where the mixture is stable. The solid symbols represent the lowest ϕ_r measured wherein the system demixes. The solid lines serve as a guide to the eye.

We investigated the role of buffer ionic strength on the location of the phase boundary at a fixed ξ value of 3.5. Two buffers were prepared with total ionic strengths set at 25mM and 100mM both at a pH of 8.3. Figure 3.4(b) displays the binodals at the respective buffer conditions. The lower boundary in the figure with the square symbols represents the 100mM mixture while the upper one with the triangles represents the binodal line in the 25mM ionic strength buffer.

Since both *fd* and the polystyrene spheres are charged both particle species interact via a soft repulsive potential. For the spheres the range of this repulsive force is simply given by the Debye length while in the case of the charged rod there is a need to define an effective rod diameter d_{eff} see section 3.2. This consideration is important when comparing the experimentally determined binodals with theoretical predictions, since the Free Volume Theory assumes hard body interactions and does not consider the soft repulsive potential present in charged systems. Following the protocol described in section 3.2, we switched off the charge on the surface of the rods yielding sterically stabilized rods. Figure 3.5 is the comparison of the experimentally determined binodal in the *fd*-PEG/sphere system with the gas/liquid phase boundary calculated using the Free Volume Theory. At an ionic strength of 100mM the surface charge on the surface of the rods is screened quite effectively. The rods have an experimentally determined $d_{eff} \approx$ 10nm. This yields a good approximation to a hard rod. The experimentally determined binodal in the rod/sphere mixture in a 100mM ionic strength buffer is plotted in the same figure with the *fd*-PEG/sphere system for comparison in figure 3.5. The FVT calculation using d_{eff} from the Onsager consideration qualitatively agrees with the experimental data but the best fit of the data uses as an input for the calculation a higher d_{eff}.

3.4 Discussion and Conclusion

The location of the binodal line at a fixed buffer ionic strength, shifts to higher rod volume fractions ϕ_r as ξ increases (see figure 3.4(a)). Our experimental observation is in agreement with the work done by Vliegenthart et al where they showed how the location of the gas/liquid binodal in a rod/sphere phase diagram is determined by ξ using the FVT [112]. The observed bulk phase behavior also corroborates with numerical calculations which show that the depth of the depletion potential decreases monotonically as ξ increases [120] (see figure 2.3).

The experimentally determined binodal was observed to shift to lower ϕ_r by a factor two as the effective ionic strength of the buffer was increased from 25mM to 100mM as shown in figure 3.4(b). The Debye length κ for the charged polystyrene particles changes from $\approx 2nm$ to $1nm$ which is less than 1% of the radius of the spheres. This small difference does not explain the relatively large shift in the binodal. On the other hand the effective rod diameter d_{eff} changes from 14nm in the 25mM buffer to 10nm in the 100mM buffer. Changing the buffer ionic strength effectively tunes the d_{eff} and thus changes the rod aspect ratio. This evidence seems to suggest that the rod aspect ratio is an important parameter in determining the phase behavior of the rod/sphere mixture. This strong dependence of the location of gas/liquid boundary on the rod aspect ratio is confirmed when calculating binodals using the Free Volume Theory.

The binodal obtained in the mixture of spheres and the *fd-PEG* complex, which should effectively screen off the charges on the surface of the rod showed a large difference when compared to the FVT calculated binodal as shown in figure 3.5. We can only offer a few hand-waving arguments to explain the difference between experimental result and theory. One possible reason for this discrepancy is based on the efficiency of the surface coverage of the rods with the polymer chains. A patch-wise coverage could lead to an incomplete screening of the negative charge along the surface of the rods. The unscreened charges lead to a modified effective interparticle interaction. The resulting interaction potential would then be a superposition of a soft electrostatic repulsion and a steric repulsion. Within the FVT calculation scheme, we only take into account exclusively hard body interactions which could then explain the difference which we observed between FVT and the experimentally determined binodal. Another explanation for the difference between the FVT calculation and the experimental binodal is that the flexible PEG polymer coils are assumed to behave as undeformable spheres having a radius R_g which are immobilized onto the surface of the rods. In practice we would expect that the spherically shaped polymer coils are deformable. The extent of the polymer chain deformation which we are not able to quantify, alters the effective diameter of the *fd-PEG* complex and thus leads to a mismatch between FVT and experiments. However the FVT yielded a smaller deviation when compared to the experimentally obtained binodal in the case of the mixture where depletion was induced by uncoated *fd* which were dispersed in a buffer set at relatively high ionic strength. The attempt to prepare a mixture which interacts dominantly via excluded volume interactions was therefore achieved by setting the buffer ionic strength at 100mM. At this effective ionic strength we obtain a d_{eff} of 10nm which when applied for the FVT computation, yields a smaller mismatch between theory and experimental data. If we set d_{eff} as a fitting parameter, a d_{eff} of 13nm matches the experimental data quite well. There is a small difference in the shape of the binodal which we attribute to the flexibility of the *fd* which is not accounted for in the FVT. To get rid of the rod flexibility we plan in the future to use *Y21M*, a stiffer mutant of the wild-type *fd* which approaches the ideal rigid rod limit.

We find a quantitative mismatch between FVT and experiments which increases in magnitude with increasing ξ. For discussing this discrepancy, we compare the binodals that are predicted by using a d_{eff} which we obtained from two different methods. In the first case we use an empirically determined d_{eff} from the plot of the isotropic/nematic coexistence concentration versus the effective buffer ionic strength. In the second case we apply d_{eff} obtained from the best fit of the experimental data. At $\xi = 1.8$, the deviation is only $\approx 7\%$. It increases to $\approx 20\%$ for $\xi = 2.5$ and finally for the $\xi = 3.5$ it is as high as $\approx 40\%$ difference in magnitude. This discrepancy can be explained by the fact that the mathematical expression used to calculate the average free volume of rods in the phase boundary calculation scheme is correct in the limit of low ϕ_r and is only an approximation at higher ϕ_r. At larger ξ, much higher rod volume fractions are required to induce phase separation and in turn the FVT is less accurate in predicting the location of the binodal line. In our experiments we are at rod number densities that are $\approx 30c^*$, where c^* is the overlap concentration. It is very impressive that with the FVT we are able to semi-quantitatively describe the observed phenomena. Future work will be focused on developing a theory which takes into account the fact that the spheres begin to experience the depletion force at an effective range which is no longer set by L_{rod} but by the mesh size of the dynamic network made up of the rods.

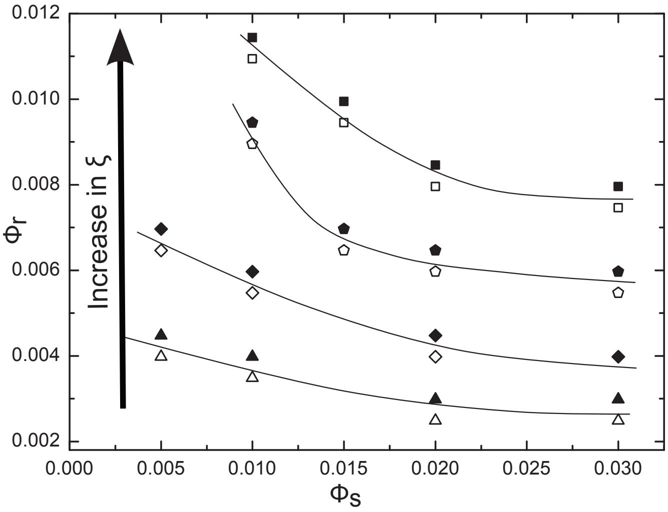

(a) Binodals as a function of ξ

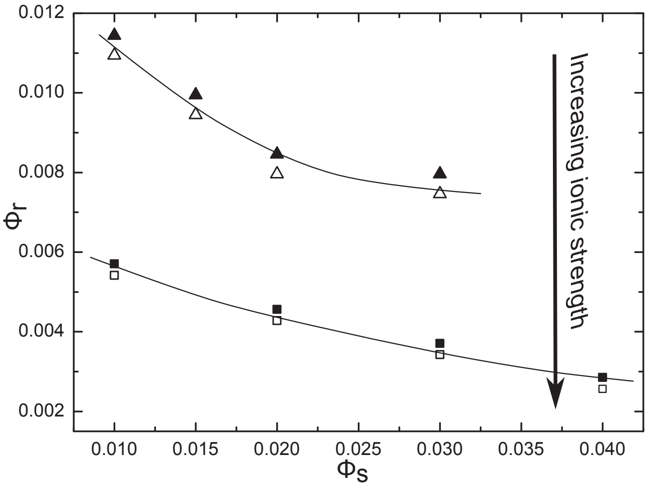

(b) Binodals as a function of ionic strength

Figure 3.4: *(a) Gas/liquid Binodal lines of a sphere-rod mixture for* ξ *= 1.8 (triangles), 2.5 (diamonds), 2.9 (pentagons) and 3.5 (squares). The open symbols in each case indicate the highest rod volume fraction* ϕ_r *at a fixed sphere volume fraction* ϕ_s *where the mixture was stable while the solid symbols indicate the lowest concentration of fd where the mixture was unstable, as determined from Fig.3.3. The vertical arrow points in the direction of increasing* ξ *values. (b) Gas/liquid Binodal lines at* ξ *= 3.5 in 25mM and 100mM ionic strength buffers. Lower boundary (square symbols) is the experimentally determined binodal in the 100mM ionic strength buffer and the upper boundary (triangle symbols) is the one for the 25mM buffer.*

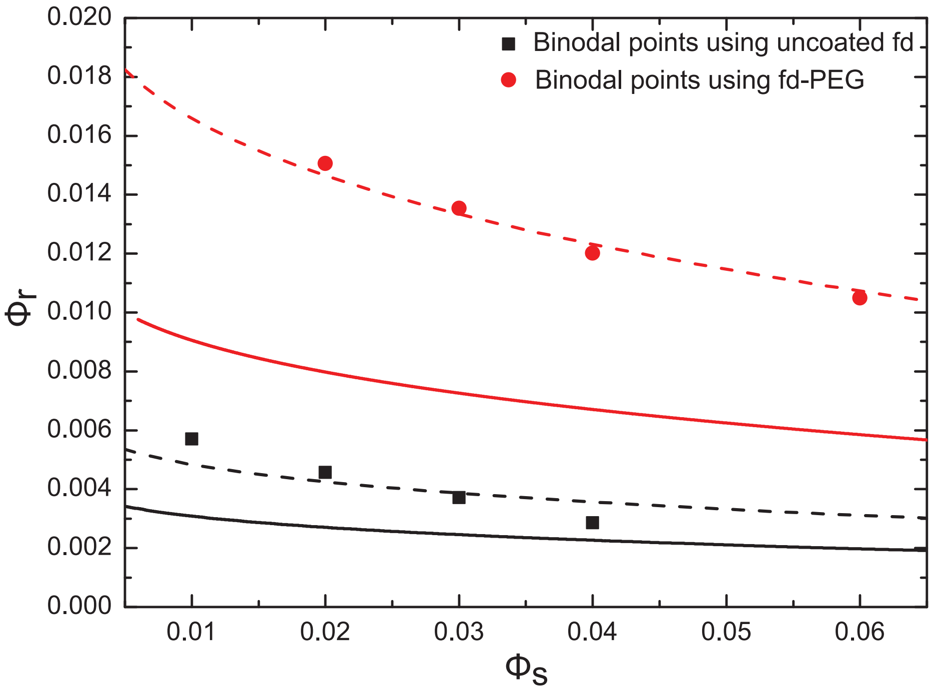

Figure 3.5: *Experimentally determined binodals of mixtures of spheres and the fd-PEG complex at an effective ionic strength of 25mM (red circles), and uncoated fd at an effective ionic strength of 100mM (black squares). The solid lines are the binodals calculated by means of the Free Volume Theory using rod diameter* d_{eff} *determined by using the Isotropic-Nematic coexistence concentration and by applying the Onsager theory on hard rods. From Onsager's theory, PEG-coated fd has a* $d_{eff} \approx$ *19nm and the uncoated fd at the given buffer ionic strength has a* $d_{eff} \approx$ *10nm. The dashed lines are the respective binodals from Free Volume Theory using the* d_{eff} *as a fitting parameter. The best fit for the fd-PEG complex mixture gave a* d_{eff} *of 28nm and in the uncoated fd* d_{eff} *= 13nm.*

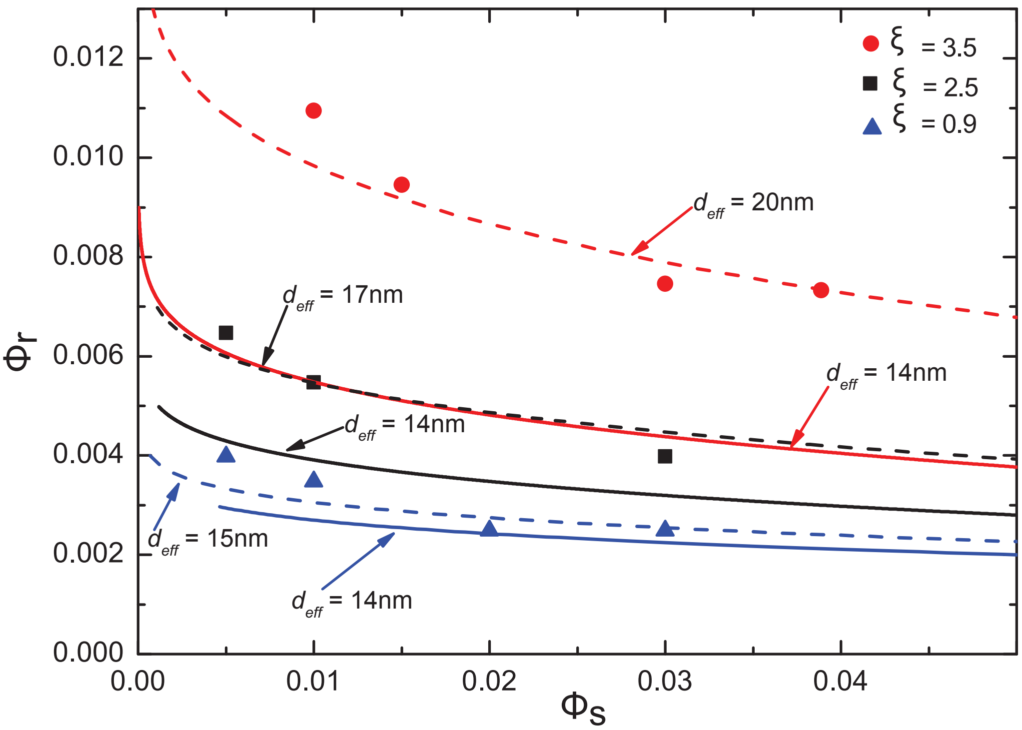

Figure 3.6: *Experimentally determined rod/sphere mixture binodals, for* ξ *= 0.9, 2.5, 3.5 at a fixed effective ionic strength of 25mM. The solid lines are binodals calculated using the Free Volume Theory (FVT). The effective rod diameter* d_{eff} *used is determined by means of the Onsager theory on ideal rods. The dashed lines are a fit of respective experimental data with the* d_{eff} *as fitting parameter also using the FVT.*

4

Equilibrium Phase Behavior

In this chapter we investigated the equilibrium phase behavior of a model colloidal rod/sphere mixture. We determined the location of a two phase (*gas/liquid*) coexistence region and also a three phase coexistence region (*gas/liquid/solid*) in the experimentally determined state diagram. We present a study of free fluid/fluid interfaces and a discussion of the resulting microstructures which are formed after phase separation in the respective regions of the phase diagram.

4.1 Introduction

As highlighted in chapter 2, the depletion interaction plays an important role in determining the equilibrium phase behavior of a binary mixture of colloidal particles. Phase separation can occur at sufficiently high enough colloid concentrations. For the rest of this chapter the colloidal particle species which mediates the attractive force between the second component shall be referred to as the depletant agent. Analogous to atomic systems, bulk phases such as gas-like (dilute in colloids), liquid-like (more concentrated in colloids but still disordered) or solid-like (crystalline) can be observed. Moreover, depending on particle size and shape, phases with complicated microstructures have been observed experimentally [6, 10].

A binary mixture which has not been investigated intensively is the rod/sphere mixture. This is quite surprising when considering the fact that mixtures of rod-like and globular particles are ubiquitous both in nature and in numerous practical applications. In the introduction of this thesis, we reviewed the current state of the work published on the rod/sphere system both from theoretical work and experiments (see chapter 1). Two main regimes were reviewed with respect to size ratio $\xi = L_{rod}/R$, where L_{rod} is the length of the rod and R is the radius of spheres.

The first case is the one in which the rods are extremely small i.e $\xi << 1$, and in the other limit where the spheres are much smaller than the rods, so $\xi >> 1$. This chapter will focus on the intermediate regime $\xi \approx 1$ where there is a lack of systematic experimental investigations of the equilibrium phase behavior of this system.

In order to be able to predict the bulk equilibrium phase behavior of colloidal mixtures a starting point is to obtain the form of the depletion potential acting between the particles in an infinitely dilute system. The Derjaguin approximation is a relatively simple way to obtain a quantitative expression of this inter-particle force. The approximation relates the force that acts between two curved surfaces to the force that would act between two flat surfaces. This is done by progressively using flat discs to approximate the curved surface [20]. The larger the radius of the curved surface is, the more accurate is the Derjaguin approximation. When applied to a rod/sphere mixture the Derjaguin approximation holds for $R \gg L_{rod}$. The mixtures which we investigated fall in the range of $\xi \approx 1$ in which the Derjaguin approach overestimates the rod-induced depletion potential. Yaman et al showed how the depth of the depletion potential becomes shallower as ξ increases using an exact numerical integration method which uses for the calculation of the depletion interaction, a first order approximation of the potential (see section 2.1.2.2) [120]. The relatively shallow potential obtained in rod/sphere mixtures calculated in the ξ regime where the Derjaguin approximation breaks down has been suggested as a posible reason for the lack of phase separation in rod/sphere mixtures [106].

On the other hand Monte Carlo simulations applied to study the bulk phase behavior showed that at high enough rod volume fractions ϕ_r, phase separation occurs and that the resulting phase behavior is a liquid/liquid phase coexistence for $\xi > 0.6$ and a gas/solid phase for $\xi < 0.6$ [15]. In the Monte Carlo simulations (MCS), the rods are assumed to be infinitely thin but in experiments the depletants have a finite rod diameter. A theory that accounts for the finite rod aspect ratio is the Free Volume Theory (FVT) (see section 2.2). Using a rod aspect ratio of 20, the qualitative behavior observed in the MCS was confirmed but interestingly at $\xi \approx 1$ the FVT predicts a three phase coexistence region [112]. Experiments on mixtures of silica spheres and boehmite rods with $\xi = 0.6$ showed depletion induced crystallisation in the bulk and at the wall confirming the FVT predictions [60]. One disadvantage inherent to the experimental system is that the rods had a polydispersity ≈ 40 % hence a ξ which is not well defined. Yasarawan et al observed in the Isotropic/Nematic (*I/N*) coexistence region of the rods, the formation of nematic tactoids interspersed with layers made up of spheres. They used sepiolite rods and silica spheres at a $\xi = 2.7$ [123].

In this chapter we present a study on the equilibrium phase behavior of a rod/sphere mixture in a buffer in which the colloidal particles are neutrally bouyant. We use *fd*, an established model system for mono-disperse colloidal rods, and charge stabilized polystyrene spheres. By preparing mixtures of *fd* and spherical particles of different diameters, we scanned mixtures with several ξ values around 1. We characterized the equilibrium phases just above the theoretically determined binodal line in the region of the phase diagram highlighted in figure 4.1. The phase separation kinetics of a representative state point in the phase diagram studied using confocal microscopy volume scans is discussed in section 4.3.1. After that, the interfacial properties of structures formed after reaching the end stage of phase separation characterized using capillay wave analysis are presented in section 4.3.2 and 4.3.3. The chapter ends with the presentation of the equilibrium phase diagram that we determined experimentally.

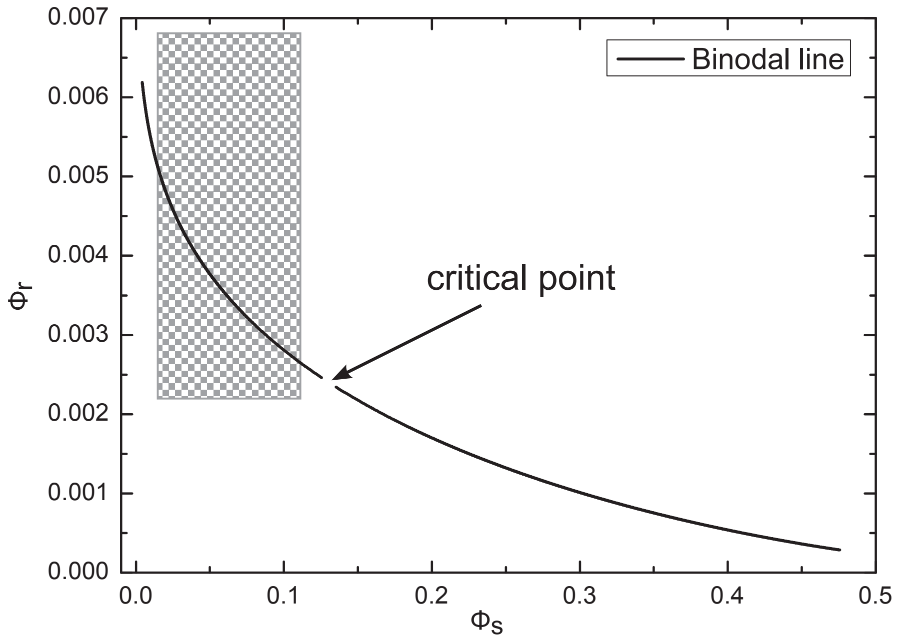

Figure 4.1: *Plot showing the region of the rod/sphere state diagram that was characterized above and below the gas/liquid binodal. The region within the checkerboard rendered rectangle highlights the location of state points that were investigated.*

4.2 Materials and experimental techniques

4.2.1 Experimental System and Setup

Polystyrene spheres of radius 0.5μm purchased from Thermo Fischer Scientific were used to prepare the rod/sphere mixtures. We used *fd* virus, for the monodisperse colloidal rods. The colloidal particles were dispersed in a TRIS-HCl buffer set at a pH value of 8.3 and at a total ionic strength of 25mM. For experiments in which the microspheres are made neutrally bouyant, we prepared the buffer in a D_2O/H_2O mixture. In experiments where we observed the fluctuations at a macroscopic interface between two phases, only H_2O was used and thus the system is no longer density-matched. For a more comprehensive description of the physical properties of the particles please see section 3.2

The fluorescence confocal microscopy volume scans for studying the phase separation kinetics were performed using a 60x water immersion objective on a Olympus IX 71 inverted microscope equipped with a FLUOVIEW FV3-291

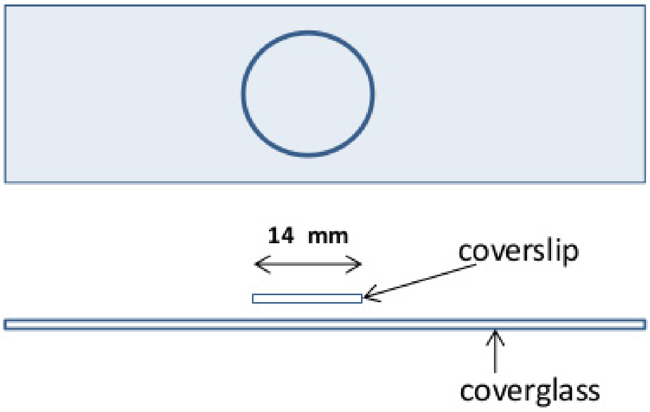

__Figure 4.2:__ Schematic diagram of the thin sample holder used for the characterizaton of the microstructure after phase separation. The top part of the figure is a planar view from the top of the holder showing the glass slide and the coverslip that make up the chamber after sealing with glue. The bottom part of the figure is a view from the side showing the region between the two glass slide where the sample is pipetted onto for observation by optical microscopy.

confocal unit. Mixtures were loaded into capillaries of 100μm path length made of borosilicate glass purchased from Vitrocom. Image stacks 60μm deep behind the coverglass were acquired in 0.5μm stepsizes in the z-direction. A z-stack was acquired every 3 minutes over a period of two hours to ensure that we imaged the phase separation from the very early stages until the system reached equilibrium.

The characterization of the microstructure was carried out using a combination of wide field fluorescence microscopy and confocal laser scanning microscopy (CLSM). The wide field fluorescence measurements were performed on a Zeiss Axioplan 2 microscope with a 63x oil immersion objective. Image acquisition was carried out by means of an Andor Technologies NEO sCMOS fast camera controlled by Mircomanager software [92]. The fluorescence confocal microscopy was performed with a 100x oil objective on a Zeiss Axiovert 200M inverted microscope equipped with a VT-Infintity (Visitech International) confocal scanning unit. Images were acquired using an Andor iXon camera. We prepared sample holders made up of regular coverglasses and circular thin coverslips of diameter 14mm and 170μm thick. Figure 4.2 shows a schematic diagram of the sample holder. 5μl of the sample to be observed is pippeted onto the coverglass then the thin coverslip is placed directly on top of the sample droplet which causes the sample to spread and thus fill the space confined between the coverslip and coverglass by means of capillary forces. The sample is sealed with glue and the resulting average chamber height is $\approx 20\mu$m which is a factor 20 the rod length thus we can rule out confinement effects on the equilibrium phase behavior of prepared mixtures. The thin chamber has the advantage of making it possible to image inside the highly scattering samples since the microspheres are not optically-matched.

The measurements to study the interfacial properties of the microstructures formed after phase separation were carried out in observation chambers described in the preceding paragrapgh. An hour after sample preparation, when a phase separating mixture reaches steady state (see section 4.3 where the phase separation kinetics is discussed), the sample is placed onto an AXIOPLAN 2, Zeiss microscope equipped with a 100x, 1.4 Numerical Aperture immersion oil objective. The sample is illuminated by a HBO 100 Mercury lamp. The experimental protocol to determine the interfacial properties of the respective phases consists of acquiring 1000 frames at 20 frames per second using a sCMOS Andor NEO camera. In the fluorescence images, *fd* viruses are not visible since they do not fluoresce but one sees spherically shaped clusters, consisting of small spherical particles in a background of the rods. We set the imaging plane to coincide with the equator of the cluster and obtain fluorescence time series of the fluctuations (see figure 4.3). To get the fluctuation spectrum density, we threshold the images and use an edge detection algorithm in ImageJ, a java based image processing toolkit. After obtaining the discretized contour for each frame, we use JFilament [96] to get the cartesian coordinates.

For the set of experiments that were performed in rod/sphere mixtures at ϕ_{col} = 0.1, the colloidal particles were dispersed in H_2O and thus the spheres are no longer density matched. The gravitational length which is defined as $l_g = k_BT/G^*$ is in this case $6\mu m$. Here k_BT is the energy due to thermal motion and G^* is a buoyant colloid weight. For a particle of diameter 500 nm, at such a gravitational length, motion due to gravity of a single particle is at least by a

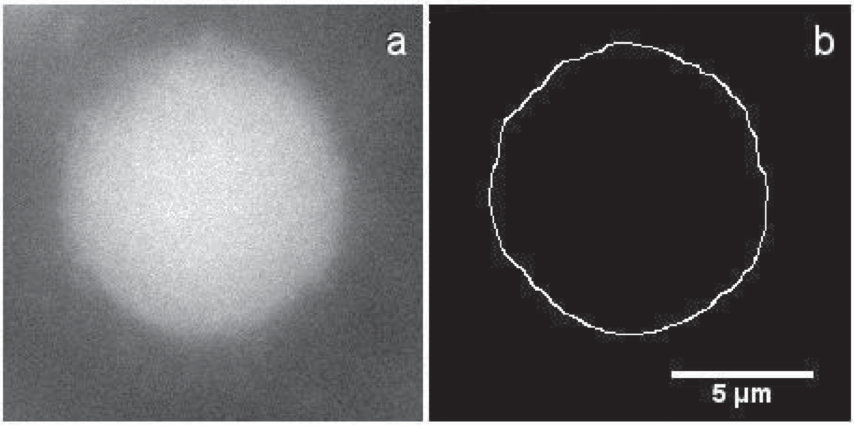

Figure 4.3: *a) is a snapshot of a time series showing a typical cluster after reaching steady state in a phase separating mixture. The rods are not fluorescently-labelled and are thus invisible. b) is the contour of the cluster at its equator plane. The contour is decomposed into a discretized Fourier series and used in the determination of the Power Spectral Density.*

factor 10 greater than that due to thermal motion. The effect of gravity on the system can no longer be neglected.

We constructed rectangular shaped sample holders of dimensions 15 x 1 x 0.17 mm, with walls made from 170μm coverslip glass slides to facilitate the imaging. Upon preparing mixtures at four different statepoints represented by the points labelled (*vii*-*x*) as shown in figure 4.5, we vortexed the sample and filled the measurement cell. The cells were sealed with glue and placed in a vertical position. As the phase separation in the rod/sphere mixture proceeds, the formed colloidal liquid phase droplets are subject to gravity driven flow [2]. The droplets begin to collect at the bottom of the measuring cell and they coalesce leading to the formation of a macroscopic horizontal interface between the colloidal liquid and gas phases. After reaching equilibrium, The holder is then mounted on a horizontal confocal scanning laser microscope (CSLM, Zeiss Exciter) for the imaging of thermal capillary waves at the fluid-fluid interface [1]. After allowing the phase separated sample to equilibrate over night, we follow the thermally induced undulations by recording a time series of 5000 frames. The confocal microscope is setup in a horizontal configuration and we image capillary waves in a focal-plane parallel to the x-z plane see the top right insert in Fig. 4.4. A

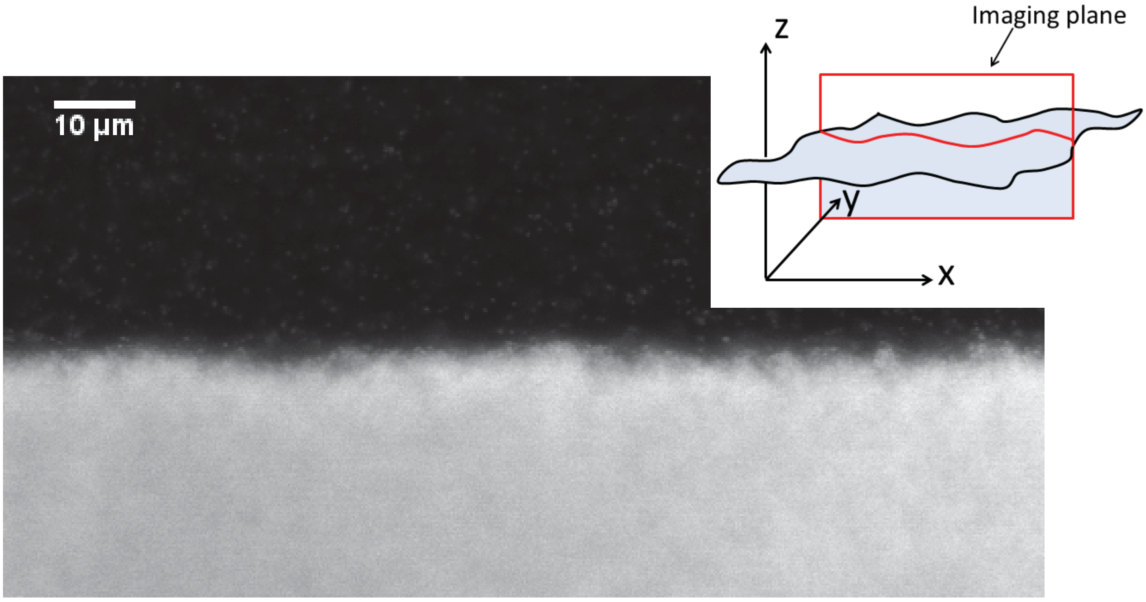

Figure 4.4: A typical snapshot of a time series taken using a horizontal confocal microscope showing a colloidal liquid phase at the bottom and a gas phase at the top. fd virus is not fluorescently labelled thus not visible in this snapshot. Insert on the top-right shows the imaging plane in which the fluctuations are observed.

typical frame in the series is shown in Fig. 4.4 where the colloidal liquid phase is at the bottom of the image and above a sharp interface is the colloidal gas phase.

4.3 Results and discussion

An overview of the experimental results which will be discussed in this section is presented in figure 4.5. The figure shows part of the experimentally determined phase diagram in a mixture at a size ratio of $\xi = 3.5$. The roman numerals above the gas/liquid binodal line represent the rod/sphere mixture compositions that were used for the characterization of the equilibrium phase behavior. In each subsection we will make reference to the figure 4.5 and give a description of the microstructure being studied, then the experimental technique that was used to investigate the equilibrium properties of the microstructure and then present the results.

4.3.1 Phase separation kinetics and morphology

In chapter 3 we determined the location of gas/liquid binodals for rod/sphere mixtures for a range of size ratios ξ running from 1,8 to 3,5. It was observed that in mixtures that phase separate, it takes $\sim$ 60 minutes for the system to reach steady state. Diffusive Wave Spectroscopy measurements showed that the mean relaxation time τ of the correlation functions which we measured during the phase separation process initially increased before it reached a plateau value (section 3.3.1). The constant value of τ at later stages of the phase separation hints to the fact that the microstructure attains an equilibrium size after full phase separation. We also observed that the turbidity of the samples decreases throughout the demixing process which allowed the imaging of the bulk phase behavior by optical microscopy methods. In this subsection we report the results of following the formation of structures during phase separation by confocal fluorescence microscopy. From the image analysis we determine the phase separation kinetics.

The composition of the mixture discussed in this subsection is represented by the statepoint labelled (*iii*) in figure 4.5. We observed that the phase separation occurs via a formation of nuclei made up of the spherical colloids that grow into larger clusters. The clusters continue to grow in size until they attain a narrow size distribution an hour after the system is quenched. We were not able to observe the initial stages of the demixing due to the time it takes to load the mixture into the sample holder and then mounting it onto the microscope. A typical time series of images showing the growth of the clusters is shown in figure 4.6(a). We then determined the average volume that each cluster occupies using the confocal z-stacks recorded every three minutes. The analysis was carried out using a three dimension object counter which is an ImageJ plugin [16]. In the initial stages of the phase separation, the volume of the spherically shaped clusters grows linearly in time and then caps off reaching a plateau as seen in the plot of average cluster volume versus time presented in figure 4.6(b).

Phases which are made up of stable of clusters consisting of charged spherical

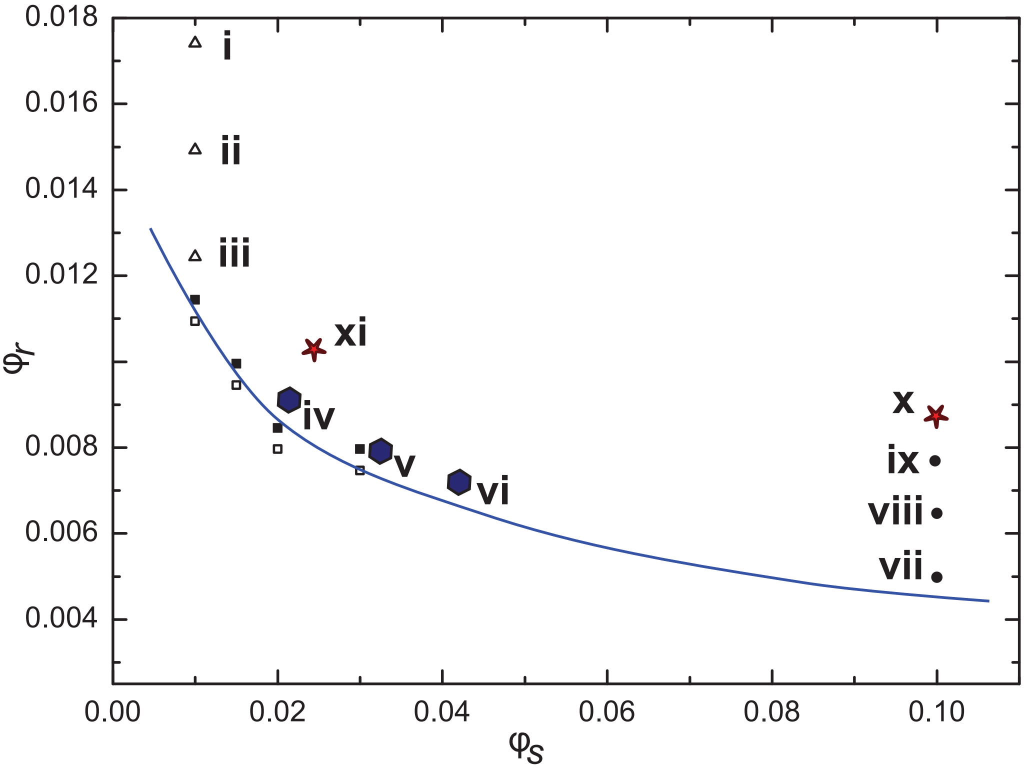

Figure 4.5: *Plot showing the experimentally determined gas/liquid binodal line for a mixture at size ratio* ξ *= 3.5. The open and closed square symbols represent mixtures which are stable and unstable respectively. The solid blue line is a guide to the eye showing the location of the gas/liquid binodal. Statepoints (i-ii) phase separated into solid/liquid/gas phases that coexist in the form of clusters having a solid core covered by a thin liquid layer which decreases in thickness the further away the point is from the gas/liquid binodal. The mixture with the composition represented by the statepoint labelled (iii) is in the two phase coexistence (gas/liquid) region of the phase diagram. The phase separation mechanism and kinetics for the point (iii) are dicussed in section 4.3.1. The three blue hexagonal points just above the gas/liquid binodal line which are labelled (iv-vi) represent the statepoints where contour analysis of clusters was performed (see section 4.3.2). The three circular symbols at* ϕ_s*=0.1 which are labelled (vii-ix) represent mixture compositions where the interfacial tension was determined for macroscopic interfaces between the gas and liquid phases (see section 4.3.3). The statepoint (x) is a mixture in which the three phase coexistence region is observed and it was not possible to obtain a clean horizontal macroscopic interface. The mixture represented by (xi) is also in the three phase coexistence region but at a* $\phi_s = 0.025$ *and shows crystalline regions with clear grain boundaries which separate crystallites having different lattice orientation (see section 4.3.4).*

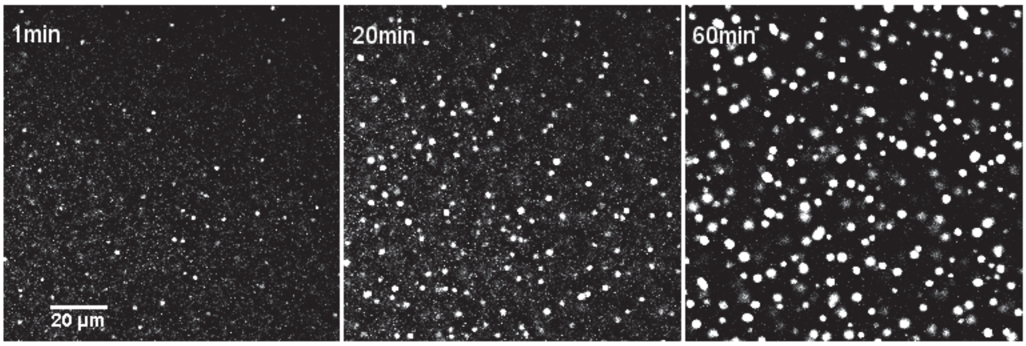

(a) Time series of cluster growth

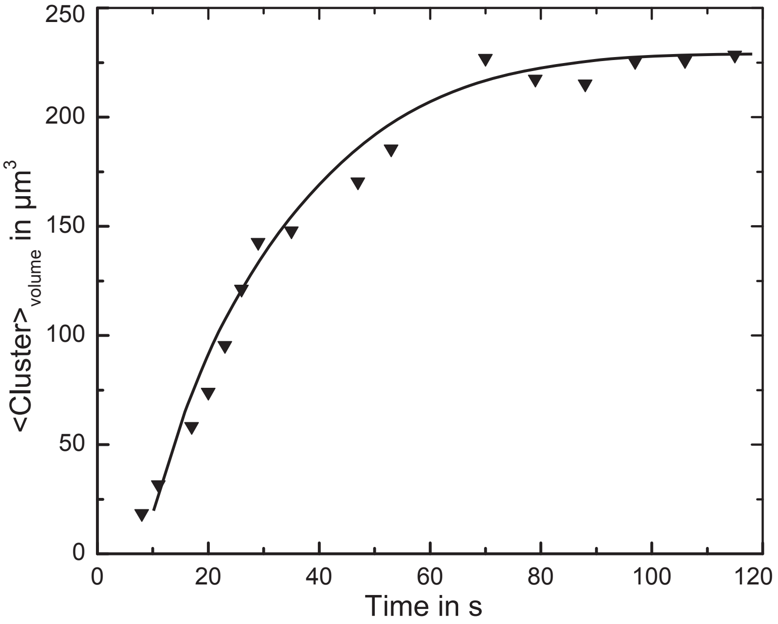

(b) Average cluster volume vs time

Figure 4.6: *(a) Video microscopy time lapse at a fixed imaging plane during the phase separation of a mixture having a composition represented by the statepoint (iii) in figure 4.5. (b) The average cluster size determined from confocal z-stacks plotted against time while the mixture phase separates.*

colloids have been observed in several colloid/polymer mixtures [94, 99, 124]. The competition between the long-ranged double layer repulsion and the relatively shorter-ranged depletion attraction which has an effective range $\ll R_{colloid}$ is used to explain the resulting bulk phase behavior. The range of the attraction when using polymer chains as depletants is set by the radius of gyration of the chains which is typically of the order of < 50nm. Unique to our experimental system is that by using *fd* virus as a depletant which has a contour length of

$\approx$ 880nm, we induce a relatively longer-ranged attraction compared to the one induced by short polymer chains. In our rod/sphere mixtures we thus have double layer repulsion due to the charged polystyrene spheres and an induced attraction with an effective range $\approx R_{colloid}$. Both theoretical work and simulations predict that in systems with such competing interactions, an equilibrium cluster phase is can coexist together with a gas phase [43, 44].

Our rod/sphere mixture undergoes microphase separation into clusters that are rich in the spherical particles at sphere volume fractions in the range of $\phi_s <$ 0.02. The probability of clusters coalescing which would result in a macroscopic liquid phase is relatively low. The reason for the improbable coalescence events is explained by the fact that the diffusion of the clusters above a critical size is hindered within the background host which is rich in rod-like *fd*-virus. The concentration of rods is above the overlap concentration at the statepoint being discussed. We suggest that the existence of the stable clusters in our rod/sphere system cannot be explained completely by only applying the theory postulated by Groenewold et al; which attributes this *sea of cluster phase* mainly to the competition between the electrostatic repulsion and depletion induced attraction. We suggest that the clusters are actually thermodynamically stable liquid-like droplets that coexist together with a gas phase. We arrive at this conclusion because at the cluster/gas phase interface we observe a dynamic exchange of single particles between the two phases. Preliminary experiments carried out using high resolution confocal microscopy suggest that this exchange is in a dynamic equilibrium but we do not as yet have sufficient quantitative proof of this.

4.3.2 Analysis of thermally induced fluctuations at cluster interface

As was already shown in the previous subsection, mixtures at low sphere volume fraction ϕ_s for high enough rod concentrations ϕ_r phase separate into a stable sea of liquid-like clusters rich in colloidal spheres and a rod-rich background which is poor in spherical particles. In this subsection we report the results of the characterization of interfacial properties of the clusters. We recorded a time series of the thermally-induced fluctuations at the equator plane of individual clusters using video microscopy (see figure 4.3). Each cluster is made up of $\approx$ 1000 polysytrene particles and in the fluorescence images the cluster looks like a liquid droplet in a host medium of a different viscosity. Statepoints in the phase diagram for which the fluctuations were recorded are shown in figure 4.5 and are depicted by the blue hexagonal points labelled with roman numerals (*iv*-*vi*). A detailed description of the experimental protocol followed can be found in section 4.2.

Figure 4.7 shows a representative fluctuation spectrum which is plotted versus the wave vector q_x for a mixture with the composition represented by the blue point labelled (*vi*) in figure 4.5. The fluctuation spectra of statepoints *iv* and *v* qualitatively look similar to the spectra obtained for the statepoint (*vi*). In order to relate the spectral coefficients $\langle|u(q_\perp)|^2\rangle$ to the interfacial tension γ, we use equation 4.1 [82].

$$\langle|u(q_\perp)|^2\rangle = \frac{k_B T}{2\gamma}\left[\frac{1}{q_x} - \frac{1}{\sqrt{\frac{\gamma}{\kappa} - q_x^2}}\right] \tag{4.1}$$

where k_B is the boltzmann constant, γ is the interfacial tension and κ is the bending rigidity. The two fitting parameters are γ and κ . For a colloidal rod/sphere mixture the bending rigidity κ is infinitely small and can be neglected since the curvatures of interfaces are also small which is due the characteristic ultra-low interfacial tension observed in mixtures of colloidal particles [54]. The first few modes are discarded when fitting the Power Spectral Density (PSD). This is done to account for the significant difference in the first five modes between the theoretically calculated fluctuation spectra of a spherical geometry and that of a planar one [82]. Above the first five modes the theoretically calculated spectra become indistinguishable within experimental error both for the spherical and planar geometry. This makes the performing of the analysis as a planar

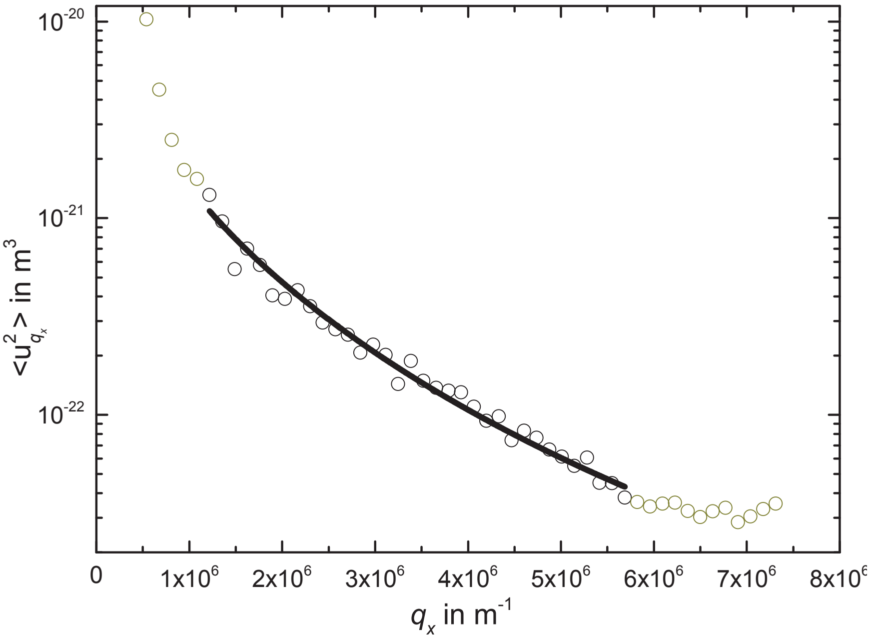

Figure 4.7: *Plot of fluctuation amplitude* $< u^2_{q_x} >$ *versus wave vector* q_x *of a typical cluster in a colloid/rod mixtures of composition* ϕ_{col} *= 0.04 and* ϕ_r *= 0.008. The solid line is the fit of the data yielding a* $\gamma = 9.7 \cdot 10^{-7}$ *N/m.*

problem a good approximation to the three diemsional case. At high-q, the cut-off is set by the optical resolution of the imaging setup and the pixel size of the camera. In our imaging system this is of the order of q $\sim 10^{-7}\mathrm{m}^{-1}$.

Table 4.1: *Ultra-low Interfacial tension of liquid-like clusters of mixtures with compositions shown in figure 4.5.*

Statepoint	iv	v	vi
$\gamma\ (N/m)$	$7.3 \cdot 10^{-7}$	$7.02 \cdot 10^{-7}$	$9.7 \cdot 10^{-7}$

Figure 4.7 shows the fit of the experimentally determined power spectral density for a mixture with ϕ_{col} = 0.04 and $\phi_r = 0.008$. The point measured is depicted by the blue point labelled (vi) in figure 4.5. The solid line shows the fit with a $\gamma = 9.7 \cdot 10^{-7}$ N/m. Table 4.1 shows the corresponding determined interfacial tension of mixtures at the state points depicted by the roman numerals (*iv*),(*v*) and (*vi*) in figure 4.5. In colloidal systems the interfacial tension can be estimated by simple scaling arguments. For colloidal particles of radius r_{col}, the interfacial tension $\gamma \simeq k_B T / r^2_{col}$. We used spheres of r_{col} = 250 nm which re-

sults in $\gamma \simeq 5 \cdot 10^{-8}$ N/m. The experimentally determined interfacial tension for our rod/sphere mixture is overestimated by a factor 10. This could partly be due to the fact that we reduce the three dimensional cluster into a two dimensional problem. We are thus only sensitive to the fluctuations in the plane of the equator which do not account for all the possible modes of the thermally induced undulations at the interface. Despite the discrepancy in magnitude, we obtain ultra-low interfacial tension which has been determined in similar colloid/polymer mixtures using independent methods such as the spinning drop method [18].

4.3.3 Thermally-induced fluctuations at macroscopic interfaces

In the previous section 4.3.2 we characterized the interfacial properties of the clusters formed in mixtures at relatively low $\phi_s \leq 0.04$. In mixtures at $\phi_s \geq 0.04$, the average cluster size increases and after the large clusters coalesce they can form a single homogeneous liquid phase. In this section, we characterize the interfacial properties of the liquid phase by analyzing thermally-induced fluctuations that occur at a macroscopic gas/liquid interface. We also compare values of the interfacial tension γ determined by two independent methods. One method is the capillary wave analysis method which is applied in the case of horizontal macroscopic gas/liquid interfaces. The second method is the Power Spectral Density analysis of spherically shaped clusters (see section 4.3.2). We carry out the experiments in a buffer prepared in pure H_2O thus mis-matching the density of spheres in the experimental system. We prepared three mixtures with compositions represented by the three state-points labelled (*vii-ix*) in figure 4.5. A horizontal macroscopic interface is formed following phase separation between a fluid-like phase, which is rich in spherical colloids, and a gas-like phase (see figure 4.4). The volume fraction of spheres in the mixtures was kept fixed while we varied the volume fraction of rods ϕ_r. Figure 4.8 shows the probability distribution of the height-height displacement of the interface about an average height for the two mixtures of different rod volume fraction ϕ_r. Clearly increasing ϕ_r

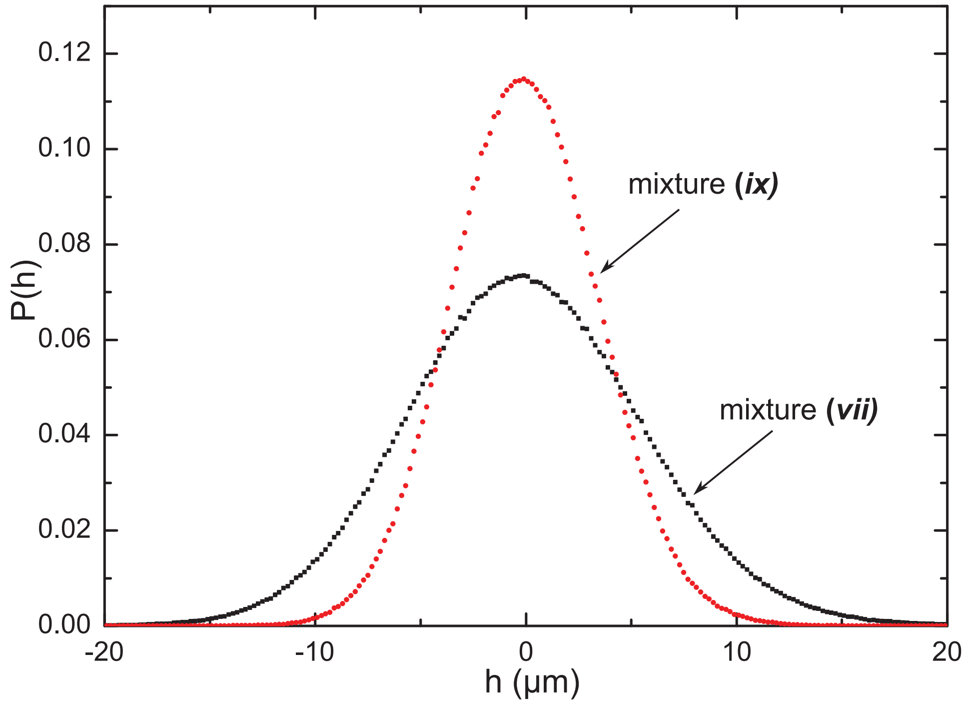

Figure 4.8: *The probability distribution function of the amplitude of the height displacements (h) about a mean interface height for two mixtures with rod/sphere compositions represented by the roman numerals (vii) and (ix) in figure 4.5. The distribution of displacement heights is much broader for the statepoint (vii) which is closer to the binodal line.*

results in fluctuations with a lower amplitude and a height distribution that has a much smaller standard deviation compared to the mixture at lower ϕ_r.

We determined both the static and dynamic correlation functions following the experimental protocol outlined in section 4.2. The theoretical background required to analyze and interpret the results is discussed in section 2.3. The static correlation function $g_h(x)$ is defined as

$$g_h(x) = \frac{k_B T}{2\pi\gamma} K_0 \left(\frac{x}{L_c} \right) \tag{4.2}$$

where k_B is the Boltzmann constant, γ is the interfacial tension, L_c is a characteristic length called the capillary length and K_0 is a Bessel function which is written as a function of x/L_c. Experimentally determined static correlation functions $g_h(x)$ are presented in figure 4.9. We fit the experimentally obtained

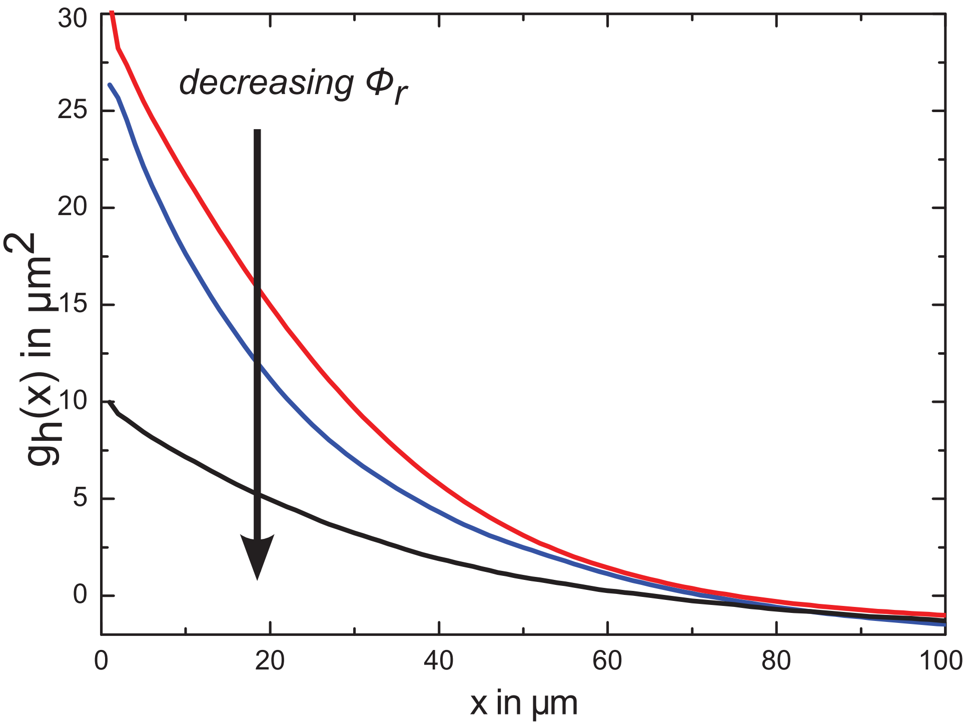

Figure 4.9: *Experimentally determined height-height static correlation functions $g_h(x)$ measured for three statepoints vii, ix, x shown in figure 4.5. The red line is for the statepoint ix, the blue line is for the statepoint viii and the black line stands for the statepoint vii. All mixtures are at a fixed sphere volume fraction ϕ_s but different rod volume fraction ϕ_r.*

static data using equation 4.2, and obtain the interfacial tension γ. The dynamic correlation function $g_h(t)$ is defined as

$$g_h(t) = \frac{k_B T}{2\pi\gamma} \int_0^{\bar{k}_{max}} d\bar{k} \frac{\bar{k}}{1+\bar{k}^2} exp(-(\bar{k}+\bar{k}^{-1})t/2\tau) \tag{4.3}$$

where $\bar{k} = L_c k$ and the relaxation time τ is given by $\tau = L_c\eta/\gamma$ [1]. By fitting the experimentally determined $g_h(t)$ by equation 4.3 we also obtain an interfacial tension.

Table 4.2 shows the interfacial tension determined using the static $g_h(x)$, and dynamic $g_h(t)$ correlation functions. The fitting of the corresponding correlation functions resulted in comparable values of γ. There is however a two orders in magnitude difference in the the values of γ obtained using the power spectral decomposition method (Table 4.2), compared with the values from the height-

Table 4.2: *Ultra-low Interfacial tension of the macroscopic interface between the liquid phase and a gas phase in mixtures with compositions shown in figure 4.5 determined from fitting both the static and dynamic correlation function.*

Statepoint	γ from fit of $g_h(x)$ (N/m)	γ from fit of $g_h(t)$ (N/m)
vii	$4.04 \cdot 10^{-9}$	$6.26 \cdot 10^{-9}$
viii	$4.73 \cdot 10^{-9}$	$8.2 \cdot 10^{-9}$
ix	$1.22 \cdot 10^{-8}$	$1.96 \cdot 10^{-8}$

height correlation function analysis (Table 4.1). The correlation function analysis has the advantage that the gas/liquid interface can to a good approximation be considered as a continuum since the length along the interface L_{int} where the capillary waves are measured is much larger than the radius of a single spherical colloid r_c i.e ($L_{int} \gg r_c$). In the method used for analyzing the contours of the spherically shaped clusters, whose typical radius is $\sim 5\mu$m, single spherical particles can be resolved leaving and entering the liquid phase during the image acquisition. For the latter case, assuming that the interface is a continuum is a poor approximation. Furthermore the leaving and entering of the smaller spherical particles into and out of the liquid phase introduces artifacts during the edge detection protocols rendering this method less accurate. Nonetheless both methods yield an ultra-low interfacial tension $\approx 10^{-7} - 10^{-9} N/m$ which has been measured in similar colloid/polymer mixtures [18]. In the next section we will present experimental results that show a region of the phase diagram for a rod/sphere mixture at $\xi = 3.5$ in which three phases (solid/liquid/gas) coexist.

4.3.4 Three-phase coexistence

So far in this chapter we have characterized the equilibrium phase behavior of statepoints that lie relatively close to the gas/liquid binodal in a mixture at a size ratio $\xi = 3.5$. Indeed after phase separation we observed a liquid-like phase that is rich in spherical particles coexisting with a much more dilute gas phase. In section 2.2 we introduced the Free Volume Theory (FVT) which is a tool used to calculate the phase behavior in mixtures of colloidal particles [63,64]. The FVT predicts a fluid/fluid coexistence for mixtures having a size ratio $\xi > 0.6$ which

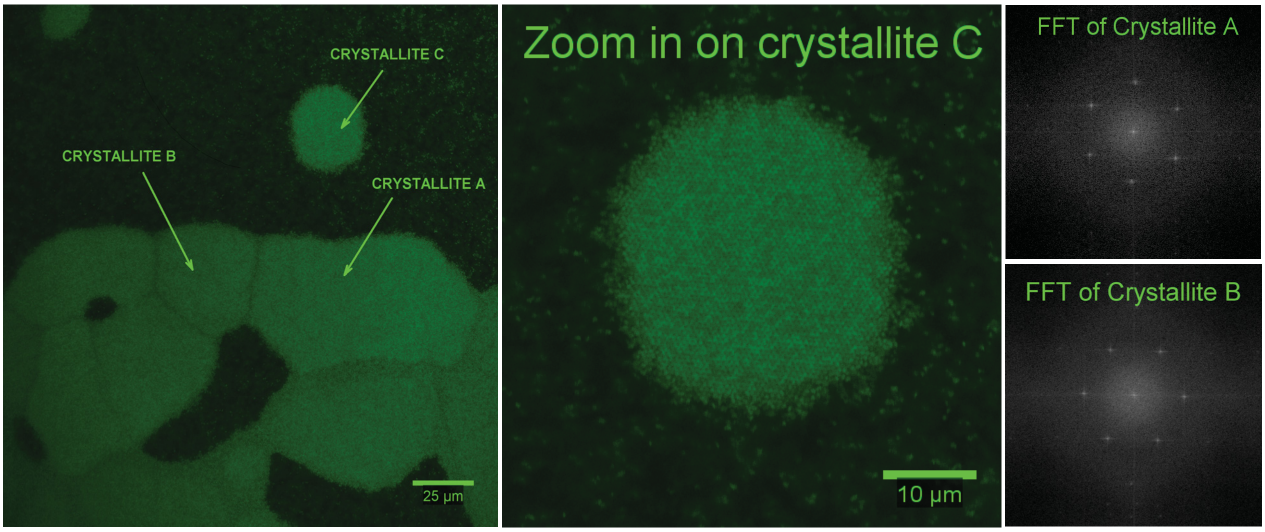

Figure 4.10: *(left figure) A confocal image of a mixture at a size ratio $\xi = 3.5$ showing clusters that have a solid crystalline core which is covered by a thin liquid-like outer layer. Distinct grain boundaries are observed whenever two crystallites that have different lattice orientations collide with each other. (middle figure) A zoomed-in image of crystallite C showing the highly ordered solid core and the more liquid-like film at the edges of the cluster. Both the solid and liquid outer layer coexist together with a much more dilute gas phase. (most right figure) Fast Fourier transform of clusters A and B respectively showing evidence of typical colloidal crystal packing.*

is in agreement with what we observe for our rod/sphere mixture at a size ratio $\xi = 3.5$. For the size ratio that we studied the FVT also predicts a three phase coexistence region within the phase diagram which is bounded from below by the gas/liquid region and above by the gas/solid coexistence region [112]. In this section we present the results of the characterization of statepoints which are found deeper into the phase separating region where we found experimental evidence that suggests a three phase coexistence region.

We investigated the phase morphology of the statepoint (*xi*) in figure 4.5) which lies just above the gas/liquid region of the experimentally determined phase diagram. The dispersion was prepared in a buffer that was not density matched to allow the dense colloidal phases formed after phase separation to collect at the bottom of the observation microscopy slide which we mount on a horizontal confocal microscope setup. It was observed that the initial stages of the phase separation occurred via the formation of clusters that grow in time just as in the case of mixtures that were prepared close to the binodal line. The main difference however is that the clusters formed exhibit a solid crystalline core covered by a liquid-like melted layer several colloidal diameters thick. Due to gravity, the clusters gradually sediment to the bottom of the sample holder but instead of coalescing into one homegeneous phase as in the case of the purely liquid-like clusters, grain boundaries are formed which separate the crystallites having different crystal lattice orientation as shown in figure 4.10. Fast Fourier transform performed on the images of the solid-like core shows a regular hexagonal pattern which is characteristic of a colloidal crystalline order. A gas phase is observed which coexists together with the gas/liquid phase. This experimental evidence leads us conclude that we have located the three-phase coexistence region in our colloidal rod/sphere mixture which is predicted by the Free Volume Theory [112].

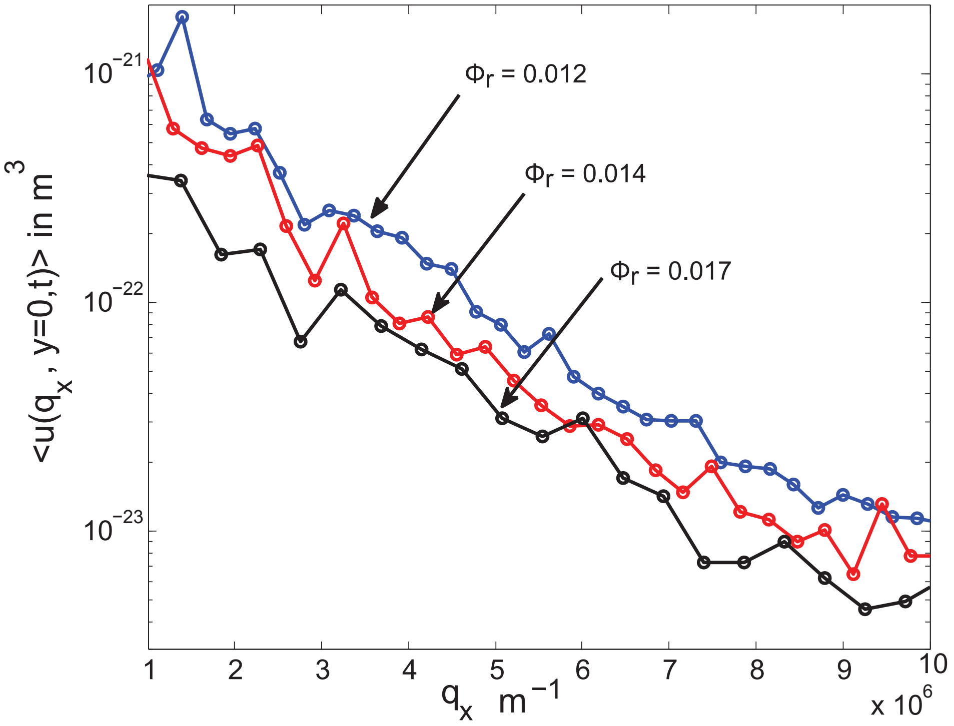

Figure 4.11: *Fluctuation spectra determined for the liquid-like melted layer covering the solid crystalline core of clusters observed in the three-phase cosxistence region of phase diagram. The rod/sphere mixtures were all prepared at a fixed volume fraction of spheres ($\phi_s = 0.01$) at three different rod concentrations (ϕ_r).*

We characterized the thin liquid film on top of the crystalline core phase by analysing the fluctuations of the melted layer at statepoints labelled (*i-iii*) in figure 4.5. The fluctuation spectra at the interface between the liquid outer layer of the solid-core of the clusters and the gas phase is shown in figure 4.11. The spectra have the same shape as those of the purely liquid-like clusters measured in section 4.3.2. This supports what we observed in the case of the macroscopic interfaces where the interfacial tension γ increased with increase in ϕ_r which in turn led to a decrease in displacement heights of the interface (see section 4.3.3). Interestingly, during the initial stage of the phase separation there is no evidence of a solid phase in the clusters from the confocal microscopy images. The clusters appear to behave as dense liquid droplets. It is only when phase separation goes to completion that the crystalline core becomes clearly visible. An independent experiment which we performed that supports this conclusion is presented in the chapter 5.3.2. Ten Wolde et al have shown how critical density fluctuations in dense liquid droplets in the fluid/fluid coexistence region can lead to crystallite formation inside the droplets for systems with short-ranged attraction using numerical simulation methods [117]. In chapter 5.3.2 we will show what we believe is an experimental observation of such crystal nucleation and growth which occurs within dense liquid-like clusters.

4.3.5 Phase Topology

As mentioned at the outset of this chapter, the goal was to map out the equilibrium phase behavior of the colloidal rod/sphere mixture consisting of rod-like *fd* virus and charge stabilized polystyrene spheres. We studied in our experiments a narrow colloidal sphere concentration window namely $\phi_s \leq 0.1$. We were limited to this range by the fact that the polystyrene spheres we used are not refractive index matched and thus the highly scattering particles make charaterization of the sample using optical microscopy almost impossible at very high ϕ_s. The experimentally mapped out phase diagram is shown in figure 4.12.

Although the fact that anisotropically shaped particles make excellent depletion agents has been known since the seminal work of Asakura and Oosawa [7] in the 50s, there has been a lack of suitable experimental model systems where this could be systematically explored. The phase diagram we mapped out clearly highlights the efficiency of rod-like particles as depletants. Rod volume fractions $\phi_r \approx 0.002$ are already sufficient to induce phase separation whereas when using polymers or smaller spherical colloids as depletants at least a factor 10 higher in concentration will be required to induce strong enough depletion forces. Furthermore, relatively small increases in ϕ_r at a fixed ϕ_s lead to pronounced differences in the phase morphology. This is seen for example in the phase diagram at sphere volume fractions $\phi_s < 0.03$ where the transition from a stable gas/liquid phase into a three phase coexistence region is induced by $\sim 5\%$ increase in ϕ_r. It is also clear to see that the phase behavior of the rod/sphere mixture is indeed rich considering that we only studied a very small window but we were able to observe a (gas/liquid), (gas/liquid/solid) and (gas/crystal) phase separation. With spherical particles that can be index matched with the buffer it would be possible to determine the complete rod/sphere phase diagram and then compare this to predictions made by the Free Volume Theory. Refractive index-matched particles would also make it possible to follow particle ordering within clusters as a function of time and precisely determine when the dense liquid core in the 3 phase region transforms into the crystalline core. Although *fd* wild type is an excellent model for colloidal rods the mutant Y-21M is a more ideal rod. The mutant is less flexible having a persistence length ~ 10 times its contour length. It would be very interesting to determine the location of binodals using the more rigid Y-21M and check if deviations with the FVT will decrease.

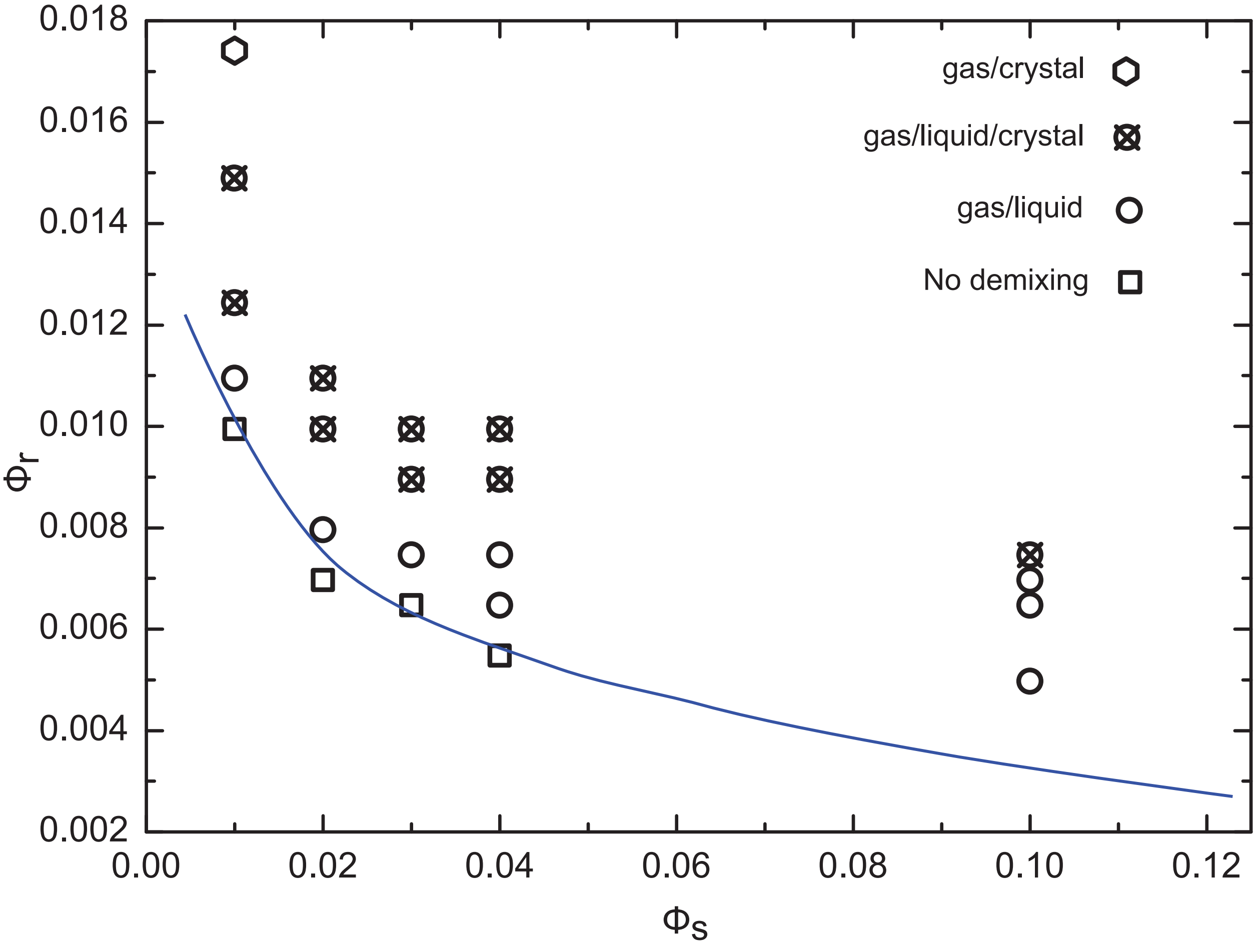

Figure 4.12: *Part of the rod/sphere phase diagram for a mixture of size ratio $\xi = L_{rod}/R =$ 3.5. The blue line is a guide to the eye showing the location of the experimentally determined gas/liquid binodal line. Above the binodal line is a region where the mixture becomes unstable and phase separates into a gas/liquid tha coexist at equilibrium. Increasing rod volume fraction ϕ_r a three phase coexistence region is observed (gas/liquid/crytal). At low ϕ_s and high ϕ_r a gas/crystal phase is the thermodynamically equilibrium state.*

5

Mixtures of rods and spheres under shear flow

We investigated the internal structure of clusters rich in spherical particles which are formed after phase separation in rod/sphere mixtures. We studied clusters formed in the two phase coexistence region (gas/liquid) and the three phase (gas/liquid/solid) region of the experimentally determined phase diagram. We probe the structure using a home built cone/plate shear cell that is mounted on a confocal microscope allowing real space and time measurements of the flow properties of the clusters. We show that the clusters in the two phase region deform as pure liquid droplets and we compare the experimental observations to theoretical models on liquid droplet deformation. For the clusters in the three phase region, we show that they deform following a mechanism which resembles the tip streaming effect. Finally we present experimental evidence of the formation of crystal nuclei within purely dense fluid clusters found in the 3-phase coexistence region of the rod/sphere state diagram.

5.1 Introduction

Complex colloidal dispersions are abundant both in naturally occurring systems and also in many practical applications. Examples of naturally occurring systems are blood, and the cytoplasm of a living cell [30]. Practical systems which are made up of dispersions of colloids include drug delivery systems for medical purposes [56, 76], paints, drilling fluids [71, 104] and in the food processing industry in the form of proteins and polyscaccharides [27]. The understanding of the phase behavior of such dispersions is thus not only important from a fundamental research point of view but it is also essential for many applied purposes. This need has prompted an active interdisciplinary field of research which approaches the study of colloid physics from an experimental, computer simulations and theoretical perspective [69, 70].

The complexity of the physics of colloidal dispersions can be classified using a general scheme [68, 69]. In the first instance we consider the degree of complexity of the colloidal system itself. This degree of complexity considers the shape, the concentration of particles and the form of interaction potential whether it is attractive or repulsive or if it is a superposition of both. The system complexity can be further increased by dispersing mixtures of anisomeric particles. We can also define the complexity of the problem. The criteria for making this classification is whether we study the thermodynamic behavior of the system in the absence of external fields that can mechanically perturb the system or we consider the thermodynamic behavior in the presence of external fields such as magnetic, optical, confining geometries and shear flow.

The equilibrium phase behavior of colloidal dispersions is very rich and is not yet fully understood. In the first part of this thesis we presented a review on the phase behavior of simple spherical particles and also for colloid/polymer mixtures. We increased the system complexity by replacing the polymers in the mixtures with nearly ideal rods and we determined the equilibrium phase behavior. In all the discussions the stability of the dispersions was investigated under quiescent conditions. Interestingly though, at the colloidal length scale (1-10 nm to 1-10 μm) the systems fall under a class of materials known as *soft* matter. Such soft materials are more susceptible to deformation compared to condensed molecular systems and in many practical applications mixtures of colloidal particles are always subject to some external fields such as shear, magnetic and optical fields. Shear flow is more common and it is easier to realise in a controlled fashion under normal laboratory conditions so we will restrict our discussion to the influence of shear on the phase behavior of colloidal dispersions.

In colloidal dispersions shear flow can either destroy structure or induce their formation. For example steady shear flow melts away the ordering in dispersions of colloidal crystals made up of simple spherically shaped charged particles [4]. On the other hand shear has been observed to induce ordering in liquid-like phases made up of nearly hard spheres that are subjected to an oscillatory shear at low strain amplitude [5, 119]. Holmqvist et al showed that growth rates and induction times of crystal formation exhibit a maximum which depends on the rate of shearing in dispersions of charged silica particles [51]. For a more comprehensive review on the literature that discusses flow induced structure in colloidal suspensions see reference [111].

Shear flow couples more strongly to the orientation of anisometric particles than in the case of their spherical counterparts. Examples of anisometric particles are colloidal rods and disc shaped particles also known as platelets. Under equilibrium conditions such anisometric particles can form lyotropic liquid crystalline phases [85]. At low concentrations particles have random orientations but as concentration increases particles start to align with the longer axis pointing on the average in one preferred direction. The first ordered state after the isotropic phase is known as the nematic phase. Smectic and columnar phases can also be observed at higher particle volume fractions. In the case of colloidal rods it has been shown theoretically that shear flow can shift the Isotropic-Nematic (I-N) coexistence to lower concentrations [23, 77]. Lenstra et al observed experimentally the predicted displacement of the I-N spinodals using dispersions of *fd* viruses [65]. The flow-induced rod alignment in suspensions of *fd* virus leads to a decrease in the viscosity with the increase in shear rate (shear thinning) [41]. This decrease in the viscosity has an influence on the flow behavior and could lead to flow instabilities. Kang et al observed in *fd* dispersions formation of shear bands in the vorticity direction using an optical couette shear cell and they also managed to determine the full non-equilibrium phase diagram [57] of the rod-like viruses. Similar hydrodynamic instabilities are also observed in dispersions of worm-like micelles and platelets [45].

The complexity of the problem can be increased by shearing multi-component dispersions. The theoretical and experimental knowledge of the flow behavior of pure colloidal suspensions serves as the framework upon which we can explain the phenomena observed in mixtures subjected to shear flow. One example of a multi-component dispersion is a solution of Worm-Like Micelles (WLMs) where spherical nanoparticles at volume fractions ($\sim$ 1 percent) are added to the disperion [49,74]. The addition of the nanoparticles to the solution of WLMs increases the zero-shear viscosity and the longest relaxation time. The modification of the flow behavior is explained by considering that micelle-nanoparticle juctions are formed in the network which significantly influences the relaxation mechanisms of the WLMs network. In systems where spherical particles are suspended in a visco-elastic host medium the formation of 2-Dimensional sheets or chain-like structures which are made up of the spheres has been observed [81, 93].

In near critical colloid polymer mixtures the critical point is shifted to higher concentrations when shear flow is applied [66]. In the case of already phase separated mixtures shear flow can either deform structures or induce their formation. For example Derks et al studied phase separation under shear in a mixture of poly-(methylmethacrylate) PMMA particles and polystyrene spheres. They showed that above a critical size spinodal domains begin to couple to shear flow and are stretched in the direction perpendicular to flow and that the steady state width of the band-like structures is independent of the shear rate [22]. Similar string-like structures under shear are also observed in polymer blends [79].

In the case of colloid/polymer mixtures the complexity of the problem can be increased further by substituting the flexible polymer chains with more rigid rod-like particles [46]. The rods are much more susceptible to shear flow and it is thus reasonable to conclude that the coupling of the rods to the flow field will alter the rod-induced depletion force that is mediated between the spherical particles. This in turn will influence the stability of the rod/sphere mixtures. It is challenging to synthesize mono-disperse ideal colloidal rod model systems which are also neutrally bouyant. There are currently no systematic studies to our knowledge on mixtures of colloidal rods and spheres under shear flow as a result of this lack of suitable rods. Naturally occurring filamentous bacteriophages offer an excellent model for colloidal rod-like particles [34]. In particular *fd* virus is a well established model system (see section 3.2). Chapters 3 and 4 of this thesis have been dedicated to studying the equilibrium phase behavior of a mixture *fd* and polystyrene spheres that are density matched. In the rest of this chapter we will present the results of a systematic study of how structures formed in phase separating mixtures undergo deformation when subjected to a steady shear flow. We probed the internal sructure of clusters formed at statepoints that lie just above the experimentally determined gas/liquid binodal which we expect to have a purely liquid-like internal structure. We also investigate the internal structure of clusters that we observe in mixtures prepared at statepoints well above the gas/liquid binodal. For these statepoints we have evidence from confocal microscopy images which show clusters that have a highly ordered core and a disordered liquid-like outer layer.

In section 5.2 we describe the experimental details and the confocal-rheoscope which is a home built cone-plate shear cell mounted on a fast confocal fluorescence microscope that we use for performing in-situ rheology experiments. In section 5.3.1 we discuss the susceptibility to shear flow of the liquid droplets that are formed in the gas/liquid region of the phase diagram. We present in section 5.3.2 the results on the shear-induced deformation of clusters formed in the 3-phase coexistence region. We show in section 5.3.3 that the clusters in the 3-phase region before steady state deform via a mechanism similar to that of pure liquid droplets but at equilibrium they deform following a two step mechanism. This is followed by the conclusions in section 5.4.

5.2 Materials and experimental techniques

5.2.1 Description of model system

We used charge stabilized polystyrene spheres of diameter 0.5μm. The spheres were fluorescently labelled with rhodamine. To induce the depletion force between the colloidal spheres we used *fd* virus. *fd* is a filamentous bacteriophage 880nm long, 8nm in diameter with a persistence length of 2.2μm. A complete description of the colloidal particles and the buffer used for the experiments is given in section 3.2. *fd* virus which is made up of single stranded DNA wrapped in repeat units of coat proteins is also neutrally bouyant yielding a model system for which influence of gravitaty is negligible. We define the size ratio $\xi = L_{rod}/R_{sphere}$ where L_{rod} is the length of the rod and R_{sphere} is the radius of the polystyrene spheres which will be used for the rest of the chapter. The rod/sphere mixture that we discuss in the rest of the chapter has a size ratio of $\xi = 3.5$. We prepared mixtures with compositions in the two phase coexistence region (gas/liquid) and in the three phase (gas/liquid/solid) region of the phase diagram.

5.2.2 Cone/Plate shear geometry

For the shear experiments we used a home-built cone/plate shear cell which is mounted onto a ZEISS Axiovert 200M inverted microscope equipped with a vt infinity fast confocal unit. The cone is made of steel and has an angle of 1.4°. The bottom plate of the shear cell is made up of a circular coverglass 80 mm in diameter and 170μm thick as shown in the schematic diagram of the setup shown in figure 5.1. The actual inner diameter of the shear cell chamber is 20mm. Both the steel cone and glass bottom plate are coupled to servomotors that are driven independently and which are set to rotate in opposite directions. Figure 5.2 shows an engineering drawing with greater detail on the actual shear cell construction.

The rotation of the cone in an opposite direction to that of the plate results

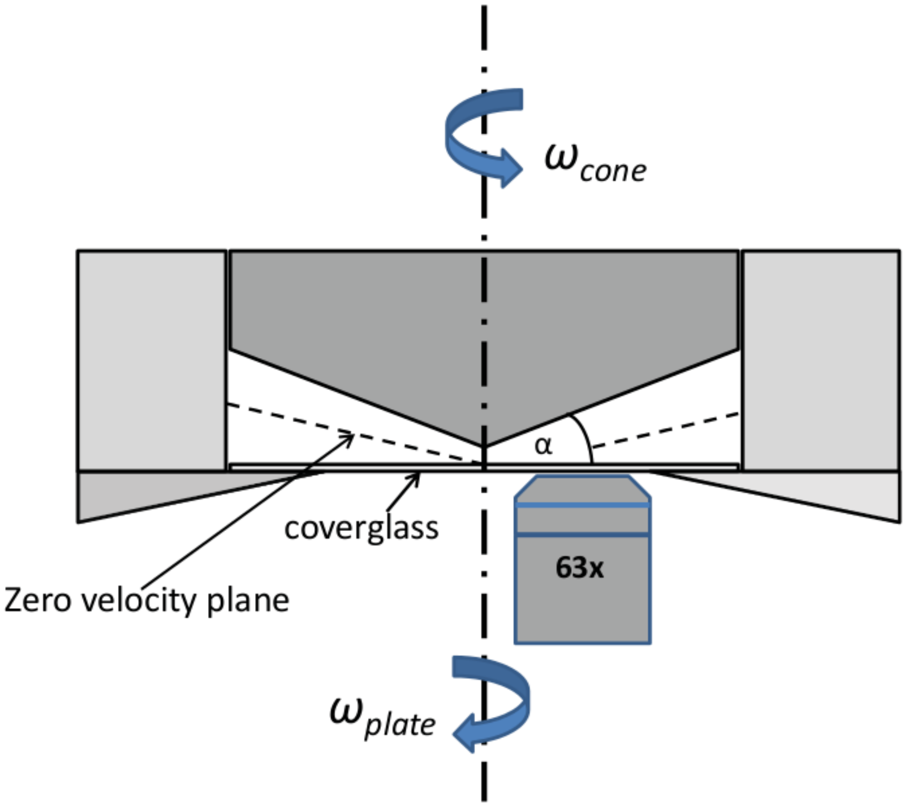

Figure 5.1: *Schematic diagram of the counter-rotating cone-plate shear cell.* $\alpha = 1.4°$ *is the angle the steel cone makes with the bottom glass plate. The location of the zero velocity plane is depicted by the dashed line.* ω_{cone} *and* ω_{plate} *are the angular velocities of the cone and plate respectively, which are made to rotate in opposite directions. The ratio of* $\omega_{cone}/\omega_{plate}$ *determines the location if the zero velocity plane.*

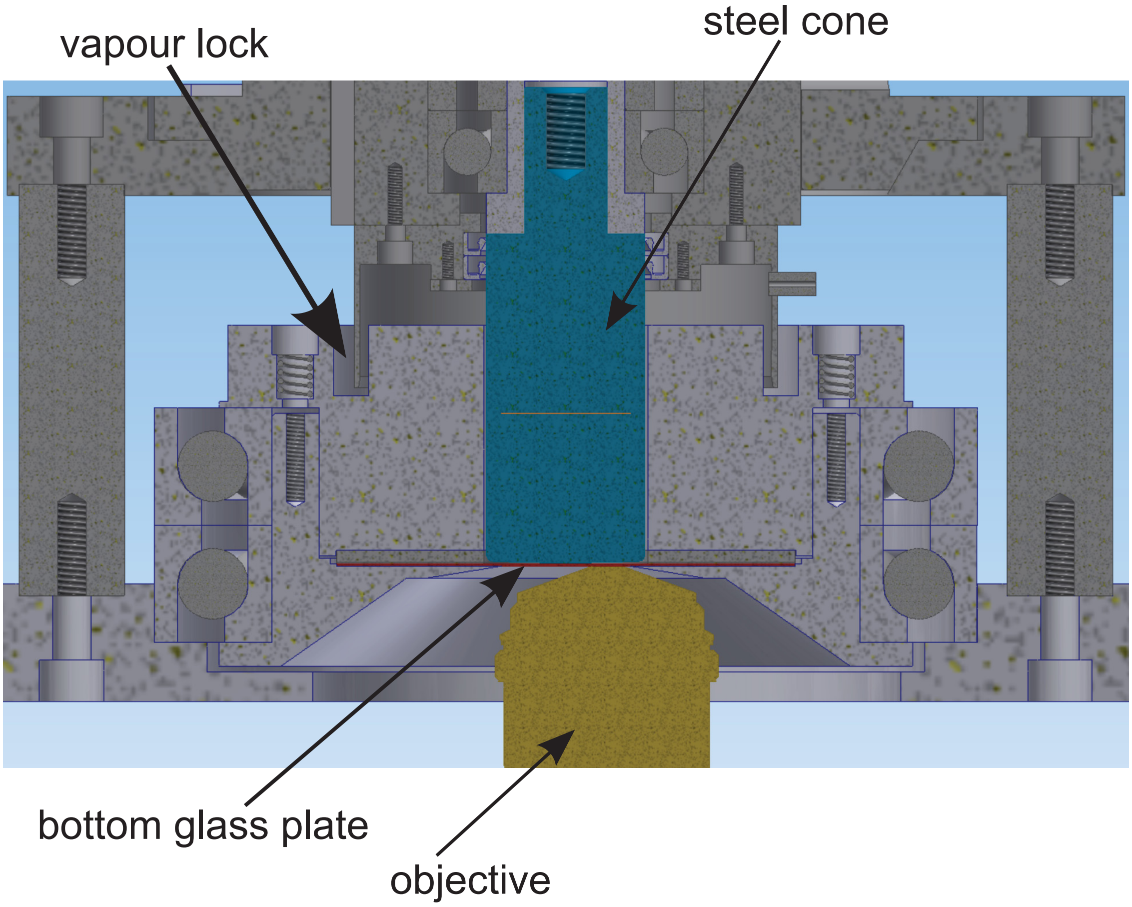

Figure 5.2: *A sectional view of the cone plate shear shell which is integrated onto an inverted confocal microscope. The shear cell is mounted onto the microscope such that the objective is 7 mm off the centre with respect to the centre of the shear cell. High magnification immersion objectives can be used for imaging by applying a thin film of immersion liquid onto the bottom glass plate in a ring which is concentric with the metal cone. Sample volume needed to fill the cell is 180 µl. The shear cell chamber is enclosed in a metal block and added to that a vapour lock reduces evaporation allowing experiments to be carried out over several hours with sample drying out.*

in the establishing of a stationary plane called the zero velocity plane. When observed under a microscope the structures that are located within this plane seem not move with repect to the lab frame of reference while shear is being applied. This makes it possible to observe what is in the zero velocity plane using the microscope without features of interest moving fast in and out of the field of view. The height of zero velocity plane is determined by the ratio of the angular velocity of the cone ω_{cone} to that of the bottom plate ω_{plate} while keeping the shear rate $\dot{\gamma}$ constant. For a cone/plate geometry, the shear rate is calculated using equation 5.1

$$\dot{\gamma} = \frac{\Delta\omega}{tan\alpha} \tag{5.1}$$

where $\Delta\omega = \omega_{cone} - \omega_{plate}$ and α is the angle between cone and bottom plate. From equation 5.1 it is clear that in the cone/plate geometry the shear rate is the same at all radial positions.

5.2.3 Image acquisition and analysis

Real time/space observations of the phase separated mixtures while subjecting the dispersions to shear flow is made by using the confocoal microscope in the EPI-fluorescence illumination mode. Relatively high frame rates $\sim 13fps$ are achieved by using a multi-pinhole fast confocal scanning unit. The confocal microsope is equipped with an Andor iXon camera (Andor Technologies) which has 512x512 pixels each of size 16μm x 16μm. For all the experiments discussed in this chapter we used a 63x Glycerol/Oil immersion objective with a Numerical Aperture N.A = 1.3 resulting in a field of observation of size 130μm x 130μm. The imaging plane was set parallel to the plane spanned by the velocity (v) and vorticity vector (∇ x v). The ratio of $\omega_{cone}/\omega_{plate}$ was chosen such that the zero velocity plane was $\sim 40\mu$m deep behind the bottom glass plate. Volume scans were obtained by driving the objective with a piezo crystal from Jena Piezo Systems which was sychronized with the fast confocal vt infinity confocal unit.

For example a hyperstack of 130μm x 130μm x 20 z-slices takes around 3s to acquire and at the relatively low shear rates used in the experimental protocol $\dot{\gamma} \leq 3s^{-1}$ the acquisition of the hyperstack is fast enough to avoid blurring of features that are in the field of view.

To characterize the deformation of clusters under shear we use an in-bulit function in ImageJ [92] which fits an ellipse of the projection of a cluster onto a 2D imaging plane. From the best fitting ellipse we obtain themajor and minor axes. We define the aspect ratio of the cluster as:

$$\beta = \frac{minor\, axis}{major\, axis} \tag{5.2}$$

The spherical polystyrene particles are highly scattering because they are not refractive index matched. This leads to poor resolution in the z-axis of the confocal volume scans. It is thus challenging to precisely determine the dimension of the clusters in the gradient direction. We performed 3D rendering of the volume scans using an in-built ImageJ plugin [92].

5.2.4 Determining the viscosity ratio of coexisting fluid/fluid phases and the capillary number Ca of liquid droplets

The viscosity ratio of coexisting fluid/fluid phases is a dimensionless parameter which is important in explaining the flow behavior of binary fluid mixtures. The viscosity ratio is defined as $p = \eta_d/\eta_h$, where η_d is the viscosity of the dispersed phase and η_h is the viscosity of the host phase. In our experiments clusters that are rich in spherical particles make up the dispersed phase while a rod-rich phase makes up the host. We now describe the experimental method which was used to determine the respective viscosities of the dispersed and host phase.

We determined η_h by measuring flow curves of pure *fd* which were suspended in the same buffer as the colloidal rod/sphere mixtures that were used for the shear experiments. Figure 5.3 shows a typical flow curve of pure *fd*. The dispersion of rods is shear thinning but the measured viscosity decreases only from

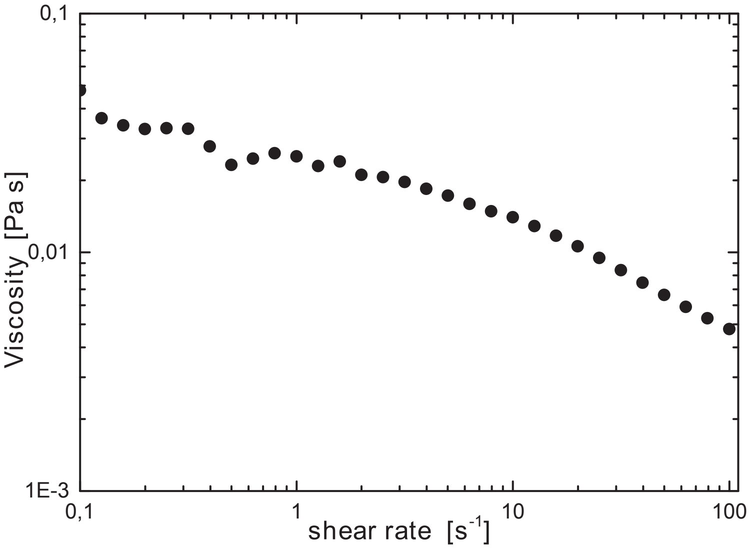

Figure 5.3: *Measured flow curve of a pure fd dispersion at a mass concentration of 2.5 mg/ml in a 10mM TRIS-HCl, 20mM NaCl buffer.*

0.034 Pa·s to 0.020 Pa·s in the shear rate regime ($0.03s^{-1} \leq \dot{\gamma} \leq 3s^{-1}$) in which the experiments were performed. We can thus approximate the rod-rich continuous phase in which the cluster are suspended as a Newtonian fluid and use the measured viscosity at low shear rates as the zero shear viscosity for calculating the viscosity ratio p. The viscosity of the clusters (rich in spherical particles) was determined by using an emperical expression for calculating the viscosity of a suspension of spheres given by equation 5.3

$$\eta_{drop} = \eta_h \left[1 - \frac{\phi_s}{\phi_{max}}\right]^{2.5\phi_{max}}, \tag{5.3}$$

where $\phi_{max} = 0.74$ and ϕ_s was obtained by determining the voxels occupied by the clusters in the confocal volume scans using a method described in section 4.3.1. We calculated a volume fraction of spheres ~ 0.3. This value of ϕ_s was then used to calculate the viscosity of the dispersed phase η_d. In the gas/liquid coexistence mixtutes that we sheared the viscosity ratio $p \approx 0.3$.

The capillary number Ca is a dimensionless number used to predict the deformation of liquid droplets which are suspended in a host phase of a higher viscosity. The theoretical background of Ca was introduced in chapter 2.6 and here we recall the main points. The capillary number Ca is defined as

$$Ca = \frac{\eta_h \dot{\gamma} R}{\Gamma} \tag{5.4}$$

where R is the radius of the spherical droplet and Γ is the interfacial tension between liquid droplet and surrounding gas phase. Ca is the ratio of viscous forces to the interfacial forces. In the case of Newtonian liquids the critical capillary number Ca_{crit} is obtained when the two respective forces are of the same order of magnitude. At $Ca < Ca_{crit}$ the interfacial tension is more dominant than the viscous forces and droplets deform affinely maintaining a stable ellipsoidal shape with increase in shear rates. At $Ca > Ca_{crit}$ the viscous forces dominate and droplets become unstable and begin to breakup. In the limit $Ca \gg Ca_{crit}$ droplets deform into long and slender bands that breakup due to Rayleigh-Taylor instabilities [95, 103]. For the calculation of Ca using equation 5.4, we used an average $< R >$ which was obtained from the confocal microscopy images of the sheared clusters ($< R > \sim 5 \cdot 10^{-6} m$) and Γ which was determined experimentally by capillary wave analysis as described in section 4.3.2 ($\Gamma \sim 10^{-8}$ N/m).

5.3 Results and Discussion

5.3.1 Shearing a gas/liquid coexistence mixture

In chapter 4 we determined the location of the two phase (gas/liquid) coexistence region in the rod/sphere mixture at relatively low sphere volume fraction $\phi_s < 0.1$ for a mixture of size ratio $\xi = 3.5$. The liquid phase is rich in the spherical colloids. We observed the formation of spherically shaped clusters which coexist together with a gas phase (poor in polystyrene spheres) which is suspended in a rod-rich host phase (see figure 5.6(A)). We also showed that the polystyrene spheres are neutrally bouyant and as such the suspended clusters made up of the spherical particles do not sediment but rather remain dispersed. Growth kinetics studies showed that the clusters grow until they reach an equilibrium end size after $\sim$ 60 minutes. The liquid-like droplets have an ultralow interfacial tension $\sim 10^{-8}$ N/m as determined by contour analysis of the thermally induced fluctuations at the gas/liquid interface. In this section we present the results of how single clusters which behave as liquid-like droplets of ultra-low interfacial tension γ that are suspended in a continuous matrix of different viscosity deform and finally breakup into daughter droplets. We compare the observed non-equilibrium droplet behavior to classical theories on droplet deformation and break-up [108].

We prepared a rod/sphere mixture at $\xi = 3.5$ which had a sphere/rod composition of $\phi_s = 0.03$ and $\phi_r = 0.007$ respectively. After preparing the mixture in an eppendorf tube we immediately loaded it into the home built counter-rotating shear cell described in section 5.2. We waited for an hour before starting the shear experiments to allow sufficient time for the system to fully phase separate and reach steady state. The statepoint labelled by the roman numeral (v) which we sheared is located just above the gas/liquid binodal line in the phase diagram presented in chapter 4.3 in figure 4.5. The end stage of the phase separation is made up of the liquid-like clusters which are suspended in a rod-rich host phase (figure 5.6(A)). The zero velocity plane was adjusted so that it was located $\sim 25\mu$m behind the cover glass. Confocal z-stacks were acquired by imaging a plane every 1 μm along the z-axis while simultaneously applying a ramp in shear rates. Time was allowed for the mixture to equilibrate after each step increase in shear rate $\dot{\gamma}$.

At $\dot{\gamma} \leq 0.05 s^{-1}$ the liquid droplets are not deformed as evidenced by an average value of the cluster aspect ratio $\beta \sim 1$ which was defined in equation 5.2. Table 5.1 is a summary of the results. At such low shear rates a snapshot of the dispersion under shear cannot be distinguished from images acquired in the quiescent state as shown in figure 5.6(A). After increasing the shear rate ($0.05 < \dot{\gamma} < 0.09 s^{-1}$) we observed that the droplets are deformed affinely into a steady ellipsoidal shape with an average cluster aspect ratio $\beta \sim 0.75$ which we obtained after analysing 10 clusters at each shear rate applied. The longest

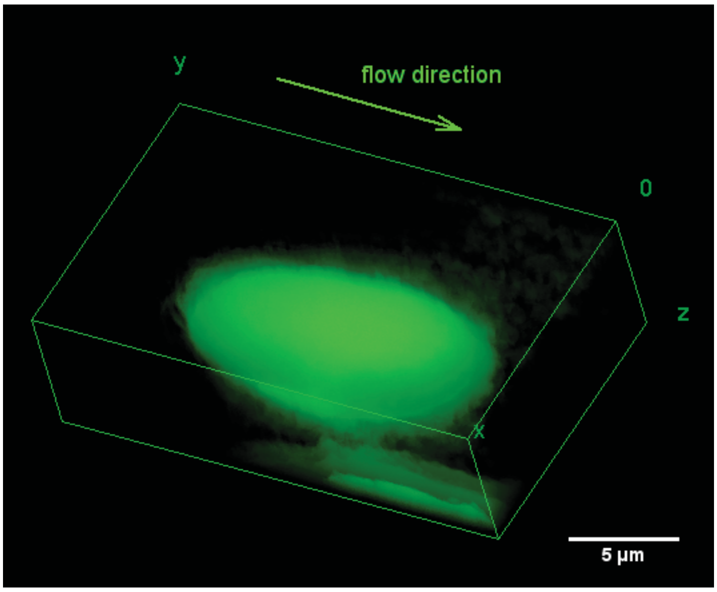

Figure 5.4: *A 3D rendering of a confocal z-stack showing a deformed liquid-like cluster at a shear rate* $\dot{\gamma} = 0.15$ *s* $^{-1}$. *The cluster is deformed into a steady ellipsoidal shape with the longest axis parallel to the flow direction.*

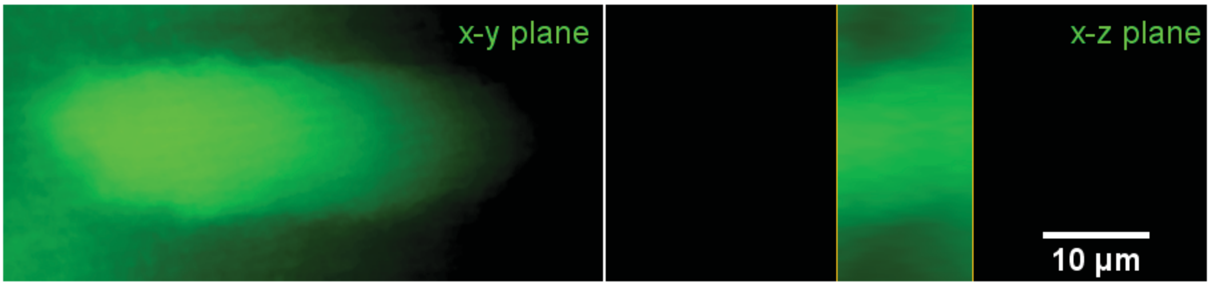

Figure 5.5: *Projections of the liquid-like cluster presented in figure 5.4 showing the equator of the cluster viewed in the plane spanned by the velocity and vorticity vector (left image) and the corresponding orthogonal view in the plane which is spanned by the gradient and vorticity vector (left image).*

axis of the droplet was alligned parallel to the direction of flow as shown in figure 5.6(B). Further increasing the shear rate ($0.09 < \dot{\gamma} < 0.15s^{-1}$) results in a state where the larger droplets are stretched into long and slender bands that almost stretch across the 128 μm long field of view used for the experiment while smaller droplets undergo affine deformation. A 3D reconstruction of an intermediate-sized droplet which is undergoing deformation is shown in figure 5.4. Sectional views of the ellipsoidal structure are shown in figure 5.5. At a constant $\dot{\gamma}$ the bandlike structures formed from the stretching of the larger droplets remain stable after allowing time for equilibration as presented in figure 5.6(C). On stopping the shear flow the band-like structures breakup into smaller droplets that retract back into spherical droplets as shown in the series of images in figure 5.6(D-F). Starting off at high shear rates $0.2s^{-1} < \dot{\gamma}$ results in the almost instantaneous formation of the bandlike structures similar to those presented in figure 5.6(C) which are unstable and are completely destroyed as strain units $\dot{\gamma}t$ increase.

Table 5.1: *Table showing droplet deformation mechanisms as shear rate $\dot{\gamma}$ is increased.*

Shear rate $\dot{\gamma}$ [s^{-1}]	Ca	<Cluster aspect ratio> (β)
≤ 0.05	≤ 0.25	~ 1
$0.05 - 0.09$	0.25 - 0.45	~ 0.75
$0.09 - 0.15$	0.5 - 0.8	decreases monotonically
> 0.2	> 0.8	not defined

To compare the experimentally observed droplet deformation with theoretical models and to discuss the subsequent breakup of clusters we will use the viscosity ratio p, the capillary number Ca and critical capillary number Ca_{crit} which were defined in section 5.2.4 and discussed more fully in section 2.6. In our experiment we obtained $p \approx 0.3$. We calculated Ca for the whole range of shear rates applied during the experimental protocol and the results are summarized in table 5.1. The table shows the observed droplet deformation at each respective shear rate. Grace [40] showed that for viscosity ratios p in the range $0.1 - 1.0$ the Ca_{crit} is ≈ 0.5. For our mixture we observed that the droplets

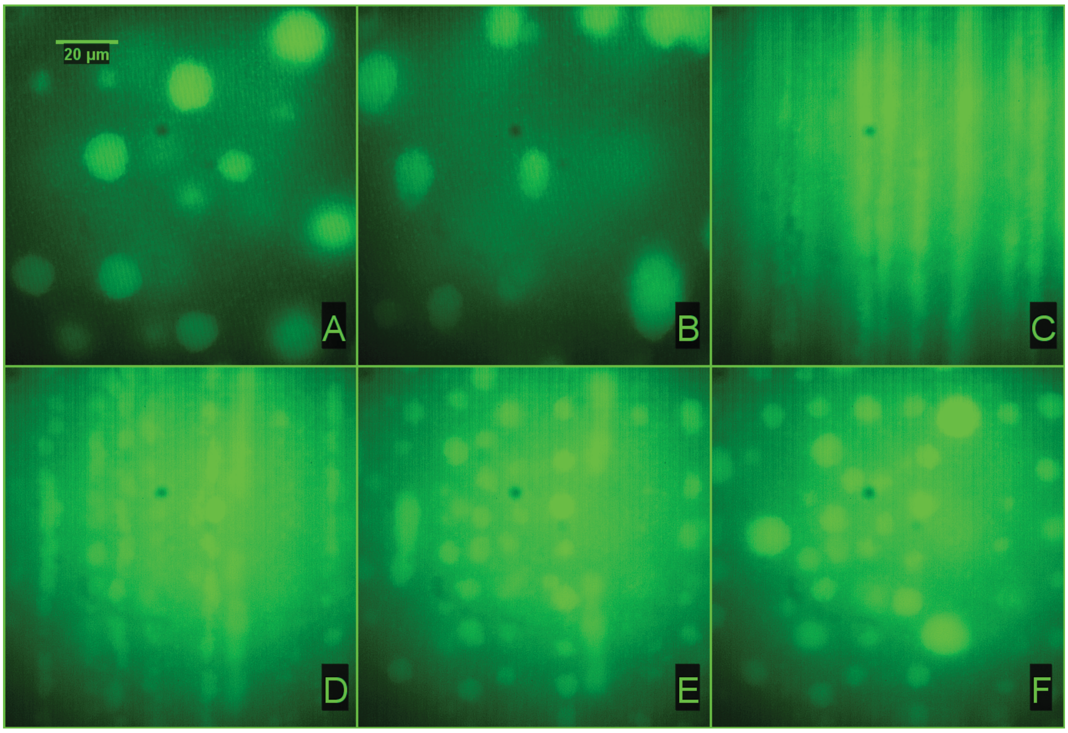

Figure 5.6: *Representative confocal microscopy images taken while applying a ramp in shear rates $\dot{\gamma}$. The rod/sphere mixture of size ratio $\xi = 3.5$ demixes into a gas and liquid phase that coexist. The liquid phase is in the form of suspended clusters rich in the spherical colloids and the gas phase of spheres is contained in the continuous rod-rich phase. The sphere volume fraction in the mixture is set to $\phi_s = 0.03$ and rod volume fraction $\phi_r = 0.007$. Shown are images acquired at shear rates $\dot{\gamma}$: 0.03 s^{-1} (A), 0.06 s^{-1} (B) and 1 s^{-1}(C). Images (D-F) are part of a time lapse showing what happens on cessation of the shear flow. The elongated bandlike structures break into smaller droplets that retract into spherically shaped ones.*

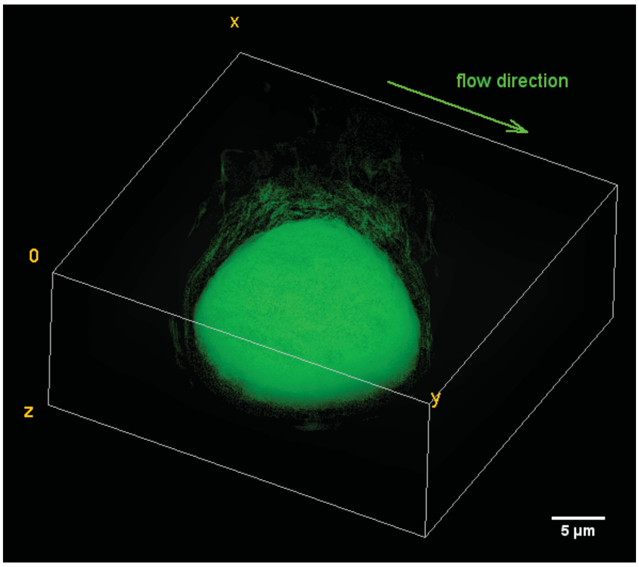

Figure 5.7: *A confocal volume image of a liquid-like cluster sitting at the glass wall under quiescent condition. The cluster partially wets the glass and maintains a finite contact angle with the cover glass.*

undergo affine deformation below $Ca \sim 0.5$ from a spherical shape into stable ellipsoids. At $Ca > 0.5$ the droplet shapes are not stable anymore. The droplets elongate into long slender band-like structures. This result is strikingly similar to the phenomenological behavior observed in mixtures of polymer blends [108]. The prediction of droplet deformation and break up under shear is often discussed using an emperically determined boundary which separates the region of stable droplets from unstable ones in a plot of capillary number Ca versus viscosity ratio p. This stability boundary spans an interfacial tension range of $5 \cdot 10^{-4} \leq \Gamma \leq 2.5 \cdot 10^{-2}$ N/m and covers several orders of magnitude of viscosities $5 \leq \eta \leq 3 \cdot 10^{3}$ Pa$\cdot$s [19, 40] (see figure 2.9 in chapter 2.6). It was determined for a model system of immiscible polymer blends. Our colloidal model system has a much lower interfacial tension ($\Gamma \sim 7 \cdot 10^{-7}$ N/m) and viscosity ($\eta \sim 0.025$Pa$\cdot$s) compared to what is typically the case in the polymer blends. Interestingly though, the stability boundary in figure 2.9 semi-quantitatively describes our observations.

A deviation from the predicted behavior using the stability boundary is observed at $Ca > 0.5$. Instead of droplets breaking up into smaller stable daugh-

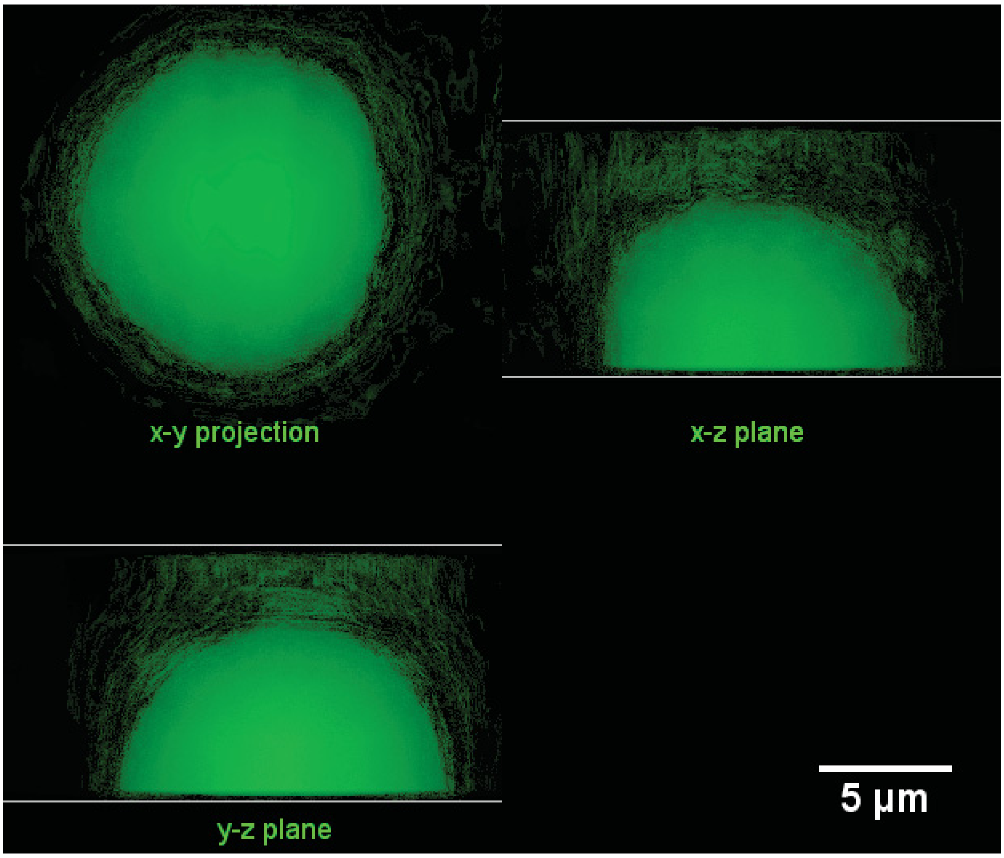

Figure 5.8: Sectional projections of the cluster shown in figure 5.7 under quiescent conditions.

ter droplets, stable bandlike sructures are formed as shown in figure 5.6(C). Such bandlike formation has been observed in phase-separated solutions of polymers [47, 107]. Hashimoto et al [47] call the band formation a string-like phase and suggest that the strings are the first step towards shear-induced mixing. Qualitatively we observe the same behavior. At moderate shear rates the string-like phase is stable but at higher shear rates the cross section of bands decreases until the bands are destroyed. The fact that at moderate shear rates the bandlike structures are stable can be attributed to the suppression of surface tension instablities by shear flow [21, 47]. The coupling of the shear flow to the capillary waves leads to an effective interfacial tension which is dependent on the shear rate (section 2.5). By suppresing the thermally induced fluctuations at the fluid/fluid interface, the Rayleigh-Taylor instabilities that would typically lead to break up of the bands are damped and thereby stabilizing the band-like structures. Droplet breakup and retraction is observed on cessation of shear as shown in figure 5.6(D-F) which can be understood by considering that the interfacial tension becomes dominant in the absence of viscous stresses of the sheared host.

The experimental evidence gathered from studying the behavior of the clusters under shear in this section clearly shows that the clusters behave as purely liquid droplets. Further evidence of the liquid-like nature of the clusters is the way that clusters which are close to the bottom glass plate of the shear cell partially wet the glass surface forming a finite contact angle. Figure 5.7 is an example of a cluster at the bottom glass plate of shear cell. Orthogonal projections of the cluster are shown in figure 5.8 clearly highlighting the finite contact angle between the horizontal glass plate and droplet surface. In the next section we will probe mixtures in the region where we observed the coexistence of three phases (gas/liquid/solid) using shear flow.

5.3.2 Shearing clusters in the 3-Phase region

In section 4.3.4 we presented confocal microscopy images of clusters rich in polystyrene spheres which are formed after phase separation in a rod/sphere

Table 5.2: *Table showing shear rate at which tip streaming occurs ($\dot{\gamma}_s$) in a mixture at fixed $\phi_s = 0.01$ but increasing rod volume fraction ϕ_r.*

ϕ_r	$\dot{\gamma}_s$ in s^{-1}
0.010	2.5
0.013	6.8
0.015	9.2

mixture at a size ratios $\xi = 3.5$. The clusters formed in that part of the phase diagram have a core in which the polystyrene particles are highly ordered and an outer which shows a liquid-like ordering. Dispersed clusters coexist together with a dilute gas phase. We conclude from this experimental evidence that we have identified a 3 phase coexistence region in our phase diagram. Such a 3-phase region is predicted for rod/sphere mixtures using the The FVT at size ratio $\xi > 0.6$. The 3 phase region is bounded from below by a gas/liquid two-phase region and bounded above by the gas/solid coexistence region [63]. In the rest of this section we will present the results of the response of the clusters found in this 3 phase region to simple shear flow. We then compare the deformation pathway of the clusters to that of the one observed in the case of purely liquid-like clusters which were discussed in section 5.3.1.

Rod/sphere mixtures at a size ratio $\xi = 3.5$ were all prepared in a density matched buffer as described in section 5.2. The sphere volume fraction was fixed at $\phi_s = 0.01$ but we varied the rod volume fraction ϕ_r. After preparing a mixture of a desired composition, we loaded the sample into our home built cone/plate shear cell and waited for an hour before performing shear experiments to allow the system to reach equilibrium. We set the zero velocity plane at 30 μm behind the cover glass. For all the experiments which are reported in this section the experiment consisted of a ramp in shear rates ($\dot{\gamma} < 10s^{-1}$) while acquiring a time series of images in the zero velocity plane at an average rate of 13 frames per second.

We can describe the observed response of the clusters to the ramp in shear rates ($\dot{\gamma}$) by defining three main flow regimes. In the first regime at $\dot{\gamma} < 0.4s^{-1}$ no

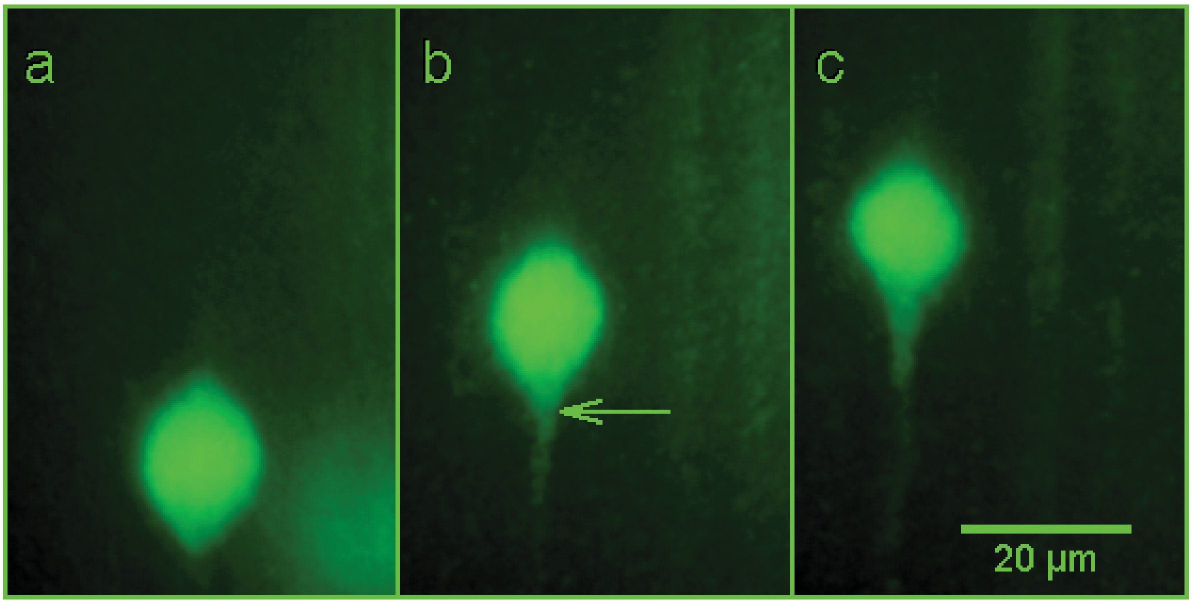

Figure 5.9: *The evolution from a stable cluster under shear (a) to one undergoing tip streaming (b) and (c). The green arrow in (b) shows the region at one of the poles of the cluster where a thin liquid jet is released in the direction of the flow field.*

deformation was observed. Increasing the shear rate to $0.4s^{-1} < \dot{\gamma} < 2.5s^{-1}$ we enter into an intermediate regime where clusters grow into larger structures by means of coalescence which is aided by the shear-induced convection but there is no indication of clusters undergoing deformation. The average cluster shape due to the coalescence events is no longer spherical but relatively anisotropic which we parameterize by defining a major and minor axes. In the intermediate regime the major axis of the clusters tumbles with respect to the direction of flow. Since we only observe a projection of the clusters onto the imaging plane and thus do not have information in the z direction, we could not precisely determine the tumbling frequency. In the third flow regime the clusters are deformed as shear rate is increased. In particular spherically shaped clusters deform into a spindle-like shape with the pointed tips pointing in the direction of shear flow (see figure 5.9(a)). This is followed by an ejection of a thin stream of particles emanating from the tips of the clusters as shown in figure 5.9(b). Keeping the shear rate constant leads to tip-streaming which is followed by a complete melting of the clusters into band-like structures made up of the spherical particles similar to the bands observed for the liquid droplets mentioned in section 5.3.1. The shear rate at which this jetting and susbsequent melting away of clusters occurs increases with the increase in rod volume fraction ϕ_r for a fixed sphere volume fraction ϕ_s as shown in table 5.2.

The transition from the first flow regime where the clusters maintain a fixed orientation with respect to the flow direction, into the second flow regime in which the clusters start to tumble is observed in many model systems. Examples include suspensions of lipid vesicles [58, 75] and red blood cells [59]. Differences in the detailed rheological response is governed by the interfacial tension, the strength of the interparticle attraction and the viscosity ratio p. In the first two flow regimes presented in the preceeding paragraph the clusters behave as undeformable anisotropically shaped colloidal structures under shear. The third flow regime which occurs at larger shear rates has many similarities to a phenomenon called tip-streaming. The classical case of tip streaming applies to purely liquid droplets where the droplets become elongated during shear thereby forming pointed tips. The tip formation is followed by an ejection of smaller droplets at the pointed tips until a new equilibrium droplet size and shape is achieved for the specific shear rate being applied [87]. The difference to what we obeserve from this classical picture is that we do not obtain discrete droplets being ejected at the tips but rather we obtain a thin tube-like liquid jet at the conical shaped tips (see figure 5.9). Furthermore instead of the streaming stopping after the larger cluster has reduced its size as in the classical case [102], we observe a complete fluidization of the once solid core into a band-like strip. We propose that what we observe for the clusters in the 3 phase region under shear is not the classical tip streaming but rather the gradual deformation and the subsequent melting away of the clusters.

In the initial stages of the cluster deformation the shear flow mainly affects the outer liquid-like layer by changing its effective dynamic interfacial tension Γ_{eff} (equation 2.40). Derks et al showed how shear flow suppresses the thermally-induced fluctuations at a colloidal gas/liquid interface which in turn leads to an increase in Γ_{eff} [21]. A more comprehensive description of the dynamic interfacial tension in colloid/polymer mixtures under shear was given in chapter 2.5. In the cone/plate geometry used in our shear experiments the coupling of shear flow to the capillary waves is highly effective for the surfaces of clusters which mostly lie in the direction parallel to the flow resulting in a localized increase in the effective surface tension $\Gamma_{eff}^{\|}$. The interfacial tension for the surfaces which lie perpendicular to the flow direction $\Gamma_{eff}^{\perp}$ is much lower than the $\Gamma_{eff}^{\|}$ and this difference in magnitude increases at higher shear rates (figure 2.8). This anisotropy in the dynamic surface tension results in the formation of conical shaped tips at the poles of the clusters (see figure 5.9). Such tip formation was not observed for the purely liquid droplets in the previous section 5.3.1 because in that case shear rates that are by a factor 10 less than the ones applied in this section were sufficient to deform and destroy the clusters. The surface tension can be approximated as isotropic throughout the cluster surface at the low shear rates applied in the respective experimental protocol. The next stage of the deformation is the steady jetting of the outer liquid layer which starts from these pointed tips. As the liquid layer decreases in thickness the inner solid-like core is then gradually fluidized. In the final stages the cluster is smeared into long and slender liquid-like bands.

The shear rate at which the "*3 phase clusters*" start to deform increases at a fixed sphere volume fraction ϕ_s with increase in rod volume fraction ϕ_r. We can explain this by considering that the depletion-induced attraction acting between the spherical particles also increases with ϕ_r. This increase in interparticle attraction is further confirmed by the capillary wave analysis at the gas/liquid interface which showed that the amplitude of the fluctuation of the interface decreases with increase in ϕ_r (see section 4.3.4) which implies a larger interfacial tension.

5.3.3 Crystal nucleation inside dense liquid droplets

In the previous subsection 5.3.2 we characterized the flow behavior of clusters which are formed in the 3 phase coexistence region of our rod/sphere mixture at a size ratio $\xi = 3.5$. In this section we present the results of a shear experiment that we designed to study the evolution of the internal structure of clusters. ten Wolde et al have shown using numerical simulations that in the phase diagram of colloids which have relatively short-range attractions, crystalline nuclei can form within an initially dense liquid-like cluster [117]. The formation of the crystallite at the core is attributed to critical density fluctuations within the pure dense droplet twhich lower the free energy needed to form the crystal nucleus. The probability of the crystallite nuclei formation increases above a critical size of the liquid-like droplet [117].

In the early stages of phase separation the core of clusters shows no crystalline ordering based on the analysis of confocal microscopy cluster images. A solid-like core is resolved when the average size of the clusters approaches a steady state end size which we determined experimentally (section 4.3.1 where the growth kinetics of clusters is discussed). The fact that the highly ordered structure inside the clusters starts appearing in the microscopy images only at later times leads us to conclude that initially the core is just a dense fluid which then transforms into a crystalline ordered phase in line with ten Wolde et al [117] numerical simulation results. We probed the internal structure of the clusters by subjecting them to shear flow at different waiting times after quenching. In each experiment we determined the shear rate at which the onset of cluster deformation occurred and the corresponding droplet deformation mechanism.

In the shear experiments performed at relatively short waiting times after quenching $t \leq 50$ minutes, low shear rates (corresponding to a low shear stress) were sufficient to destroy the clusters ($\dot{\gamma} < 6s^{-1}$) as shown in figure 5.10. For longer waiting times after quenching $t > 50$ minutes much higher shear rates ($\dot{\gamma} > 6s^{-1}$) were needed for destroying clusters as also shown in the figure 5.10. From our study of the growth kinetics of a mixture of the same composition

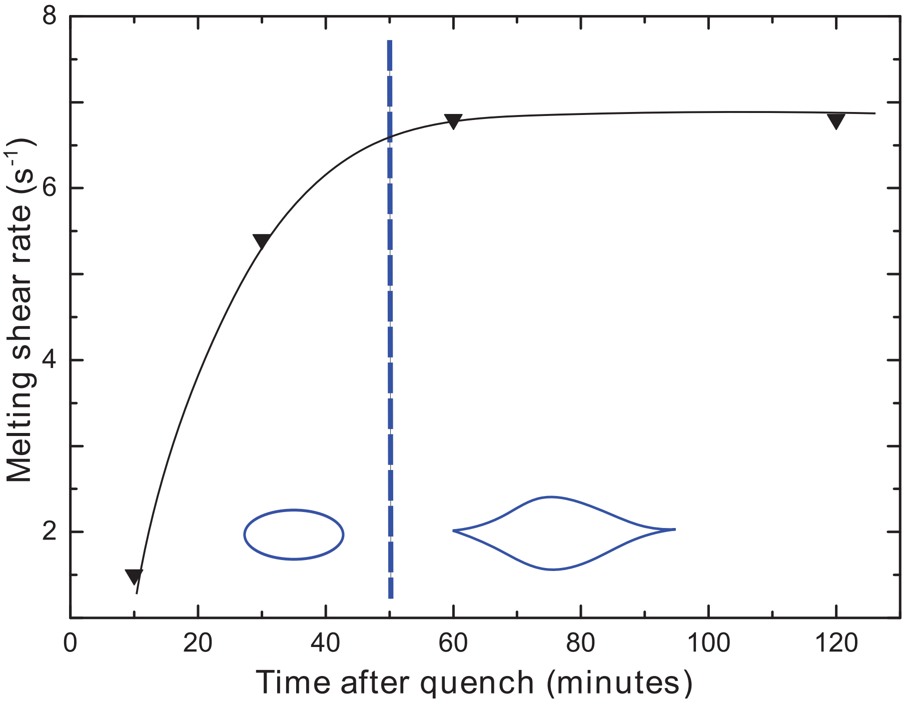

Figure 5.10: *A plot showing the shear rate at which clusters are deformed and thereafter destroyed. Each solid triangle is a separate experiment for which a mixture of a fixed composition* ($\phi_r = 0.013, \phi_s = 0.01$) *is prepared but sheared at different waiting times after sample preparation. The blue vertical dashed line separates the observed droplet deformation mechanisms into two main flow regimes. For mixtures sheared after waiting* $t \leq 50$*minutes the clusters are affinely deformed into ellipsoidal shaped droplets as illustrated by the blue ellipse inserted into the figure to the left of the dashed line. For mixtures sheared after* $t > 50$*minutes the clusters deform via the formation of cone shaped tips (illustrated by sketch to the right of the blue dashed line) which is followed by the ejection of a stream of particles similar to what was presented to figure 5.9.*

under quiescent conditions (see section 4.3.1) we know that after ≈ 60 minutes the clusters reach an equilibrium end size which has a narrow size distribution. The results presented in figure 5.10 and the knowledge of the growth curve of the clusters suggests that clusters in mixtures which are allowed to fully phase separate have a greater shear modulus than that of the ones formed during the initial stages of the phase separation. It was also observed that the clusters at relatively short waiting times after quenching $t \leq 50$ minutes, deform via a different mechanism compared to clusters in samples allowed to phase separate for longer times $t > 50$ minutes as shown in figure 5.10. At shorter waiting times the droplets deform affinely into ellipsoidal shaped structures which is a typical deformation mechanism of purely liquid droplets dispersed in a continuous phase of a different viscosity. For mixtures allowed to phase separate for longer times we observed the tip streaming-like phenomena which we attribute to the cluster having a denser solid-like core and a liquid-like outer layer. From this experimental evidence we conclude that the internal structure of the clusters seems to evolve from a purely liquid homogeneous droplet to one with a much more dense core. The core shows a crystalline ordering as observed by means of confocal microscopy images (see section 4.3.4).

5.4 Conclusion

Simple shear flow was used to probe the structure of clusters which are formed in phase separating colloidal rod/sphere mixtures. Clusters that are formed in the two phase (gas/liquid) coexistence region of the phase diagram responded to shear via a mechanism similar to what is observed for purely liquid droplets that are suspended in a host medium of a higher viscosity. Several flow regimes were identified. No deformation of structures was observed at the lowest shear rates ($\dot{\gamma} \leq 0.05 s^{-1}$) applied in a shear ramp experiment. Increasing the shear rate ($0.05 < \dot{\gamma} < 0.09 s^{-1}$) led to the clusters being deformed affinely into stable ellipsoidal shaped droplets with the longest axis aligned parallel to the direction of flow. Increasing the shear rate further ($0.09 < \dot{\gamma} < 0.15 s^{-1}$) resulted in a coexistence of smaller sized clusters that deform affinely and stable band-like structures which are formed as a result of the streching of the larger sized droplets. The bands break-up into smaller droplets when shear flow was switched off reminescent of Rayleigh-Taylor instabilities. The remixing of phase separated mixtures occurred in experiments where the shear protocol started off with the application of relatively high shear rates ($0.2s^{-1} < \dot{\gamma}$). The behavior of the clusters under shear flow clearly shows that their internal structure is made up of a purely liquid-like phase. The partial wetting of the bottom glass wall of the shear cell by the cluster provides corroborative evidence that the clusters formed in state-points close to the gas/liquid binodal are indeed liquid-like droplets. Due to the fact that we study the phase behavior of the rod/sphere mixture at rather low sphere volume fractions ($\phi_s < 0.06$) the number density of spherical particles is not significantly high enough to form a single homogeneous liquid phase. We instead obtain spherical shaped droplets dispersed throughout the rod-rich host medium.

There is a clear difference in the evolution of cluster shapes as the rate of shearing is increased in the case of the 3 phase region (see figure 5.9) to that of the purely liquid-like droplets (see figure 5.6) found in the 2 phase region of the phase diagram. This difference is a strong indication that the "*3 phase clusters*" are much more viscous at the core than the purely liquid ones. Futher proof that the "*3 phase clusters*" have a solid-like core is seen in the shear rates at which deformation is observed. The "*2 phase clusters*" require shear rates as low as $\dot{\gamma} \approx 0.1s^{-1}$ to destroy the clusters, but for the more solid-like clusters the shear rates must be increased by up to a factor 10 to begin to observe small deformations. In the low shear rate regime the 3-phase clusters behaved as purely solid structures under shear showing a transition from a fixed orientation with respect to velocity vector to a tumbling behavior. Our experiments revealed that cluster deformation followed a two step pathway. In the first step of the cluster deformation we observe a jet streaming of particles from conical shaped tips. We propose that the tips form as a result of a lower effective interfacial tension Γ_{eff}

at the poles than on the cluster surfaces which are parallel to the flow direction. The interfacial tension of surfaces parallel to flow direction is lower because shear induces suppression of capillary waves leading to an increase in Γ_{eff}. After the outer liquid layer is convected away we enter into the second step of the deformation pathway. In this step the crystalline core is melted and we observe the formation of bands similar to the ones we obtain in the case of the 2-phase liqiuid-like clusters. We conclude that the deformaton of the 3-phase clusters begins with the shear flow affecting mainly the outer liquid-like layer and once that fluid layer is depleted the solid-like core is then fluidized and subsequently smeared into the band-like structures. Further shearing after band formation as in the 2-phase clusters case leads to mixing.

We also showed that the internal structure of the 3-phase clusters evolves from a purely dense liquid-like state at short waiting times after preparing mixture to a crystalline structure inside the cluster having a melted liquid-like outer layer when system is fully phase separated. We propose that this is an experimental observation of crystal nucleation inside a dense fluid cluster which is induced by critical density fluctuations as predicted by ten Wolde using numerical simulations [105].

6

Summary and Outlook

The central theme of this thesis is the study of the stability of a model colloidal rod/sphere mixture under equilibrium conditions and the role that an external flow field plays on the phase behavior of the mixture. Experimentally obtained phase boundaries are related to binodals which are calculated using the Free Volume Theory (FVT), a well established method for calculating phase boundaries in mixtures of colloids. For state-points which de-mix, the resulting microphases are sheared in order to probe the internal structure. The subsequent deformation pathways are compared with semi-quantitative models. In this thesis we use mixtures of rods and neutrally buoyant polystyrene spheres with size ratios ξ in the range 1.8 to 3.5. Here ξ is defined as the ratio of L_{rod}/R_c where L_{rod} is the length of the colloidal rods and R_c is the radius of the spheres. The rods induce an attractive interaction potential between the spherical particles. *fd* virus, a micron-sized semi-flexible filamentous bacteriophage was used as a model for an ideal rod-like colloid.

In chapter 3 we characterized the depletion-induced clustering in the mixtures at various ξ using a combination of light scattering and optical microscopy techniques. We investigated the influence of the size ratio ξ and the effective buffer ionic strength on the location of the gas/liquid binodal in the equilibrium state diagram. We found that the gas/liquid binodal line shifts to higher rod volume fractions ϕ_r with increase in ξ. The binodals which were calculated using the FVT are in good qualitative agreement with the experimental results. We find however a quantitative mismatch between theory and experiments which increases in magnitude with increasing ξ. This discrepancy can be explained by the fact that the mathematical expression used to calculate the average free volume of rods in the phase boundary calculation scheme is correct in the limit of low ϕ_r and is only an approximation at higher ϕ_r. At larger ξ much higher rod volume fractions are required to induce phase separation and in turn the FVT is less accurate.

In chapter 4 we performed capillary wave analysis at the interfaces between a coexisting liquid and gas phase. We obtained an ultra-low interfacial tension γ ranging from 10^{-7} to 10^{-9} N/m. The values obtained are comparable to those calculated using scaling laws. We characterized the region of the state diagram located just above the experimentally determined gas/liquid binodal for a mixture at a size ratio $\xi = 3.5$. Three distinct regions were identified which the FVT also predicts. In the first region we found liquid-like clusters (rich in polystyrene spheres) coexisting together with a gas phase. In the second region the core of the clusters exhibits a crystalline structure, but a more liquid-like outer layer which coexists with a gas phase. In the third region we find the coexistence of crystallites and a gas phase.

In chapter 5 the internal structure of the clusters was probed using a counter-rotating cone/plate shear cell, mounted on a confocal microscope, which facilitated measurements in real space/time while simultaneously applying shear. We found that clusters which are formed in the two phase (gas/liquid) coexistence region, responded to shear via a pathway similar to that of droplets which are suspended in a denser fluid. At intermediate shear rates stable bands were bands were formed. We rationalized that the stability is due to the shear dependent suppression of capillary waves on the surfaces of the bands which leads to an increase in the interfacial tension. On cessation of shear the bands break up into daughter droplets reminiscent of the Rayleigh-Taylor instabilities. Phase separated mixtures are homogenized above a limiting shear rate. We also found that clusters in the (gas/liquid/solid) coexistence region deform following a two-step pathway. The first step involves the removal of the liquid-like outer layer via a jet streaming of particles from conical shaped tips which point in the direction of shear flow. The final step involves the fluidization of the crystalline core which leads to the formation of liquid-like bands similar to what was observed in the case of the liquid-like cluster. Finally we could show that the crystalline core belonging to clusters in the three phase region is a result of the formation of crystal nuclei within an initially dense fluid phase. This can be explained by critical density fluctuations which lower the free energy barrier for crystal nucleation within such a metastable fluid phase.

For further work on the characterization of the rod sphere mixture, several properties of the colloidal particles require improvement in order to allow the use of optical microscopy techniques. Firstly the synthesis of spherical particles that have a fluorescent core and an outer shell than can be rendered transparent by matching the shell's refractive index to that of the solvent. Such an improvement would facilitate the tracking of particles within clusters and also allow the direct determination of the particle ordering within the microphases. With respect to the rods, it would be of interest to use a more rigid rod. A possibility would be to use Y-21M, which is a mutant of the wild type *fd*. This mutant has a persistence length ~ 10 times its contour length and offers a good model for an ideal rod. One would expect a better agreement of the experimentally obtained binodals with those predicted by the FVT in mixtures of Y-21M and spheres. Another feature which was not exploited in our experiments is the possibility to fluorescently label the viruses. This feature would allow the direct visualization of the rod-rich phase at single particle level. In shear experiments, the average orientation of the rods could then be determined in real space/time as a function of shear rate.

Acknowledgments

Completing this Thesis has been indeed a challenging experience. As I got closer to the end of the formal part of my graduate studies, it became more intense and it demanded even more mental, emotional and physical resources.

The support that I received from family and friends is what made it possible in the end. Thanks to my wife Comfort, my mother Nyarai Simbanegavi, my boys Caleb and Jermaine. Your love, support and understanding I cherish very much.

I am grateful to my advisor and friend Prof. Dr. Pavlik Lettinga and to Prof. Dr. J.K.G Dhont for the opportunity to pursue my graduate training in his group. Special thanks goes to Prof. Dr. Stefan Egelhaaf for the insightful discussions. Last but not least all the members of the Institute of Complex Systems 3 at the Juelich Forschungszentrum and the IHRS BioSoft graduate school.

List of Figures

List of Tables

Bibliography

[1] D. Aarts. *The Interface In Demixed Colloid-Polymer Systems*. PhD thesis, Universiteit Utrecht, 2005.

[2] D. G. A. L. Aarts, R. P. A. Dullens, and H. N. W. Lekkerkerker. Interfacial dynamics in demixing systems with ultralow interfacial tension. *New Journal of Physics*, 7(1):40, 2005.

[3] D. G. A. L. Aarts, M. Schmidt, and H. N. W. Lekkerkerker. Direct visual observation of thermal capillary waves. *Science*, 304(5672):847–850, 2004.

[4] B. J. Ackerson and N. A. Clark. Shear-induced melting. *Physical Review Letters*, 46(2):123, 1981.

[5] B. J. Ackerson and P. Pusey. Shear-induced order in suspensions of hard spheres. *Physical review letters*, 61(8):1033, 1988.

[6] M. Adams, Z. Dogic, S. L. Keller, and S. Fraden. Entropically driven microphase transitions in mixtures of colloidal rods and spheres. *Nature*, 393:349, 1998.

[7] S. Asakura and F. Oosawa. On interaction between two bodies immersed in a solution of macromolecules. *The Journal of Chemical Physics*, 22(7):1255–1256, 1954.

[8] S. Asakura and F. Oosawa. Interaction between particles suspended in solutions of macromolecules. *Journal of Polymer Science*, 33(126):183–192, 1958.

[9] R. Bandyopadhyay and A. Sood. Effect of silica colloids on the rheology of viscoelastic gels formed by the surfactant cetyl trimethylammonium tosylate. *Journal of colloid and interface science*, 283(2):585–591, 2005.

[10] E. Barry and Z. Dogic. Entropy driven self-assembly of nonamphiphilic colloidal membranes. *Proceedings of the National Academy of Sciences*, 107(23):10348–10353, 2010.

[11] P. Bartlett, R. Ottewill, and P. Pusey. Superlattice formation in binary mixtures of hard-sphere colloids. *Physical review letters*, 68(25):3801, 1992.

[12] S. A. Berkowitz and L. A. Day. Mass, length, composition and structure of the filamentous bacterial virus fd. *Journal of Molecular Biology*, 102(3):531 – 547, 1976.

[13] T. Betz and C. Sykes. Time resolved membrane fluctuation spectroscopy. *Soft Matter*, 8:5317–5326, 2012.

[14] T. Biben and J.-P. Hansen. Phase separation of asymmetric binary hard-sphere fluids. *Physical review letters*, 66(17):2215–2218, 1991.

[15] P. Bolhuis and D. Frenkel. Numerical study of the phase diagram of a mixture of spherical and rodlike colloids. *The Journal of chemical physics*, 101:9869, 1994.

[16] S. BOLTE and F. P. CORDELIÃˆRES. A guided tour into subcellular colocalization analysis in light microscopy. *Journal of Microscopy*, 224(3):213–232, 2006.

[17] J. Buitenhuis, L. N. Donselaar, P. A. Buining, A. Stroobants, and H. N. Lekkerkerker. Phase separation of mixtures of colloidal boehmite rods

and flexible polymer. *Journal of colloid and interface science*, 175(1):46–56, 1995.

[18] E. H. de Hoog and H. N. Lekkerkerker. Measurement of the interfacial tension of a phase-separated colloid-polymer suspension. *The Journal of Physical Chemistry B*, 103(25):5274–5279, 1999.

[19] R. A. Debruijn. *Deformation and breakup of drops in simple shear flows*. PhD thesis, 1991.

[20] B. V. Derjaguin. Untersuchungen über die reibung und adhäsion, iv. *Colloid & Polymer Science*, 69(2):155–164, 1934.

[21] D. Derks, D. G. Aarts, D. Bonn, H. N. Lekkerkerker, and A. Imhof. Suppression of thermally excited capillary waves by shear flow. *Physical review letters*, 97(3):038301, 2006.

[22] D. Derks, D. G. A. L. Aarts, D. Bonn, and A. Imhof. Phase separating colloid polymer mixtures in shear flow. *Journal of Physics: Condensed Matter*, 20(40):404208, 2008.

[23] J. K. Dhont and W. Briels. Viscoelasticity of suspensions of long, rigid rods. *Colloids and Surfaces A: Physicochemical and Engineering Aspects*, 213(2):131–156, 2003.

[24] J. K. G. Dhont. *Dynamics: models and kinetic methods for non-equilibrium many body systems*. Kluwer Academic Publishers, 2000.

[25] Z. Dogic. *Liquid crystalline phase transitions in virus and virus/polymer suspensions*. PhD thesis, Brandeis University Department of Physics, 2000.

[26] Z. Dogic and S. Fraden. Ordered phases of filamentous viruses. *Current opinion in colloid & interface science*, 11(1):47–55, 2006.

[27] J.-L. Doublier, C. Garnier, D. Renard, and C. Sanchez. Protein–polysaccharide interactions. *Current Opinion in Colloid & Interface Science*, 5(3):202–214, 2000.

[28] S. E. Duwe H.P, KAES J. Bending elastic-moduli of lipid bilayers-modulation by solutes. *JOURNAL DE PHYSIQUE*, 51:945–962, 1990.

[29] R. J. Ellis and A. P. Minton. Cell biology: join the crowd. *Nature*, 425(6953):27–28, 2003.

[30] R. J. Ellis and A. P. Minton. Cell biology: join the crowd. *Nature*, 425(6953):27–28, 2003.

[31] C. Esposito, A. Tian, S. Melamed, C. Johnson, S.-Y. Tee, and T. Baumgart. Flicker spectroscopy of thermal lipid bilayer domain boundary fluctuations. *Biophysical Journal*, 93(9):3169 – 3181, 2007.

[32] J. Evans, W. Gratzer, N. Mohandas, K. Parker, and J. Sleep. Fluctuations of the red blood cell membrane: Relation to mechanical properties and lack of {ATP} dependence. *Biophysical Journal*, 94(10):4134 – 4144, 2008.

[33] Faucon, J.F., Mitov, M. D., Méléard, P., Bivas, I., and Bothorel, P. Bending elasticity and thermal fluctuations of lipid membranes. theoretical and experimental requirements. *J. Phys. France*, 50(170):2389–2414, 1989.

[34] S. Fraden. Phase transitions in colloidal suspensions of virus particles. 460:113–164, 1995.

[35] S. Fraden, G. Maret, D. Caspar, and R. B. Meyer. Isotropic-nematic phase transition and angular correlations in isotropic suspensions of tobacco mosaic virus. *Physical review letters*, 63(19):2068, 1989.

[36] D. Frenkel. Entropy-driven phase transitions. *Physica A: Statistical Mechanics and its Applications*, 263(1):26–38, 1999.

[37] K. Fricke, K. Wirthensohn, R. Laxhuber, and E. Sackmann. Flicker spectroscopy of erythrocytes. *European Biophysics Journal*, 14(2):67–81, 1986.

[38] A. P. Gast, C. K. Hall, and W. B. Russel. Phase separations induced in aqueous colloidal suspensions by dissolved polymer. *Faraday Discuss. Chem. Soc.*, 76:189–201, 1983.

[39] H. Giesekus. Die bewegung von teilchen in strömungen nicht-newtonscher flüssigkeiten. *Z. Angew. Math. Mech*, 58:T26–T37, 1978.

[40] H. P. Grace. Dispersion phenomena in high viscosity immiscible fluid systems and application of static mixers as dispersion devices in such systems. *Chemical Engineering Communications*, 14(3-6):225–277, 1982.

[41] C. Graf, H. Kramer, M. Deggelmann, M. Hagenbüchle, C. Johner, C. Martin, and R. Weber. Rheological properties of suspensions of interacting rodlike fd-virus particles. *The Journal of chemical physics*, 98:4920, 1993.

[42] E. Grelet and S. Fraden. What is the origin of chirality in the cholesteric phase of virus suspensions? *Physical review letters*, 90(19):198302, 2003.

[43] J. Groenewold and W. K. Kegel. Anomalously large equilibrium clusters of colloids. *The Journal of Physical Chemistry B*, 105(47):11702–11709, 2001.

[44] J. Groenewold and W. K. Kegel. Colloidal cluster phases, gelation and nuclear matter. *Journal of Physics: Condensed Matter*, 16(42):S4877, 2004.

[45] D. Guu, J. Dhont, and M. Lettinga. Dispersions and mixtures of particles with complex architectures in shear flow. *The European Physical Journal Special Topics*, 222(11):2739–2755, 2013.

[46] D. Guu, J. K. G. Dhont, G. A. Vliegenthart, and M. P. Lettinga. Depletion

induced clustering in mixtures of colloidal spheres and fd -virus. *Journal of Physics: Condensed Matter*, 24(46):464101, 2012.

[47] T. Hashimoto, K. Matsuzaka, E. Moses, and A. Onuki. String phase in phase-separating fluids under shear flow. *Physical review letters*, 74:126–129, 1995.

[48] W. Helfrich and R.-M. Servuss. Undulations, steric interaction and cohesion of fluid membranes. *Il Nuovo Cimento D*, 3(1):137–151, 1984.

[49] M. E. Helgeson, T. K. Hodgdon, E. W. Kaler, N. J. Wagner, M. Vethamuthu, and K. Ananthapadmanabhan. Formation and rheology of viscoelastic double networks in wormlike micelle nanoparticle mixtures. *Langmuir*, 26(11):8049–8060, 2010.

[50] P. Holmqvist, D. Kleshchanok, and P. R. Lang. Interaction potential and near wall dynamics of spherical colloids in suspensions of rod-like fd-virus. *The European Physical Journal E*, 26(1-2):177–182, 2008.

[51] P. Holmqvist, M. Lettinga, J. Buitenhuis, and J. K. Dhont. Crystallization kinetics of colloidal spheres under stationary shear flow. *Langmuir*, 21(24):10976–10982, 2005.

[52] S. M. Ilett, A. Orrock, W. C. K. Poon, and P. N. Pusey. Phase behavior of a model colloid-polymer mixture. *Phys. Rev. E*, 51:1344–1352, Feb 1995.

[53] E. Jamie, H. Wensink, and D. Aarts. Sedimentation–diffusion dynamics in colloid–polymer mixtures. *Journal of Statistical Mechanics: Theory and Experiment*, 2010(11):P11008, 2010.

[54] U.-S. Jeng, L. Esibov, L. Crow, and A. Steyerl. Viscosity effect on capillary waves at liquid interfaces. *Journal of Physics: Condensed Matter*, 10(23):4955, 1998.

[55] C. July and P. R. Lang. Depletion interactions effected by different variants of fd virus. *Langmuir*, 26(24):18647–18651, 2010.

[56] Y. Kaneda. Virosomes: evolution of the liposome as a targeted drug delivery system. *Advanced drug delivery reviews*, 43(2):197–205, 2000.

[57] K. Kang, M. Lettinga, Z. Dogic, and J. K. Dhont. Vorticity banding in rodlike virus suspensions. *Physical Review E*, 74(2):026307, 2006.

[58] V. Kantsler and V. Steinberg. Transition to tumbling and two regimes of tumbling motion of a vesicle in shear flow. *Physical review letters*, 96(3):036001, 2006.

[59] S. R. Keller and R. Skalak. Motion of a tank-treading ellipsoidal particle in a shear flow. *Journal of Fluid Mechanics*, 120:27–47, 1982.

[60] G. H. Koenderink, G. A. Vliegenthart, S. G. J. M. Kluijtmans, A. van Blaaderen, A. P. Philipse, and H. N. W. Lekkerkerker. Depletion-induced crystallization in colloidal rodâˆ’sphere mixtures. *Langmuir*, 15(14):4693–4696, 1999.

[61] P. R. Lang. Depletion interaction mediated by polydisperse rods. *The Journal of chemical physics*, 127:124906, 2007.

[62] P. R. Lang. Depletion interaction mediated by polydisperse rods. *The Journal of Chemical Physics*, 127(12):124906, 2007.

[63] H. Lekkerkerker, W.-K. Poon, P. Pusey, A. Stroobants, and P. Warren. Phase behaviour of colloid+ polymer mixtures. *EPL (Europhysics Letters)*, 20(6):559, 1992.

[64] H. N. W. Lekkerkerker and R. Tuinier. *Colloids and the Depletion Interaction*. Springer Berlin / Heidelberg, 2011.

[65] T. Lenstra, Z. Dogic, and J. Dhont. Shear-induced displacement of isotropic-nematic spinodals. *The Journal of Chemical Physics*, 114:10151, 2001.

[66] M. Lettinga, H. Wang, and J. Dhont. Microstructural response of a near-critical colloid-polymer mixture to shear flow. *Physical Review E*, 70(6):061405, 2004.

[67] K.-h. Lin, J. C. Crocker, A. C. Zeri, and A. Yodh. Colloidal interactions in suspensions of rods. *Physical review letters*, 87(8):088301, 2001.

[68] H. Loewen. Colloidal soft matter under external control. *Journal of Physics: Condensed Matter*, 13(24):R415, 2001.

[69] H. Löwen. Colloidal dispersions in external fields: recent developments. *Journal of Physics: Condensed Matter*, 20(40):404201, 2008.

[70] H. Löwen, A. Blaaderen, J. Dhont, P. Nielaba, and T. Palberg. Editorial. *The European Physical Journal Special Topics*, 222(11):2723–2725, 2013.

[71] G. Maitland. Oil and gas production. *Current opinion in colloid & interface science*, 5(5):301–311, 2000.

[72] L. Mandelstam. Über die rauhigkeit freier flüssigkeitsoberflächen. *Annalen der Physik*, 346(8):609–624, 1913.

[73] S. T. Milner and S. A. Safran. Dynamical fluctuations of droplet microemulsions and vesicles. *Phys. Rev. A*, 36:4371–4379, Nov 1987.

[74] F. Nettesheim, M. W. Liberatore, T. K. Hodgdon, N. J. Wagner, E. W. Kaler, and M. Vethamuthu. Influence of nanoparticle addition on the properties of wormlike micellar solutions. *Langmuir*, 24(15):7718–7726, 2008.

[75] H. Noguchi and G. Gompper. Swinging and tumbling of fluid vesicles in shear flow. *Physical review letters*, 98(12):128103, 2007.

[76] J. K. Oh, R. Drumright, D. J. Siegwart, and K. Matyjaszewski. The development of microgels/nanogels for drug delivery applications. *Progress in Polymer Science*, 33(4):448–477, 2008.

[77] P. D. Olmsted and C.-Y. D. Lu. Phase separation of rigid-rod suspensions in shear flow. *Physical Review E*, 60(4):4397, 1999.

[78] L. Onsager. The effects of shape on the interaction of colloidal particles. *Annals of the New York Academy of Sciences*, 51(4):627–659, 1949.

[79] A. Onuki. Phase transitions of fluids in shear flow. *Journal of Physics: Condensed Matter*, 9(29):6119, 1997.

[80] S. Oversteegen, J. Wijnhoven, C. Vonk, and H. Lekkerkerker. Crystallization kinetics and morphology in phase separating and sedimenting mixtures of colloidal spheres and rods. *The Journal of Physical Chemistry B*, 108(47):18158–18163, 2004.

[81] R. Pasquino, F. Snijkers, N. Grizzuti, and J. Vermant. Directed self-assembly of spheres into a two-dimensional colloidal crystal by viscoelastic stresses. *Langmuir*, 26(5):3016–3019, 2010.

[82] J. Pécréaux, H.-G. Döbereiner, J. Prost, J.-F. Joanny, and P. Bassereau. Refined contour analysis of giant unilamellar vesicles. *The European Physical Journal E*, 13(3):277–290, 2004.

[83] D. Pine, D. Weitz, P. Chaikin, and E. Herbolzheimer. Diffusing wave spectroscopy. *Physical Review Letters*, 60(12):1134, 1988.

[84] W. C. K. Poon. The physics of a model colloid polymer mixture. *Journal of Physics: Condensed Matter*, 14(33):R859, 2002.

[85] J. Prost. *The physics of liquid crystals*, volume 83. Oxford University Press, 1995.

[86] P. Pusey and W. Van Megen. Phase behaviour of concentrated suspensions of nearly hard colloidal spheres. *Nature*, 320(6060):340–342, 1986.

[87] J. Rallison. The deformation of small viscous drops and bubbles in shear flows. *Annual Review of Fluid Mechanics*, 16(1):45–66, 1984.

[88] H. Reiss, H. Frisch, and J. Lebowitz. Statistical mechanics of rigid spheres. *The Journal of Chemical Physics*, 31:369, 1959.

[89] S. A. Safran. Fluctuations of spherical microemulsions. *The Journal of Chemical Physics*, 78(4):2073–2076, 1983.

[90] J. Sambrook, E. F. Fritsch, and T. Maniatis. Molecular cloning: A laboratory manual. 1989.

[91] S. Samuel A. *Statistical Thermodynamics of Surfaces, Interfaces, and Membranes*. Perseus Books, 1994.

[92] C. A. Schneider, W. S. Rasband, and K. W. Eliceiri. Nih image to imagej: 25 years of image analysis. *Nat Meth*, 9(7):671–675, July 2012.

[93] R. Scirocco, J. Vermant, and J. Mewis. Effect of the viscoelasticity of the suspending fluid on structure formation in suspensions. *Journal of non-newtonian fluid mechanics*, 117(2):183–192, 2004.

[94] H. Sedgwick, S. U. Egelhaaf, and W. C. K. Poon. Clusters and gels in systems of sticky particles. *J. Phys.: Condens. Matter*, 16:S4913–S4922, 2004.

[95] D. H. Sharp. An overview of rayleigh-taylor instability. *Physica D: Nonlinear Phenomena*, 12(1):3–18, 1984.

[96] M. B. Smith, H. Li, T. Shen, X. Huang, E. Yusuf, and D. Vavylonis. Segmentation and tracking of cytoskeletal filaments using open active contours. *Cytoskeleton*, 67(11):693–705, 2010.

[97] J. Solon, J. Pécréaux, P. Girard, M.-C. Fauré, J. Prost, and P. Bassereau. Negative tension induced by lipid uptake. *Phys. Rev. Lett.*, 97:098103.

[98] W. Stöber, A. Fink, and E. Bohn. Controlled growth of monodisperse silica spheres in the micron size range. *Journal of colloid and interface science*, 26(1):62–69, 1968.

[99] A. Stradner, H. Sedgwick, F. Cardinaux, W. C. K. Poon, S. U. Egelhaaf, and P. Schurtenberger. *Nature*, 432:492–495, 2004.

[100] H. Strey, M. Peterson, and E. Sackmann. Measurement of erythrocyte membrane elasticity by flicker eigenmode decomposition. *Biophysical Journal*, 69(20):478 – 488, 1995.

[101] J. Tang and S. Fraden. Isotropic-cholesteric phase transition in colloidal dispersions of filamentous bacteriophage *fd*. *Liquid Crystals*, 19(4):459–467, 1995.

[102] G. Taylor. The formation of emulsions in definable fields of flow. *Proceedings of the Royal Society of London. Series A*, 146(858):501–523, 1934.

[103] G. Taylor. The instability of liquid surfaces when accelerated in a direction perpendicular to their planes. i. *Proceedings of the Royal Society of London. Series A. Mathematical and Physical Sciences*, 201(1065):192–196, 1950.

[104] K. C. Taylor and H. A. Nasr-El-Din. Water-soluble hydrophobically associating polymers for improved oil recovery: A literature review. *Journal of Petroleum Science and Engineering*, 19(3):265–280, 1998.

[105] P. R. ten Wolde and D. Frenkel. Enhancement of protein crystal nucleation by critical density fluctuations. *Science*, 277(5334):1975–1978, 1997.

[106] M. A. Tracy, J. L. Garcia, and R. Pecora. An investigation of the microstructure of a rod/sphere composite liquid. *Macromolecules*, 26(8):1862–1868, 1993.

[107] R. H. Tromp and E. H. De Hoog. Band formation on shearing in phase-separated polymer solutions. *Physical Review E*, 77(3):031503, 2008.

[108] C. L. Tucker III and P. Moldenaers. Microstructural evolution in polymer blends. *Annual Review of Fluid Mechanics*, 34(1):177–210, 2002.

[109] F. M. van der Kooij and H. N. Lekkerkerker. Formation of nematic liquid crystals in suspensions of hard colloidal platelets. *The Journal of Physical Chemistry B*, 102(40):7829–7832, 1998.

[110] A. Van Helden, J. W. Jansen, and A. Vrij. Preparation and characterization of spherical monodisperse silica dispersions in nonaqueous solvents. *Journal of Colloid and Interface Science*, 81(2):354–368, 1981.

[111] J. Vermant and M. Solomon. Flow-induced structure in colloidal suspensions. *Journal of Physics: Condensed Matter*, 17(4):R187, 2005.

[112] G. A. Vliegenthart and H. N. W. Lekkerkerker. Phase behavior of colloidal rod-sphere mixtures. *J. Chem. Phys.*, 111:4153–4157, 1999.

[113] A. Vrij. Possible mechanism for the spontaneous rupture of thin, free liquid films. *Discuss. Faraday Soc.*, 42:23–33, 1966.

[114] A. Vrij et al. Polymers at interfaces and the interactions in colloidal dispersions. *Pure Appl. Chem*, 48(4):471, 1976.

[115] B. Widom. Some topics in the theory of fluids. *The Journal of Chemical Physics*, 39(11):2808–2812, 1963.

[116] A. M. Wierenga, T. A. Lenstra, and A. P. Philipse. Aqueous dispersions of colloidal gibbsite platelets: synthesis, characterisation and intrinsic viscosity measurements. *Colloids and Surfaces A: Physicochemical and Engineering Aspects*, 134(3):359–371, 1998.

[117] P. R. t. Wolde and D. Frenkel. Enhancement of protein crystal nucleation by critical density fluctuations. *Science*, 277(5334):1975–1978, 1997.

[118] D. Won and C. Kim. Alignment and aggregation of spherical particles in viscoelastic fluid under shear flow. *Journal of non-newtonian fluid mechanics*, 117(2):141–146, 2004.

[119] Y. L. Wu, D. Derks, A. van Blaaderen, and A. Imhof. Melting and crystallization of colloidal hard-sphere suspensions under shear. *Proceedings of the National Academy of Sciences*, 106(26):10564–10569, 2009.

[120] K. Yaman, C. Jeppesen, and C. Marques. Depletion forces between two spheres in a rod solution. *EPL (Europhysics Letters)*, 42(2):221, 1998.

[121] K. Yaman, C. Jeppesen, and C. Marques. Depletion forces between two spheres in a rod solution. *EPL (Europhysics Letters)*, 42(2):221, 1998.

[122] K. Yaman, P. Pincus, and C. Marques. Membranes in rod solutions: a system with spontaneously broken symmetry. *Physical review letters*, 78(23):4514, 1997.

[123] N. Yasarawan and J. S. van Duijneveldt. Arrested phase separation of colloidal rod-sphere mixtures. *Soft Matter*, 6:353–362, 2010.

[124] T. H. Zhang, J. Klok, R. Hans Tromp, J. Groenewold, and W. K. Kegel. Non-equilibrium cluster states in colloids with competing interactions. *Soft Matter*, 8:667–672, 2012.

[125] K. Zimmermann, H. Hagedorn, C. C. Heuck, M. Hinrichsen, and H. Ludwig. The ionic properties of the filamentous bacteriophages pf1 and fd. *Journal of Biological Chemistry*, 261(4):1653–1655, 1986.